The Dissertation Committee for Byunghwa Park certifies that this is the approved version of the following dissertation:

MEMS BASED BEAD SIZE SELECTION METHOD FOR THE ELECTRONIC TASTE CHIP

Committee:

Dean P. Neikirk, Supervisor

Ananth Dodabalapur

Alvin B. Buckman

Jason B. Shear

Ray T. Chen

MEMS BASED BEAD SIZE SELECTION METHOD FOR THE ELECTRONIC TASTE CHIP

by

Byunghwa Park, B.S., M.S.

Dissertation

Presented to the Faculty of the Graduate School of

The University of Texas at Austin

in Partial Fulfillment

of the Requirements

for the Degree of

DOCTOR OF PHILOSOPHY

The University of Texas at Austin

December 2004

To my family

ACKNOWLEDGMENTS

I would like to thank my advisor, Professor Dean P. Neikirk, for his guidance over the years I spent as a member of Micro Electromagnetic Device Group. Especially, without his patients and supports during this research, it is impossible for me to finish this work. I am happy to work with Professor John T. McDevitt, Prof. Eric V. Anslyn, and Prof. Jason B. Shear about Electronic Tongue project. To my committee members, Prof. Ananth Dodabalapur, Prof. Ray T. Chen and Prof. A. Bruce Buckman, I also would like to express my appreciation for their time and interest on this work.

I would like to thank all the members of group for their friendship. I want to express my special thanks to my friends, Marvin F. Gilbreath, Nick Aristodulus, Chulchae Choi, Sangkyu Park, Minsoo Noh, Choongho Lee, Yoon Park, Jun wan Kim, Sangwook Han, Byungki Woo, Matthew Andringa and Jooyong Kim for his friendship and valuable discussion on this dissertation.

Finally, I am so grateful to my wife Youngjin Kim, parents, parents-in law and my brother for supporting my work in every part.

MEMS BASED BEAD SIZE SELECTION METHOD FOR THE ELECTRONIC TASTE CHIP

Publication No._____________

Byunghwa Park, Ph.D.

The University of Texas at Austin, 2004

Supervisor: Dean P. Neikirk

A micromachined biological and chemical sensor array has been developed for the rapid characterization of multiple analytes in solution. Various biochemical and chemical sensors are loaded in small micromachined structure together to analyze the ingredients in the fluid. Each sensors give unique optical signals under specific conditions that are acquired simultaneously by charge- coupled-device (CCD) optical detectors and those signal patterns are recognized as taste information. A novel micromachined structure has been added to the prototype structure for better performances in many parts. Surface micromachined structures confine sensor beads in the micromachined cavity as well as select designated sensor beads by way of size sorting method. This size selection method utilizes two separate size selective sieves on both sides of micromachined sensor cavities in the electronic taste chip. Each sensor is marked by certain size and selected by designated sensor cavity. Most preferred container of biochemical and chemical sensors is agarose beads. Agarose gel beads have the open pore structure which gives good attachment and binding to biological and chemical sensors. The structural characteristics of agarose bead are investigated and appropriate environment for agarose bead size selection method has been suggested. This research may be very useful in a micro total analysis system technology.

Table of Contents

List of Tables x

List of Figures xi

Chapter 1 Introduction..........1

Chapter 2 Review of the Electronic Taste Chip..........10

2.1 Motivation of the Electronic Taste Chip 10

2.2 Evolution of the Electronic Taste Chip..........11

2.3 Invention of the Electronic Taste Chip 13

Chapter 3 Bead Confining sensor chip 18

3.1 The need of new sensor covering structure..........18

3.2 Fabrication of springboard structure..........20

3.3 Summary..........29

Chapter 4 MEMS based size selection method 30

4.1 Motivation of size selection method..........30

4.2 Statistical approach of size selection method 32

4.3 Double side aligning process 35

4.4 Demonstration of bead size selection methods..........40

4.4.1 Glass bead size selection setup 40

4.4.2 Size selection experiment of dry glass beads..........43

4.4.3 Size selection experiment in wet condition 52

4.5 Size selection of the agarose beads with fluorescent marker 56

4.6 Summary..........59

Chapter 5 Results and Discussions..60

5.1 Agarose beads as the chemical and biological sensor container.............60

5.2 Nature of polymer bead swelling and dry shrinkage 62

5.3 Study of agarose bead size changes..64

5.4 The effect of environmental humidity changes to sensor activities........85

5.5 summary...97

Chapter 6 Conclusion 98

Bibliography 101

Vita 104

List of Tables

Table 1.1: Comparison of important properties of silicon crystal and carbon steel 2

Table 3.1: Tripe layer composition and Yield, with Silicon nitride film...........27

Table 3.2: Triple layer composition and Yield, with Silicon rich nitride film...28

Table 3.3: Yield of silicon rich nitride structure...28

Table 4.1: Mis-fill possibilities Vs. separation factor..34

Table 4.2: Glass bead size and distribution...42

List of Figures

Figure 1.1: Illustration of anisotropic wet etching of (1 0 0) silicon................4

Figure 1.2: Example of high aspect ratio of SU-8..5

Figure 1.3: Curing of PDMS..6

Figure 1.4: PDMS casting examples of micro fluidic channel..........................7

Figure 1.5: Basic surface micromachining process...5

Figure 2.1: Example of DNA-On-Chip by Genometrix.................................12

Figure 2.2: A bead in the well of electronic tongue.......................................13

Figure 2.3: Illustrations of the basic electronic tongue base platform fabrication 14

Figure 2.4: Color pattern of beads depend on indicator containin and environmental pH strength..15

Figure 2.5: CCD detecting system..16

Figure 2.5: Illustration of sensor manufacturing and sensing procedure 17

Figure 3.1: The Electronic tongue chip with fluid guide................................18

Figure 3.2: Bead captured in microfilm cover..19

Figure 3.3: Etching simulation of concave opening mask 20

Figure 3.4: Dielectric stress as a function of thickness for LPCVD 21

Figure 3.5: Stress relieving sandwich film stack..22

Figure 3.6: Residual stress and Young's Modulus calculated by equation (3.1)23

Figure 3.7: Relieving sandwich structure with low stress nitride film............25

Figure 3.8: Etch rate chart ($CF_4 + O_2$ @ 200W)...25

Figure 3.9: Illustration of RIE overetching 26

Figure 4.1.1: Illustrations of the size selection unit...31

Figure 4.1.2: Single side bead size selection chip design.................................31

Figure 4.2.1: Overlap between different size-selective finger designs.............22

Figure 4.2.2: 1σ Separation case 33

Figure 4.3.1: Illustrations of double side size selection unit.............................35

Figure 4.3.2: Example of under-etch cavity 36

Figure 4.3.3: Illustration of double side etch result...37

Figure 4.3.4: Double side process photomask..38

Figure 4.3.5: Picture of size selection unit, the top and the bottom units 39

Figure 4.4.2.1: Illustration of vacuum bead installation 44

Figure 4.4.2.2: Before bead installation...45

Figure 4.4.2.3: Needle with beads approaches on top of the size selection units.45

Figure 4.4.2.4: Beads bombard onto the chip(see left top unit)...........................46

Figure 4.4.2.5: 100 micron bead settled its designated place 46

Figure 4.4.2.6: Bead installation successful...47

Figure 4.4.2.7: 140 micron beads bombardment 48

Figure 4.4.2.8: Bead trace approaches to 140micron spot..................................48

Figure 4.4.2.9: 140 micron bead installed successfully......................................49

Figure 4.4.2.10: 200 micron bead installing 49

Figure 4.4.2.11: 200 micron bead installed successfully......................................50

Figure 4.4.2.12: Getting rid of beads on top of the chip by side-air blowing........50

Figure 4.4.2.13: Bottom right beads are blown away...51

Figure 4.4.3.1 : Illustration of wet bead installation...52

Figure 4.4.3.2 : Dropping of 160 micron agarose polymer beads 53

Figure 4.4.3.3 : Water is passing through sorting units 54

Figure 4.4.3.4 : 160 micron sorting unit captured bead.......................................54

Figure 4.4.3.5 : Water in the surface is absorbed...55

Figure 4.5.1 : Bead size selection plan 56

Figure 4.5.2 : After putting 250µm, 280µm and 300µm beads under combo, red and green illumination 57

Figure 4.5.3 : After putting 250µm, 280µm, 300µm and 355µm beads under combo, red and green illuminations...58

Figure 5.1.1 : Crosslinking polymer - GEL 60

Figure 5.1.2 : Agarose bead 61

Figure 5.2 : Illustration of agarose bead swelling 62

Figure 5.3.1 : Agarose bead size shrink chart 64

Figure 5.3.2 : Initial stage of beads in normal atmosphere...............................66

Figure 5.3.3 : Right before starting shrink, after 220 seconds in normal atmosphere 66

Figure 5.3.4 : Bead start shrinking, after 240 seconds in normal atmosphere….67

Figure 5.3.5 : Bead is shrinking, after 300 seconds in normal atmosphere ……67

Figure 5.3.6 : Agarose beads size shrinkage chart under dry air flowing environment 68

Figure 5.3.7 : Agarose bead size change as getting wet and dry 69

Figure 5.3.8 : Agarose bead expands as water drops onto, 30 seconds intervals...71

Figure 5.3.9 : Agarose bead expands as water drops onto, 30 seconds intervals...72

Figure 5.3.10 : Bead swelling by water and 100% humidified air 73

Figure 5.3.11 : Agarose beads size change chart, under air flow by humidifier..74

Figure 5.3.12 : Agarose bead swelling and drying experiment, on vacuum chuck with humidifier 75

Figure 5.3.13 : Agarose bead on the chip with vacuum chuck turned, in humidified air, t=0 second..76

Figure 5.3.14 : Agarose bead on the chip with vacuum chuck turned, in humidified air, t=120 seconds 77

Figure 5.3.15 : Agarose bead on the chip with vacuum chuck turned, in humidified air, t=240 seconds 77

Figure 5.3.16 : Agarose bead on the chip with vacuum chuck turned, in humidified air, t=480 seconds 78

Figure 5.3.17 : Agarose bead on the chip with vacuum chuck turned, t=510 seconds 78

Figure 5.3.18 : Agarose bead on the chip with vacuum chuck turned, t=630 seconds 79

Figure 5.3.19 : Agarose bead on the chip with vacuum chuck turned, t=690 seconds 79

Figure 5.3.20 : Agarose bead on the chip with vacuum chuck turned, t=750 seconds 80

Figure 5.3.21 : Size of the agarose bead on vacuum chuck under humidified environment 81

Figure 5.3.22 : Size of the agarose bead under humidified environment 82

Figure 5.3.23 : Agarose bead in humidified environment, t=0 second.............83

Figure 5.3.24 : Agarose bead in humidified environment, t=200 seconds 83

Figure 5.3.25 : Agarose bead in humidified environment, t=400 seconds 84

Figure 5.3.26 : Agarose bead in humidified environment, t=600 seconds 84

Figure 5.4.1 : Illustrations of chemical sensing reaction measurement step 86

Figure 5.4.2 : Immunoassay steps and variations for experiments 88

Figure 5.4.3 : Normal condition assay result – the control...............................89

Figure 5.4.4 : Assay result of dried sample 91

Figure 5.4.5 : Assay result of dried – reconstructed by saturated humid air sample 92

Figure 5.4.6 : Assay result of chip stored under saturated humid air environment 93

Figure 5.4.7 : Non specific antibody assay result under saturated humid air environment 95

Figure 5.4.8 : non-specific antigen assay under saturated humid air environment … 96

Chapter 1 Introduction

The sense of taste is a result of complex chemical analyses which are completed in parallel fashion at a series of chemically active taste buds on the tongue. These taste buds are located within depressions in the tongue where the molecular and ionic reagents become restricted to allow time for their identification. We have four primary tastes: sweet, sour, salty and bitter. We combine the magnitude of those tastes to create a pattern that is distinctive for each food. The electronic tongue is a chemical array sensor, which is analogous to the mechanism of taste sensing. The electronic tongue technology is comprised of four primary parts: the sensing part, the micromachined platform, the CCD (Charge coupled device) pattern detection and pattern recognition and signal processing. The electronic tongue has arrays of different sensors, each located within depressions in the silicon micromachined sensor platform. The CCD pattern detecting system collects the color information from each sensing bead, and pattern recognition combines the information to decide the particular analytes in the test fluid [1].

Astonishing progress made in microsensors and microactuators in recent years are mainly due to advances in micromachining technology. Micromachining technology enables the fabrication of mechanical structures with very tiny dimensions in micrometer or even in nanometer range. This micromachining technology can be classified into three main branches. Bulk micromachining is based upon the etching of a single crystal silicon wafer with the help of the etch mask layer made of silicon oxide or silicon nitride film. Surface micromachining technology, another main branch, is building a 3-D structure by depositing or growing thin layers on a substrate surface. LIGA (LIthographie, Galvanoformung, Abformung) process technology is building high aspect ratio structures utilizing X-ray lithography with thick resist layers and electroplated metal layers. Those three technologies lead the MEMS (Micro Electro Mechanical System) marketplace and form the technology mainstream.

Most of MEMS devices are made of/with single silicon crystal. In the background of this preference to silicon as a MEMS material, there are several benefits ranging from the intrinsic level to the application level. The basic benefit of silicon is that it is a mechanical material with high strength. Table 1.1 lists important properties comparing silicon and steel. This table shows why silicon can be a good mechanical material.

Property	Silicon Crystal	Carbon Steel
Crystal Structure	Diamond	BCT
Melting point	1415˚C	1537 °C
Thermal expansion	2.5×10^{-6} / °C	$12.6\sim14.2 \times 10^{-6}$ / °C
Density	2.3 g/cm^3	7.872 g/cm^3
Young's Modulus	200 GPa	200 GPa
Yield strength	6.9 GPa	2.1 GPa
Mohs hardness	6.5	4

Table 1.1 Comparison of important properties of silicon crystal and carbon steel. (some variations depends on the amount of carbon in steel)[2][3].

One can notice that the yield strength of silicon crystal is 3.5 times larger than that of steel, and it has similar Young's Modulus even though its density is only one third of steel. From this information, one can notice that the silicon crystal is elastic and does not have a mechanical hysteresis change. Furthermore, silicon crystal has a smaller thermal expansion coefficient than steel. From those facts, the silicon crystal can be a distinguished mechanical material comparable to steel. In addition to these mechanical properties, silicon technology has many side benefits from its down-size-ability. In the advancement of ULSI (Ultra Large Scale Integration) technology, lithography and etching technology have been critical in achieving downsizing benefits. The integrate circuit (IC) downsizing brought about the reduction of power consumption, mass production, cost reduction, and so forth. With the help of this state-of-the-art photolithography and etching technology, micromachined devices can be fabricated in standard integrated circuit (IC) fabrication laboratories with the addition of only a few facilities. Micromachining has the benefit of its small size. Especially, sensors made with micro fabrication technology are useful because sensors do not need to be big in general. Furthermore, both structure and IC can be fabricated side by side on a single wafer. This can bring about better signal to noise ratio because short interconnection between the sensor and IC results in the reduction of noise. Also, reduced power consumption can be achieved, and this results in better portability and less thermal error. This is the benefit of IC as well as the benefit of MEMS devices, which are made of silicon.

Bulk micromachining technology is generally known as building a structure made of silicon crystal or composite materials, deposited or grown on the silicon substrate, with anisotropic wet etch technique. Wet anisotropic etching is the process of preferential directional etching of material using liquid etchants [4]. Anisotropic silicon etching can be defined as crystal orientation-dependent etching. This phenomenon was first reported in late 1960s and has been used since the early 1980s. There are several anisotropic silicon etchants, and they are KOH, hydrazine-water solution, EDP, TMAH, and CsOH. Among those etchants, KOH is the most widely used because of its superior anisotropic etching ratio to crystal orientation. Other etchants are also used to accommodate special requirements such as contamination problems.

This anisotropy depends strongly on crystallographic orientation. In detail, (111) surfaces show slowest dissolution rate compared with (1 0 0) and (1 1 0) planes. It is generally known that the typical etch ratio of those three planes in KOH solution is 1 (111) : 300~400 (1 0 0) : 600 (1 1 0) [4]. This high ratio makes it possible to develop unique structural topology shown below in figure 1.1, and it can be the foundation of various micromachined structures. While this anisotropy is widely accepted and applied to building microstructures, the mechanism of anisotropic etching along crystal planes has not been fully explained. It is generally understood that anisotropic etching is a function of area density of atoms, energy needed to remove an atom from the surface, and geometric screening effects[4].

For the anisotropic etching process shown in Figure 1.1, we need etch masks on the top of and at the bottom of silicon. Generally, silicon oxide or silicon nitride is used as an etch mask, while a mixture of silicon oxide and silicon nitride can be used to prevent stress issues. Silicon oxide cannot be a perfect material for the mask of anisotropic etchant because it can also be dissolved by KOH solution. Hence, silicon nitride is deposited instead of silicon oxide or is deposited on the top of the silicon oxide layer. It is very unusual, but after the etching process, sometimes the whole wafer is completely dissolved due to overetching. In bulk micromachining, time is the most important factor for controlling the amount of etching, but etch rate does not always remain the same even if other conditions such as etching temperature and etchant concentration are nominally constant.

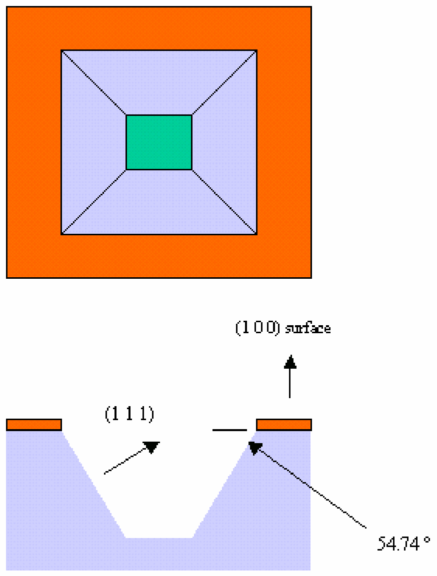

Figure 1.1 Illustration of anisotropic wet etching of (1 0 0) silicon.

One of the emerging new technologies in MEMS fabrication is PDMS casting. Compared with the LIGA process, this process is extremely cheap and makes it easier to create 3-dimensional structures. The key point of this technology is the photoresist called “SU-8”. The SU-8 resist is a negative, epoxy-type, near-UV photoresist based on EPON SU-8 epoxy resin that has been originally developed and patented by IBM. This photoresist can be as thick as 2 mm and aspect ratios >20 have been demonstrated with standard contact lithography equipment. These astounding results are due to the low optical absorption in the UV range which only limits the thickness to 2 mm for the 365nm-wavelength where the photo-resist is the most sensitive (i.e., for this thickness 100% absorption occurs). Of course LIGA still yields better results but low-cost application will undoubtedly benefit from this resist that is well suited for acting as a mold for electroplating because of its relatively high thermal stability (Tg > 200°C for the cross-linked (i.e., exposed) resist; Tg is the glass transition temperature) [6].

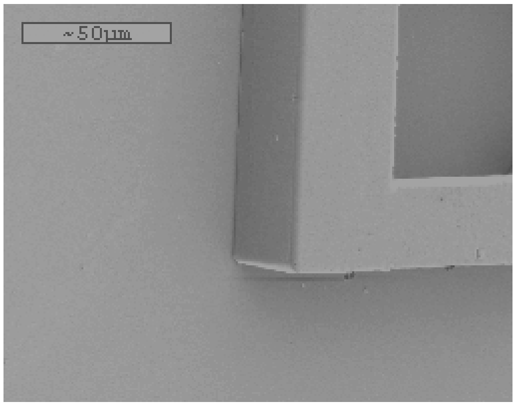

Figure 1.2 Example of high aspect ratio SU-8 pattern[6].

The other key of this technology is the elastomer polydimethylsiloxane (PDMS). It comes with a base and a curing agent. The cured elastomer is transparent and colorless and has been praised by MEMS engineers as "ideally suited for electrical/electronic potting and encapsulating applications”. PDMS is cured by an organometallic crosslinking reaction. The siloxane base oligomers contain vinyl groups. The crosslinking oligomers contain at least 3 silicon hydride bonds each. The curing agent contains a proprietary platinum-based catalyst that catalyzes the addition of the SiH bond across the vinyl groups, forming Si-CH_2-CH_2-Si linkages. The multiple reaction sites on both the base and crosslinking oligomers allow for three-dimensional crosslinking. One advantage of this type of addition reaction is that no waste products such as water are generated. If the ratio of curing agent to base is increased, a harder, more cross-linked elastomer results. Heating will also accelerate the crosslinking reaction[7,8].

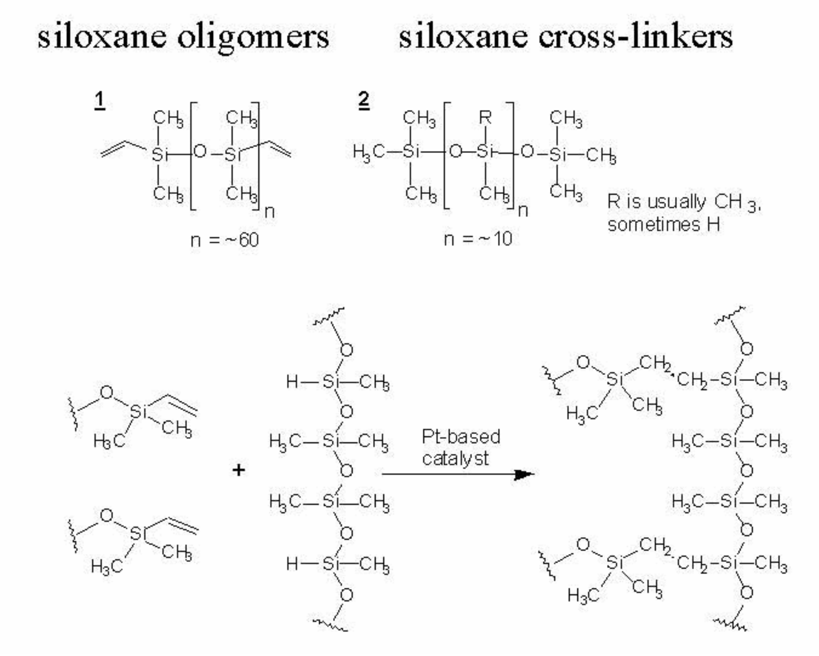

Figure 1.3 Curing of PDMS[7,8].

The PDMS process is almost same as the LIGA process. The only drawback of PDMS is its hydrophobic characteristic. A lot of microfluidic devices are created by this technology, but hydrophobic surfaces limits its versatility. Many attempts to turn the surface to a hydrophilic one have been researched by many MEMS engineers[9].

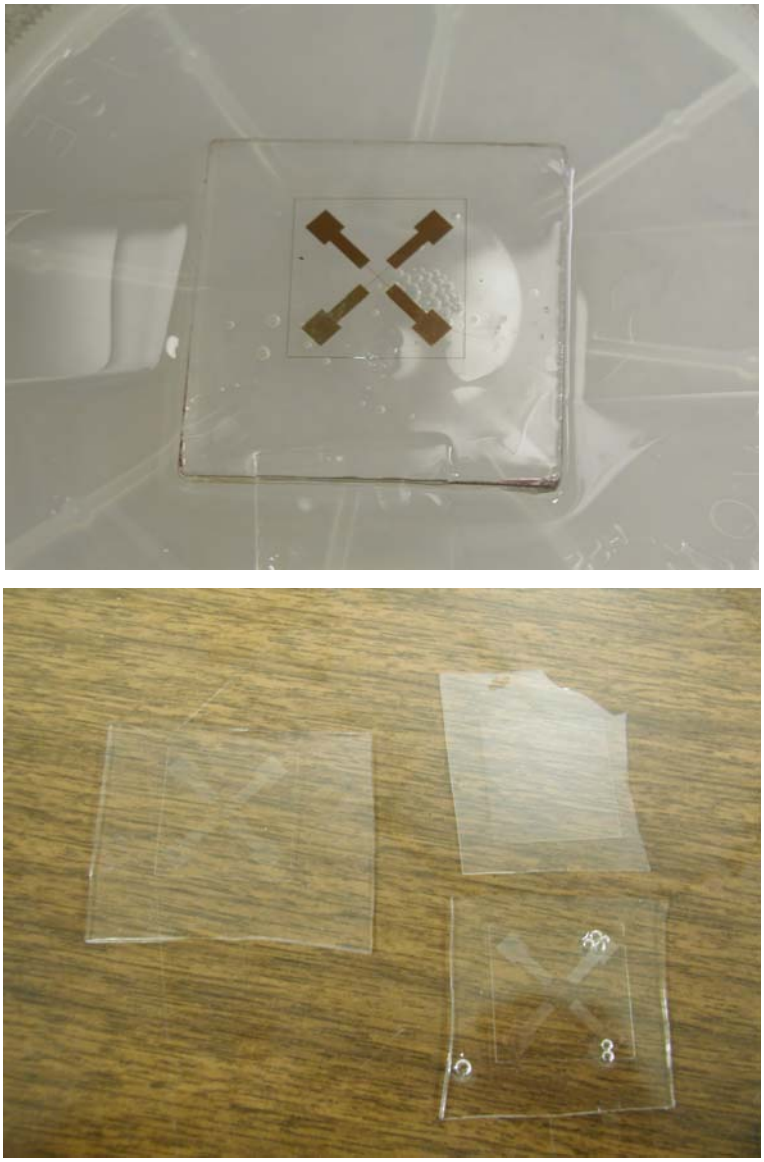

Figure 1.4 PDMS casting examples of micro fluidic channel.

Surface micromachining is the fabrication of a 3-D microstructure from multiple layer film stacks, deposited or grown on the silicon or other substrate, with the help of sacrificial layers and isotropic/anisotropic etching. This technology has been used from late 80's with the fabrication of fascinating gears and digital micromirror devices. The mainstream of surface micromachining technology is polysilicon surface micromachining. Analog Devices introduced a low price accelerometer using this polysilicon surface micromachining technology, and Texas Instruments made a digital micro mirror, which enables higher resolution projector with higher performance and low price[10,11]. In the meantime, UC Berkeley has announced a new MEMS material, polycrystalline SiGe, which has potential for having low intrinsic stress when deposited. Also it can be annealed at comparatively lower temperature for reducing stress. The basic procedure of surface micromachining fabrication is illustrated in Figure 1.6[12].

In early surface micromachining, polysilicon played the best role as the structural material, while SiO_2 and phosphosilicate glass (PSG) were main sacrificial materials. The structural layer must have desirable mechanical and electrical properties, while the sacrificial layer must be stable during mechanical film deposition and vice versa. In addition to polysilicon, aluminum, silicon nitride, silicon carbide, polycrystalline SiGe, GaAs, CVD diamond and GaN have been tested as structural layers. These various materials satisfy various requirements as a structural material. As for the sacrificial layer, polysilicon, photoresist, polyimides, aluminum gallium arsenide, carbon, Parylene, copper, aluminum, and other metals are used. Of course, those materials should be able to be used in a clean room.

Figure 1.6 is an illustration of a basic polysilicon surface micromachining process. On the base substrate, usually a silicon wafer, a poly ground plane is deposited. The sacrificial layer is deposited, and the height of the structure is determined by the thickness of the sacrificial layer. The sacrificial layer is patterned and etched to be filled with the structural polysilicon layer. Because the top surface is not flat due to the etched anchors and dimples on the sacrificial layer, a chemical mechanical surface polishing process can follow the structural layer deposition.

The last thing to do is to remove the sacrificial layer to have a 3-D structure. This is a basic one level process. Currently, Sandia National Laboratory has demonstrated a five level polysilicon process. Surface micromachining shows the art of building 3-D structures from 2-D etching technology.

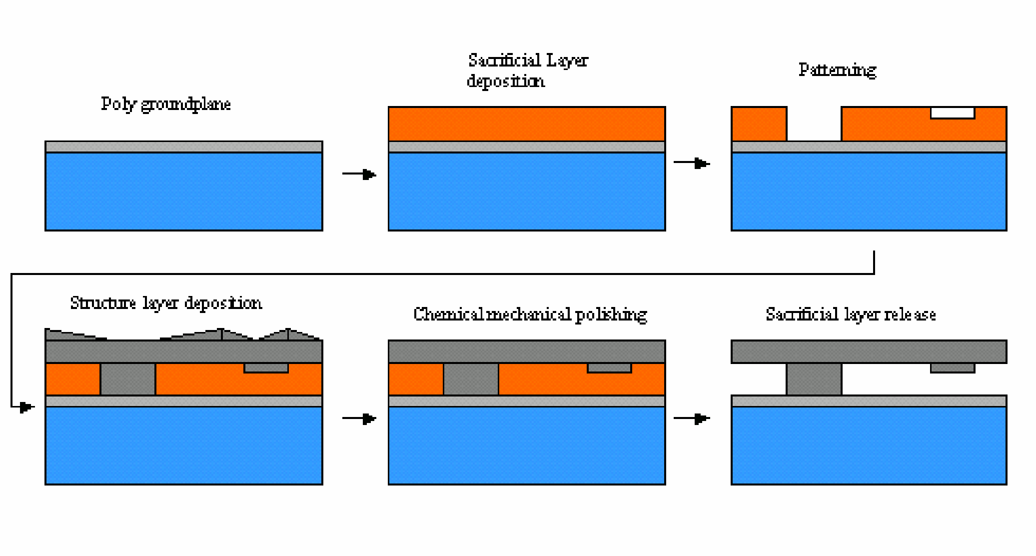

Figure 1.5 Basic surface micromachining process.

This dissertation is focused on the coordination of the preparation of chemically sensitive sensor beads and the fabrication of a micromachined platform by MEMS technology introduced above. Since the first micromachined structure was invented, its original topology and fabrication technology have been revised over and over to reduce process steps and introduce new functions. For example, a simple pit array sensor was combined with a novel capillary pump, which absorbs and delivers fluid immediately into the pits[13].

This dissertation examines a new type of sensor chip, which enhances the procedure for installing sensor beads with a size selection method. The actual size selection chip is fabricated and tested with various kinds of beads. A bead size selection method is demonstrated, problems accompanying this method are verified, and the solution to these limitations is suggested. As agarose beads are main sensor container in electronic taste chip, size selection methods for agarose beads are also tested.

Chapter 2 Review of the Electronic Taste Chip

This chapter introduces electronic tongue technology. Each part of the electronic tongue will be briefly introduced here to help understanding of the importance of the sensor platform[1].

2.1 Motivation of the Electronic Taste Chip

The discrimination of toxins, various analytes and bacteria has become increasingly important for environmental, health and safety, remote sensing, military and chemical processing applications. Due to the various usages of toxins, analytes and bacteria for the benefits of our life, inappropriate chemical wastes endanger not only human beings but also the whole ecosystem we are living in. To protect our life from the danger we had brought about, appropriate and correct discrimination and cleaning up are keenly required.

This demand has driven the advent of versatile sensors, which fulfill the various discrimination requirements for multiple biological agents, toxins, and chemical warfare agents. Furthermore, early decontamination, early and cheap detection of disease, and quality control of food and beverage will be possible with the smart sensors. So far, new chemical sensing systems using DNA and antibody-based sensing fashioned for single analyte detection have been developed and commercialized by many research institutions and pharmacy companies. [1]

The interdisciplinary team from the University of Texas suggested the combination of multiple kinds of sensors, including various kinds of DNA sensors, biochemical sensors and chemical sensors, formed into ordered arrays, capable of simultaneously detecting many analytes in real-time in a micromachined array sensor structure. Each team in the interdisciplinary team plays one or more of the roles listed below:

1) molecular recognition and solid-state synthesis of oligomeric compounds.
2) molecule-based devices and optical measurements.
3) photophysical studies and signal processing.
4) micromachining sensor platform.
5) pattern recognition and training.

2.2 Evolution of the Electronic Taste Chip

The electronic tongue is an expanded concept of an electronic nose, which is a primitive form of combinatorial library sensor. Recently, those electronic noses have been developed commercially, but they are limited in their use because they can be used to identify only volatile agents [5]. The electronic tongue follows the main pattern algorithm of the electronic nose. The electronic nose has a reference library for identifying smell. In addition to identifying smell, it has the ability to expand its library by learning from the array to respond to new stimuli. Peculiar patterns made by new or unknown analytes are recorded into a database to deal with similar species in future time. As the concept of the electronic nose has been widely accepted to this field, the need of identifying the analytes present in liquids and other non-volatile fluids induced the advent of the electronic tongue.

In the meantime, microbiologists suggested “DNA on a chip”, which targets the identification of DNA fragments. This device possesses a high density of DNA hybridization sites that are affixed in a two-dimensional pattern on a planar substrate. Pattern generation and the library reference identification mechanism of these devices share the same idea with electronic nose with a different signal acquisition system. This DNA-on-chip enabled multiple gene assaying at a time. Commercialized DNA chips can achieve high throughput by saving costs and time. [14]

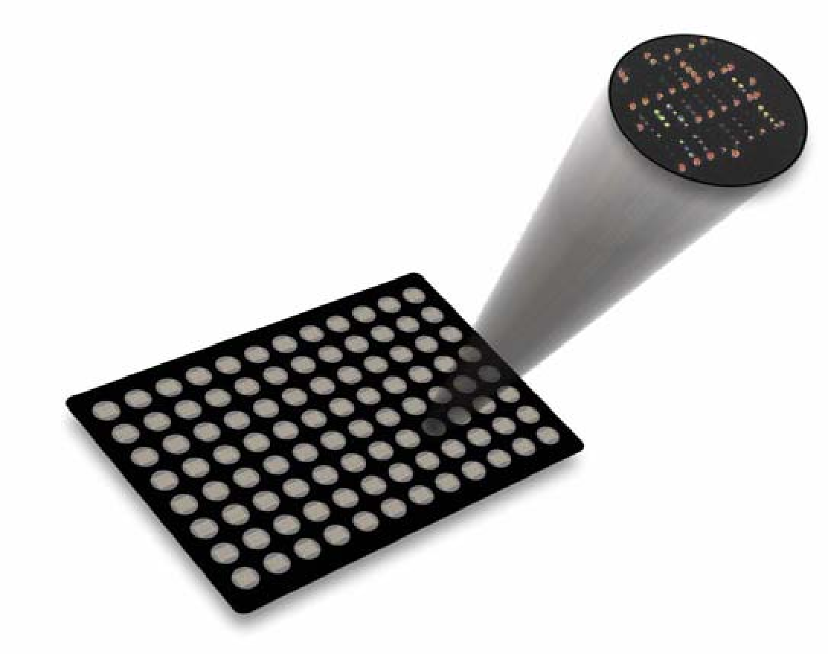

Figure 2.1 Example of DNA-On-Chip by Genometrix [14].

At the same time, there was a need for array sensors which target the analytes which are not volatile, do not contain DNA, and want to assay multiple analytes at a time. This market grew larger and larger after successful demonstration of the electronic nose, and many research institutes related to analyte assay rushed into array sensor business. The researchers in the University of Texas made good approach amongst theses stream. Dr. Eric Anslyn's group achieved significant results in the specific recognition of a cell surface saccharide using combinatorial chemistry. In addition to recognition of these sugar complexations, Anslyn's group have begun to develop a variety of alternative solid state oligomer preparation methods using building blocks made of peptides, and several unnatural oligomers[1,15].

2.3 Invention of the Electronic Taste Chip

Based on the chemistry and biology scientists' individual achievements in analyte detection libraries, UT team proposed a sensor form which mimics the topology of the mammalian tongue with the help of MEMS technology.

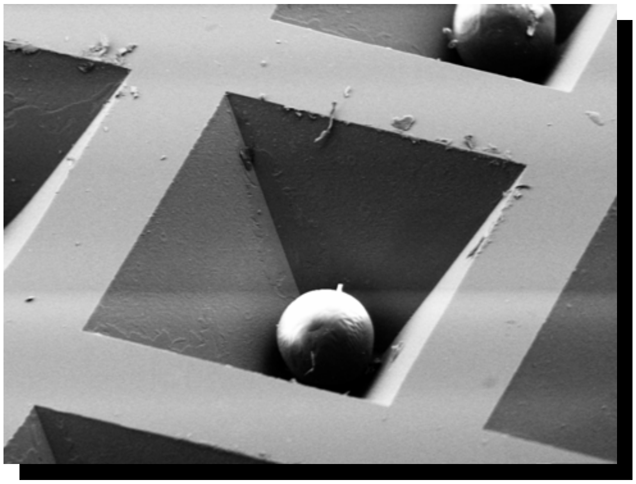

Figure 2.2 A bead in the well of electronic tongue.

The basic electronic tongue chip was made with bulk micromachining technology. Base material is a double side polished P type silicon wafer with the thickness of 250 micrometers. Before placing the silicon wafer in an LPCVD chamber for deposition, "piranha" etch cleaning is required. The piranha etch cleans up organic contaminants on the wafer surface. This piranha solution is 1:1 mixture of concentrated H_2SO_4 and H_2O_2 at 150°C. Silicon nitride is deposited on both sides of the silicon wafer. The CVD chamber at the Microelectronics Research Center of the University of Texas at Austin has the deposition rate of silicon nitride film of about 500 Å/ 10 min. Usually the thickness of the silicon nitride layer for the basic electronic tongue sensor chip is 1000 Å, which is thick enough to endure KOH wet etching process. However, thickness control is an important factor for this fabrication because KOH solution etches not only the silicon substrate but also the silicon nitride layer. If the thickness of the silicon nitride layer is too thick, the tensile stress of silicon nitride layer spoils the topology of pattern, and the wafer is prone to breakage. After depositing the silicon nitride layer, the wafer is moved to the photolithography room. After pattern exposing and developing, etching of the silicon nitride mask layer follows. This nitride layer is etched by reactive ion etch (RIE), which uses oxygen gas and CF_4 gas. After the RIE, this wafer is dipped into 79 °C KOH solution for 9 hours for silicon substrate etching. After finishing the wet etching, the wafer is sent to a dicing company to be diced into small chips. The final chip size is less than 1cm x 1cm.

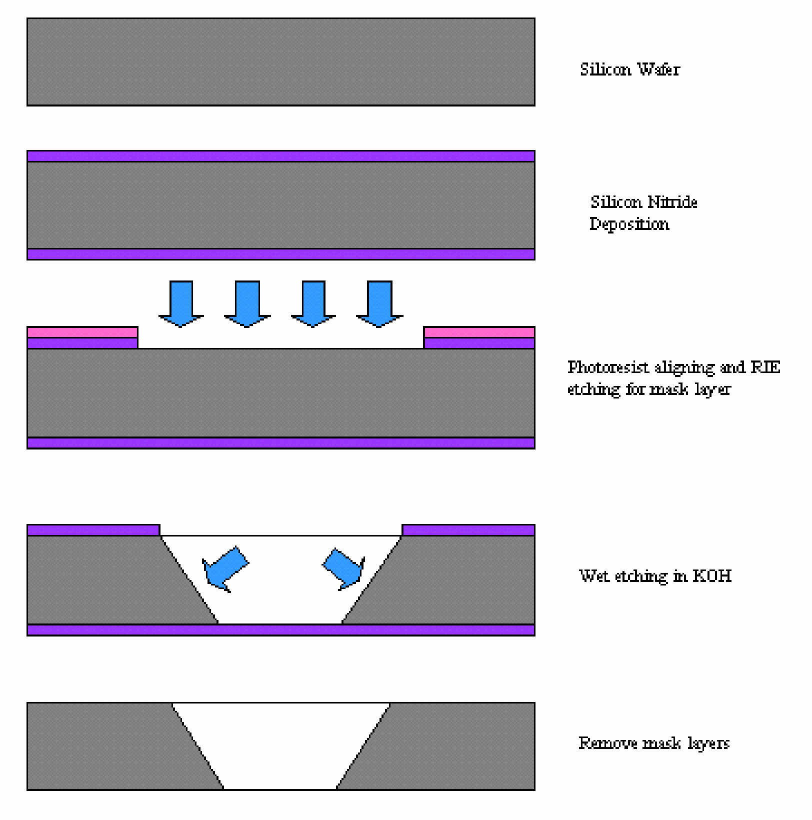

Figure 2.3 Illustrations of the basic electronic tongue base platform fabrication.

In the case of the electronic nose, it is a combination of chemical sensor technology and VLSI MOSFET technology. The electronic nose gives the identification information in the form of electrical resistance differences, while the electronic tongue does it through optical image information[5]. In a mammalian tongue, as sensor buds receive target tastants, they send signals to the nerve system. In the electronic tongue, the beads contain chemical/biological indicators that react with their target analytes and change their color sometimes depending on not only target analytes but also environmental pH. The pH strength is another important factor for deciding tastes in complex chemical mixtures.

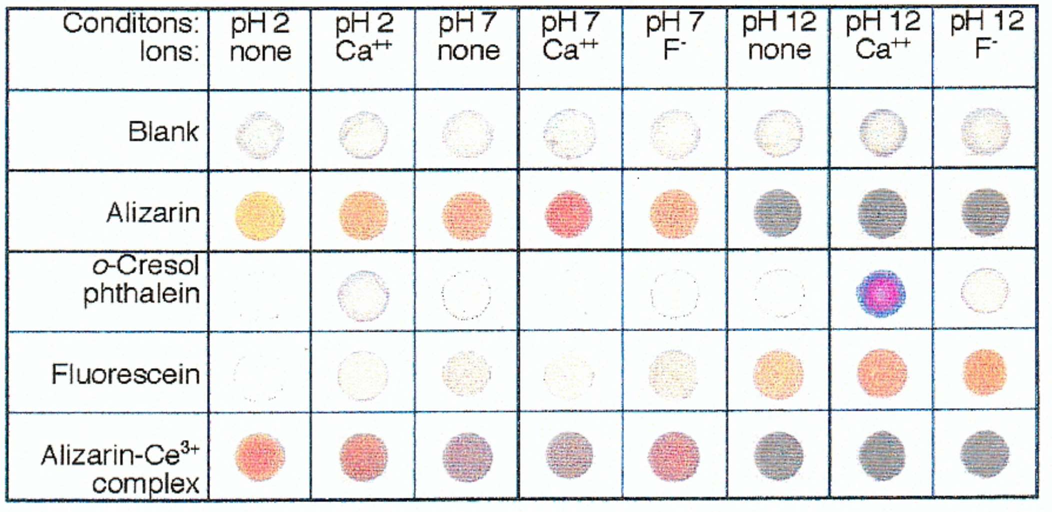

Conditons: Ions:	pH 2 none	pH 2 Ca^{++}	pH 7 none	pH 7 Ca^{++}	pH 7 F^-	pH 12 none	pH 12 Ca^{++}	pH 12 F^-
Blank								
Alizarin								
o-Cresol phthalein								
Fluorescein								
Alizarin-Ce^{3+} complex								

Figure 2.4 Color pattern of beads depend on indicator containing and environmental PH strength [15].

These optical color patterns are unique for each analyte, and these patterns are stored in a computer as the computer comes across new color patterns. As our nerve system delivers sense signals from our sense organs to the brain, this color pattern is delivered to the computer via a CCD camera for identifying analytes in liquid. In figure 2.5, we see the overview of the CCD signal transfer system from sensor to computer. A blue light emitting diode is used for systems relying on changes in fluorescence signals.

For colorimetric (i.e. absorbance) based systems, a white light would be used in place of the high energy excitation source. For fluorescence measurements, a filtering agent will be exploited to remove the excitation wavelength. A charge-coupled device (CCD) positioned below the micromachined stage will allow for data acquisition. The light emitted by the LED is modulated by the beads in the micromachined stage and passes through the bottom opening and into a CCD detector. This pattern detected by the CCD is now analyzed by the computer to identify the analytes. The computer has a large database to refer to, as well as an ability to expand its database by learning new patterns. [15]

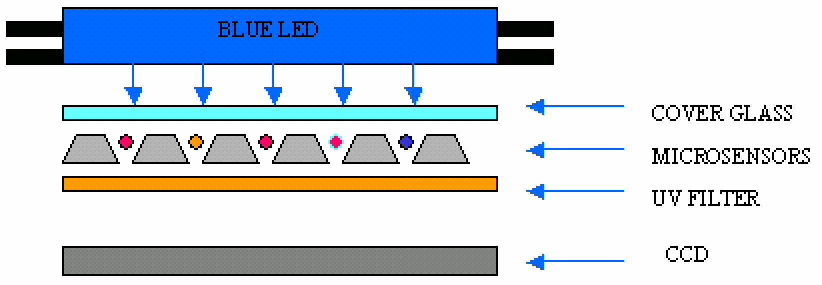

Figure 2.5 CCD detection system.

In this chapter, each component of the electronic tongue is introduced. For easy understanding of the total taste sensing process, figure 2.6 illustrates the assembly of the electronic taste chip.

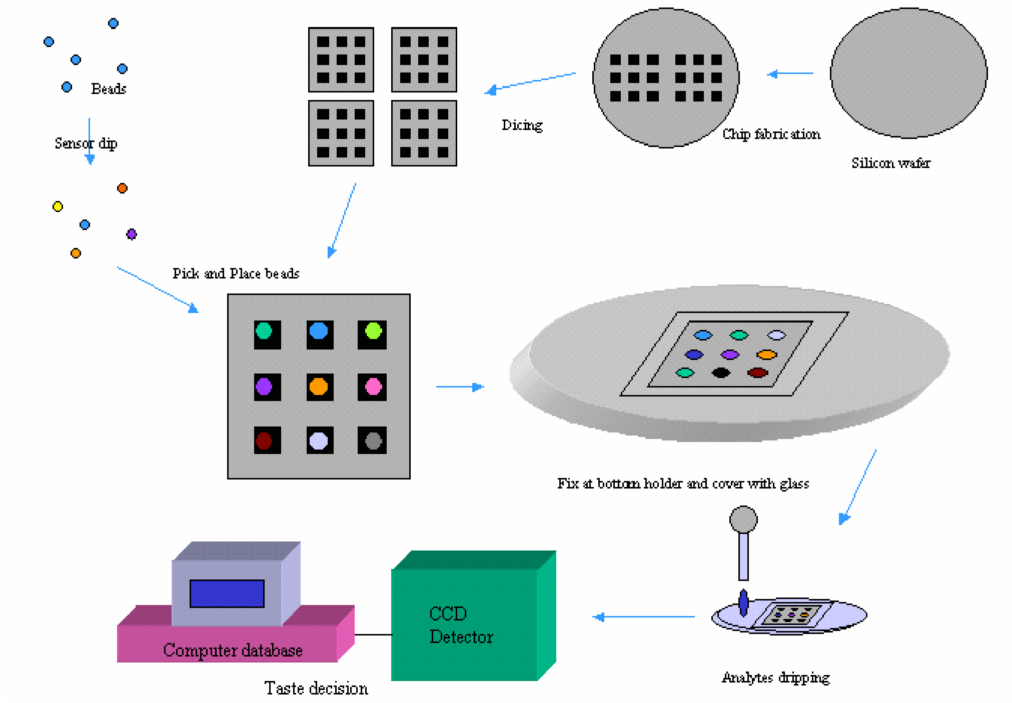

Figure 2.6 Illustration of sensor manufacturing and sensing procedure.

Chapter 3   Bead confining sensor chip

Basic steps for the fabrication of the electronic tongue have been reviewed in the previous chapter. In this chapter, an innovative attempt for acquiring better fluid-movement and labor-saving structure will be discussed.

3.1. The need of new sensor covering structure

According to the previous chapter, a silicon nitride film, deposited by CVD, is used as a mask layer for the bulk micromachining of the silicon substrate. This basic tongue chip is robust and easy to fabricate; however, it has some drawbacks. When a specimen is introduced, the fluid should permeate into each sensor from the thin gap between cover glass and substrate. However, this mechanism does not ensure the uniform supply of fluids to each sensor. Additionally, the bonding chemical, which bonds cover glass to silicon

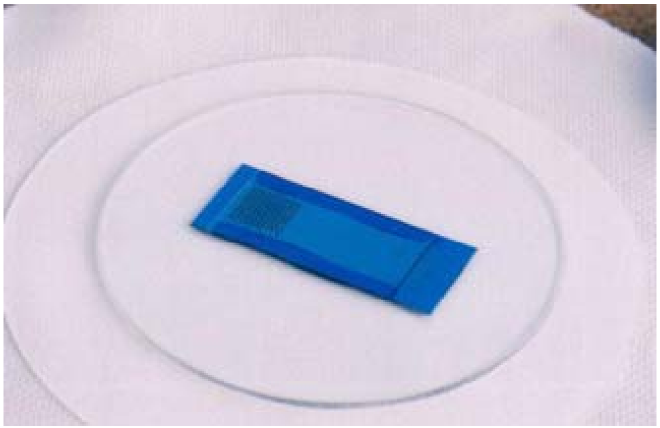

Figure 3.1 The Electronic tongue chip with fluid guide[13].

substrate, can contaminate the fluid. For these problems, Sohn et al have developed a more effective substrate topology for better fluidic flow by using capillary forces. This capillary pump is realized by placing a hydrophilic film on the substrate to enhance fluid passage. The thin gap between cover glass and substrate creates an effective capillary pump [13].

In the meantime, the author approached with another way to solve problems mentioned above. The author and Y.S Park suggested using thin microfilm ‘fingers’ for capturing beads into their pits without using slide cover glass. Effectively, it is no longer required to attach the cover glass. This process is a kind of a monolithic process, which reduces the arduous process of attaching the cover glass to the single monolithic micromachined device[16,17].

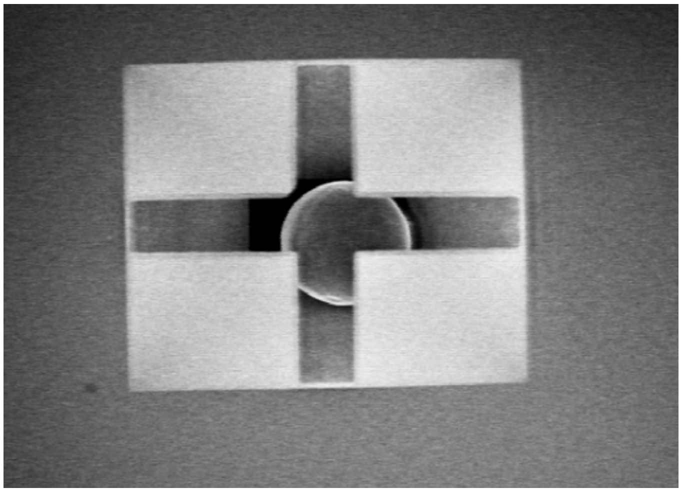

.

Figure 3.2 Bead captured in microfilm cover.

3.2 Fabrication of springboard structure

The finger, which was named when it was fabricated for the first time, came to be called a springboard to emphasis its deflection characteristics. The springboard structure is based upon the anisotropic etching profile of a bulk silicon substrate. Referring to the previous chapter, the silicon crystal has a different etch rate depending on its orientation.

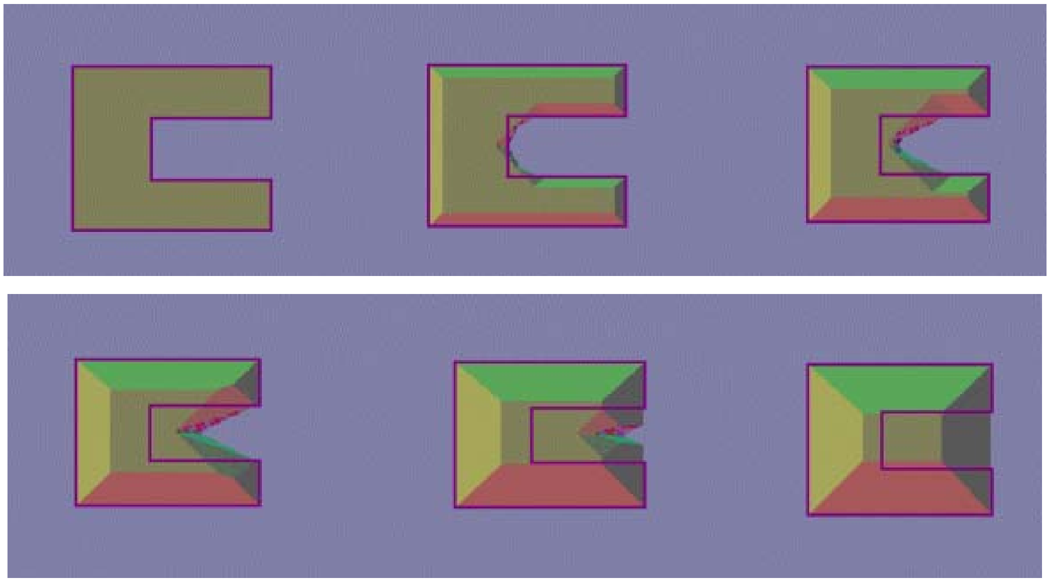

Figure 3.3 Etching simulation of concave opening mask[18].

In the case of etching a convex mask opening, anisotropic characteristics bring about undercutting below the insoluble mask layer as we can see in figure 3.3. This simulation was performed using the ACES simulator from the University of Illinois at Urbana-Champaign [18]. Each drawing represents a thirty minutes time gap at an etch rate of 1.4micron/min in the (1 0 0) direction. The structure shown in figure 3.2 is also the result of this anisotropic etching characteristics. Many MEMS structures such as cantilevers to complex bridges can be fabricated with this technique.

However, there were several problems to be solved in fabricating the springboard structure. First, a single layer of silicon nitride film cannot be used as a springboard material because of its tensile stress. This stress can induce deformation or crack a cantilever beam or other MEMS structures. Figure 3.4 shows the stress level of silicon nitride film and silicon oxide film. While silicon nitride has tensile characteristics, silicon oxide shows compressive stress, which enables stress compensation[19,20].

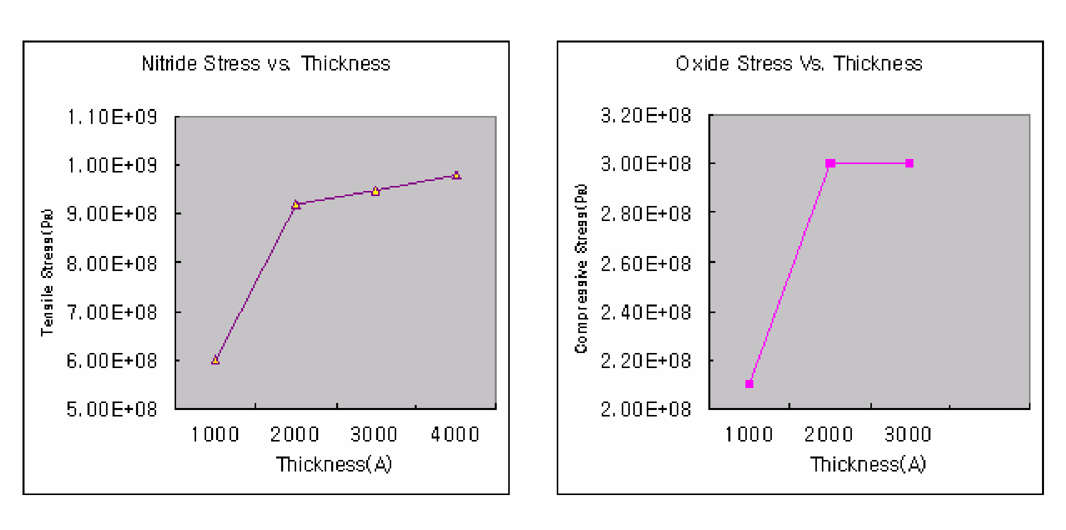

Figure 3.4 Illustrations of stress as a function of thickness for LPCVD[19,20].

A composite film stack of silicon oxide film and silicon nitride film can reduce the overall stress level by thickness matching. For this case, the film should be insoluble to potassium hydroxide so a triple layer of silicon nitride-silicon oxide-silicon nitride was adopted. Equivalent residual stress of a multi film stack can be calculated using the equation

$$\sigma_{eq} = \frac{\sum_i \sigma_i \cdot h_i}{\sum_i h_i}, \qquad (3.1)$$

where σ is the residual stress of the i_{th} film, and h is the thickness of i_{th} film.[19,20]

Also, a similar approach can be used to calculating the Young's modulus of film stacks. From the equation (3.1), the thickness combination of 1:6:1 (SiN-SiO-SiN) results in the least residual stress without considering any other factors. Figure 3.5 is the diagram of this stress relieved multi stack film.

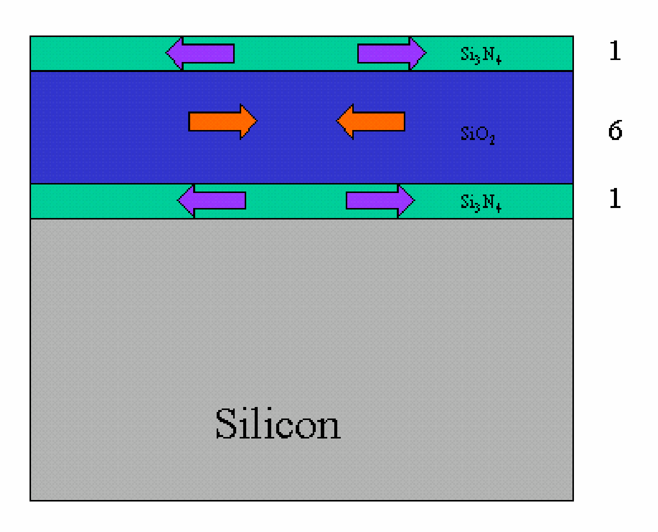

Figure 3.5 Illustration of stress relieving sandwich film stack.

The equation shows 1:6:1 ratio results in the least residual stress. Meantime, another factor to consider when choosing a film stack ratio is Young's Modulus. It describes the elastic properties of a solid undergoing tension or compression in only one direction. Young's Modulus is a measure of the ability of a material to withstand changes in length under lengthwise tension or compression [21]. From the data of the author's various trials, 1200Å -7200Å -1200Å stack proved to show the best survival rate for a springboard structure. Figure 3.6 shows the diagram of calculated stress level with equation (3.1).

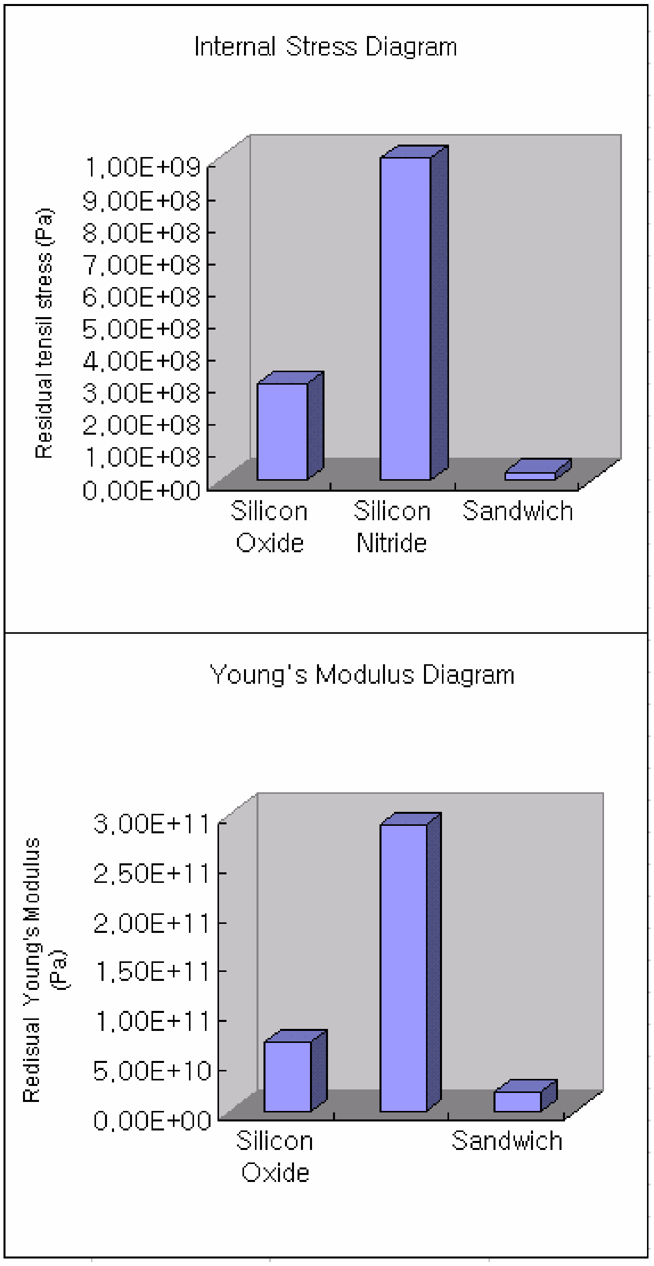

Figure 3.6 Illustration of residual stress and Young’s Modulus calculated by equation (3.1).

This diagram shows that residual stress is dramatically reduced in the ratio-matched composite multi stack film. For the composition of 1200Å-7200Å -1200Å film stack, residual tensile stress is reduced to 0.025 GPa. That is two orders lower than that of single layer. In the case of Young's Modulus, it is reduced to 20Gpa, which is one order lower than that of a single silicon nitride film. Young's modulus plays a very important role in bending of springboards, and the search for appropriate composite ratio and thickness is continuing.

In the case of low stress nitride film, Si_xN_y, they are known to be used by itself with their low stress characteristics. From references, Si_xN_y layer has much lower stress level compared with normal nitride film: stress is 100M Pa~300 M Pa and Young's modulus is 100 G Pa. As using equation (3.1), we can get very low stress level film with very thin oxide film level with triple layer method, or even use a single nitride film structure due to its low stress level. With triple layer methods, we could get less than 100MPa stress with 1:1:1 mixture. However, as the author tested several thickness low stress silicon nitride films as shown in references, the yield was not successful as written in references. One important condition of low stress silicon rich nitride film is deposition temperature of over 900°C. The author could not apply in the fabrication facilities in the University of Texas at Austin Micro Electronic Research Center has not obtained a deposition temperature over 900°C. So far, the author has not obtained good yield for a single layer silicon rich nitride film structure.

In the case of silicon nitride-oxide-nitride triple layer, the author had pretty good yield compared to silicon nitride only structure or triple layer with normal stress nitride film. To compensate film stress described in references[19,20], it is recommended to use 1.5:1:1.5 ~ 1:1:1 layer, which is much thinner triple later compared with 1:6:1 layer. The benefit of this low stress nitride film sandwich structure layer is that we can establish thinner total structure layer for etching using a simpler masking process, all with better yield.

The layer of 1:6:1 ratio springboard structure uses a composite layer with a thickness of at least 7000Å.

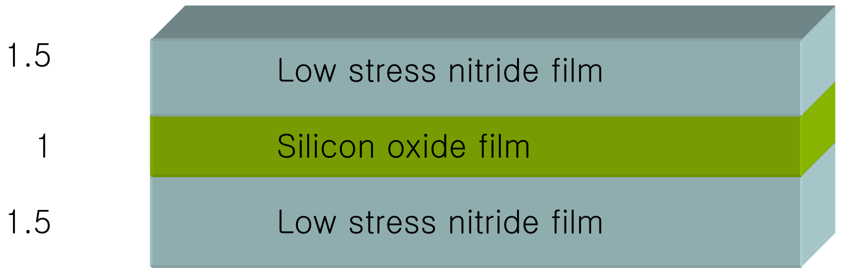

3.7 Stress relieving sandwich structure with low stress nitride film.

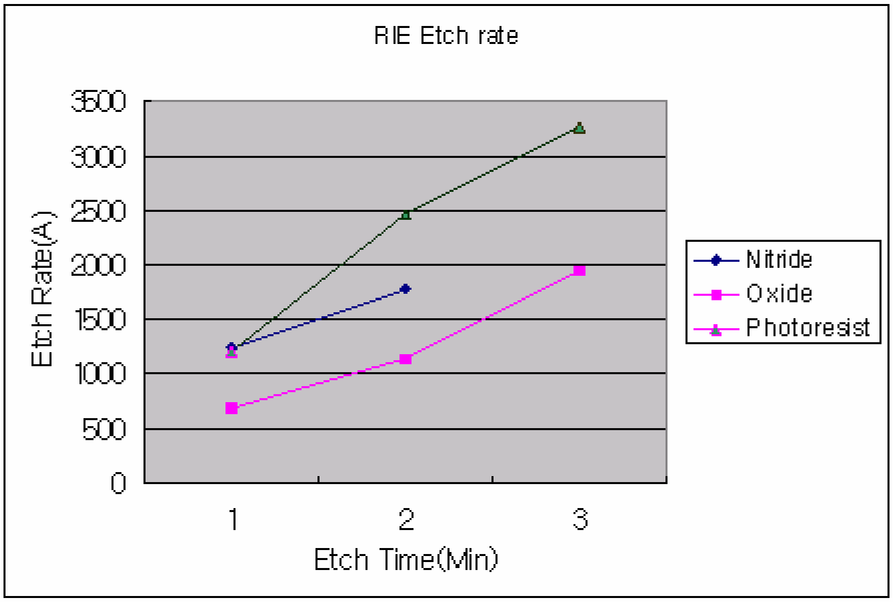

Figure 3.8 RIE etch rate chart ($CF_4 + O_2$ at 200W).

For the fabrication of the springboard, the problem begins with RIE mask layer etching. Figure 3.8 shows the RIE etch rate of the silicon nitride layer, silicon oxide layer, and photoresist layer. The etch rate of photoresist is higher than 1200Å/min while that of silicon oxide is 600 Å /min. We used the photoresist AZ5214. AZ5214 gives a thickness of 1.4 micrometer when spun at 4000 rpm for thirty seconds. Looking at the etch rate graph in Figure 3.8, photoresist can be used for the RIE etch mask for less than 6 minutes under the condition of $CF_4 + O_2$ at 200W. In the case of composite 9600 Å multi stack film layers, it is problematic to use AZ5214 as the RIE mask. Figure 3.9 shows the result of photoresist overetching. Even if only the top silicon nitride layer is overetched, this layer cannot be used as a structure layer because the silicon oxide layer in the middle will etch in the KOH solution. Referring to the graph in figure 3.8, it takes at least 14 minutes to dry etch the composite multi film with thickness of 14000Å. To overcome this problem, an e-beam evaporated aluminum layer is adopted as an RIE mask before the low stress nitride thinner sandwich layer was adopted in our process.

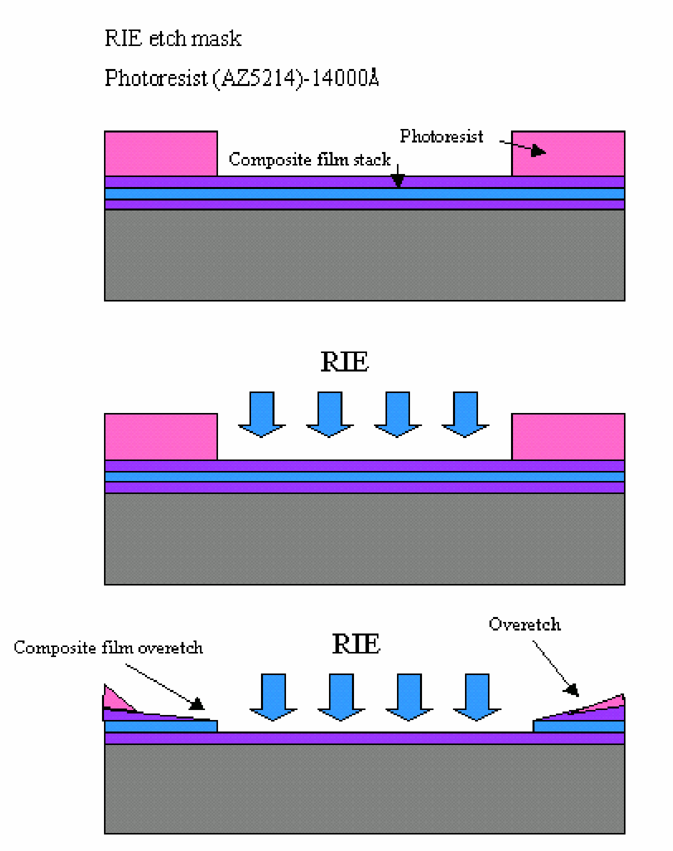

Figure 3.9 Illustration of RIE overetching.

The author deposited several different thickness ratios for testing with results shown in tables 3.1 and 3.2. In University of Texas at Austin Micro Electronics Research center,

silicon nitride furnace has flow rate of 100 sccm Dichlorosilane gas, and 300 sccm ammonia(NH3) gas. Normally silicon nitride film deposited in the flow rate of DCS (Dichlorosilane) gas of 20%, and Ammonia flow rate of 23%, which creates Si3N4 layer, which has high stress. Table 3.1 has composition mixture of Si3N4 film and Silicon Oxide film triple layer. Our favorite film composition is 1:6:1, which is close to #5 in table 3.1. That film gives best yield on creating flexible springboard structures.
The low temperature oxide furnace is set to 300 sccm of O2 and 25 sccm of SiH4, and we use flow rates of 10% of O2 and 99% of SiH4, which is almost 1:1 ratio in the furnace. The yield in Table 3.1,3.2,3.3 is a survival rate of springboard structures in a single wafer.

Test #	Silicon Nitride layer thickness(Å)	Silicon Oxide layer thickness(Å)	Silicon Nitride layer thickness(Å)	Yield
1	1500	11500	1500	~50%
2	820	7157	780	<30%
3	1500	8500	1500	~50%
4	1300	7500	1300	~50%
5	1300	6500	1300	<70%

Table 3.1 Tripe layer composition and Yield, with Silicon nitride film.

Test #	Silicon Rich Nitride layer thickness(Å)	Silicon Oxide layer thickness(Å)	Silicon Rich Nitride layer thickness(Å)	Yield
6	1500	3000	1500	~50%
7	2000	3000	2000	~50%
8	1500	2000	2000	<70%
9	2000	1500	2000	<70%

Table 3.2 Triple layer composition and Yield, with Silicon rich nitride film.

However, #5 film brings about some trouble using the AZ5214 photoresist as the RIE etchmask as described in Figure 3.9. On the contrary, the triple layer with silicon rich nitride film has similar yield with much thinner total thickness. This thinner thickness enables the use of a single layer of AZ5214 photoresist as a good etchmask during RIE. The author used #8 and #9 triple layer structures to create bead size selection chip discussed in chapter 4.

Sample #	Silicon Rich Nitride layer thickness(Å)	Temperature	Yield
A	4500	790°C	<80%
B	4500	790°C	>50%
C	5000	840°C	~50%
D	10000	840°C	<85%
E	7500	840°C	<70%

Table 3.3 Yield of silicon rich nitride structure.

While the author used a triple layer as a main structure film, Y.S Park in our group also tried single layer of silicon rich nitride film as a structural layer. Samples A and B were tested by the author in the past using. The 6 inch CVD chamber with same flow rate, except for temperature. Sample A gave good yield, almost 80%, while Sample B, which is exactly same condition, showed poor yield, less than 50. As the author tried the same experiment several times, the yield continued to fluctuate. The author suspects the temperature the chamber was not repeatable. While the author was not successful with single layer structure, Y.S Park was very successful in creating good yield structure made of silicon rich nitride film using our 4 inch CVD furnace, with the temperature of 840°C. According to his experimental result, sample D showed 100% yield while thinner ones are not very successful. As D recipe proved to be a stable one, our process would be much simpler as before.

In the ACES simulation tool, the standard KOH etch rate is 1.4 micron/min. According to this standard, it takes about 3 hours to etch through a wafer with the thickness of 270 microns. For that etch rate, KOH temperature should be set to around 92°C, which results in the breakage of every springboard pattern on the silicon surface. As KOH etches the silicon crystal, hydrogen gas is produced. The amount and the intensity of gas production are proportional to KOH temperature. Even at the temperature of 79°C, the survival rate of springboards is lower than 50%. The best way to get high survival rate is to etch the wafer with the lowest possible temperature. The author fabricates springboard chips at the temperature of 60°C for 20 hours, and this gives the best survival rate at any film thickness.

3.3 Summary

Micromachined bead confining structure is developed from basic sensor chip. A mixture of silicon nitride and silicon oxide film works as the etching mask for bulk silicon substrate etching as well as flexible structures which confine installed beads in cavities. This novel idea eliminates some of the problems in the basic electronic taste chip structure.

To have better yield of bead confining finger structures, the study of CVD films and etch methods has been discussed in this chapter. In the next chapters a size selection chip is discussed.

Chapter 4 MEMS based size selection method

4.1 Motivation of size selection method

Each bead containing different chemicals needs to be placed in its appropriate place. This can be done using pick-and-place methods, but for beads in the sub-250 micron range, this can be mechanically complex. Here the author proposes a novel method to pick beads easily as well as place them in correct places. If each bead size is derivatized in a different fashion, then each size bead becomes a different analysis site. By designing different sized openings over each well it should be possible to construct self-assembling bead arrays with multi-analyte sensing ability.

To accomplish this, the bottom and top should be controlled independently. The top window size is controlled by an etched thin film window, while bottom window size is dependent upon the etch window and wafer thickness. For a (1 0 0) silicon wafer, the bottom opening window size follows this relationship :

$$\textbf{Bottom size} = \ell - 2t \cdot \cot 54.74^\circ \quad (1)$$

, where ℓ is distance between etch window shown in figure 4.1.1, and t is wafer thickness, 54.74° is the angle between (100) face and (111) face, where anisotropic etch stops. Each well accepts beads whose diameters are smaller than the top window. At the same time, bottom opening passes beads whose diameters are smaller than the bottom opening.

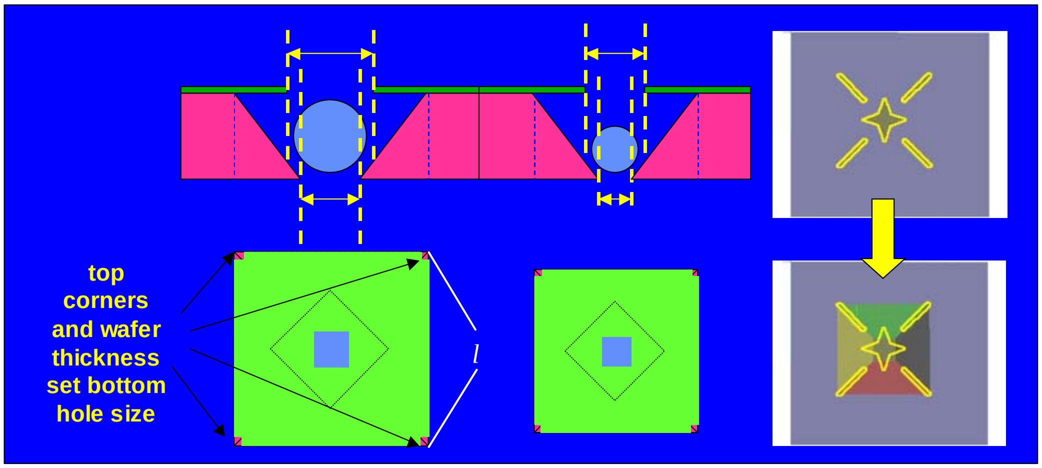

Figure 4.1.1 Illustrations of the size selection unit.

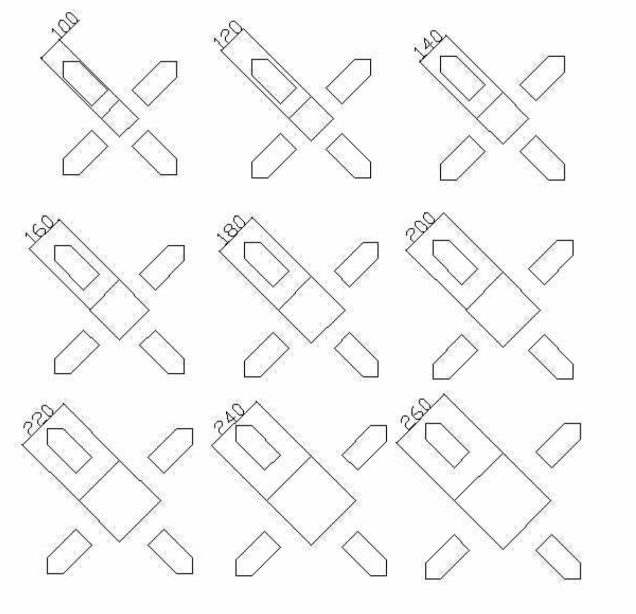

Figure 4.1.2 Prototype single side bead size selection chip design.

4.2 Statistical approach of size selection method

The feasibility of this approach is critically influenced by the fact that bead sizing is never exact. Based on Gaussian distributions of sizes, it is possible to expect errors made in self-assembly using different sized beads.

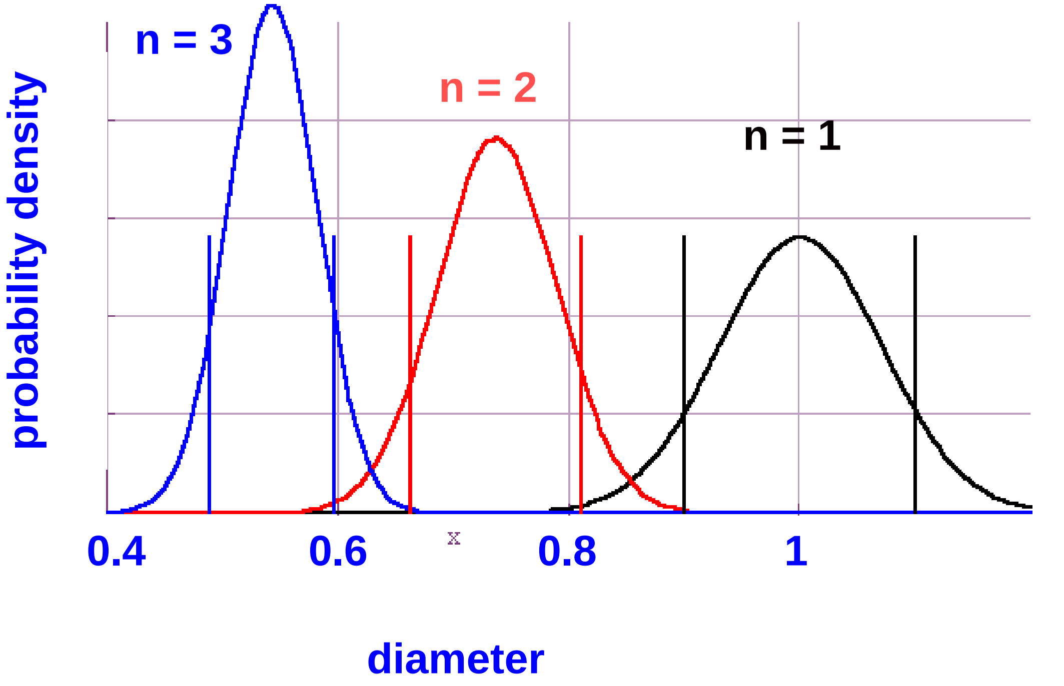

Figure 4.2.1 Overlap between different size-selective finger designs.

Figure 4.2.1 shows three different size beads' Gaussian distribution curves. Each bead size (median-μ_x) has variance of σ_x, and constant percentage is called coefficient of variance, $CV=\sigma_x/\mu_x$. As bead size gets bigger, CV gets bigger and then the Gaussian distribution curve spreads wider. Each top and bottom window works as a perfect filter. In this graph, an error means tailing over into the neighboring bottom/top filter. For examples, in 'n=1' beads' distribution curve, the left tail passes the center curve's top window diameter. That tail overlap means the possibility of mis-placing of 'n=1' beads in ‘n=2’ well. Likewise, ‘n=2’ curve’s tail passes over the diameter of ‘n=1’ well’s bottom window size. This is the possibility of mis-placing of ‘n=2’ beads in ‘n=1’ well. These errors are deeply related to how much separation distance each μ_x has. Figure 4.2.2 shows 1σ separation between top window size and neighboring bottom window size.

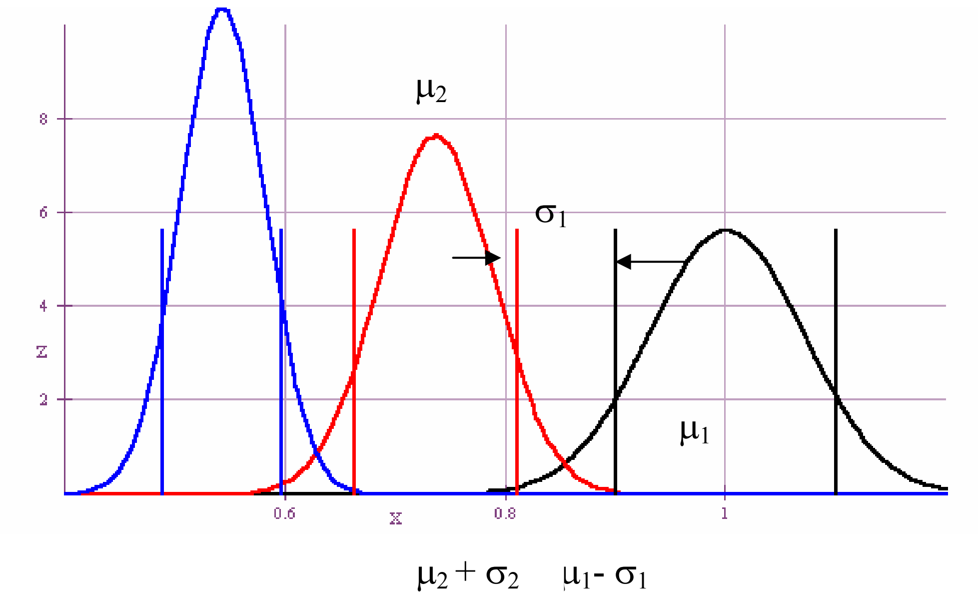

Figure 4.2.2. 1σ Separation case.

In this case, probability of mis-fill is around 3~4%. If we increase separation width by 2σ, this probability drops by one tenth. But 10^{-3} is still a high error rate so we need to find another method to reduce this error to order of 10^{-5} or less.

Here we suggest one more step before size selection process. A pre-sorting process would reduce these errors dramatically. If we filter whole Gaussian μ_x size beads by 2σ width pre-sorter chip, the tail of Gaussian distribution curve will disappear and change its shape to a truncated bell. If we perform this pre-sorting process over and over, distribution of beads will change from its original distribution N (μ_x, σ) to N (μ_x, $\sigma/4$). It is equivalent to having 4σ separation between neighboring top and bottom window sizes, whose mis-filling rate is normal distribution probability P {X>8σ}. This means it "statistically never happens" in the real world. At the same time, this pre-sorting process enhances the resolution of separation in a chip. Number of maximum size selectable beads in a chip is proportional to the size of σ. Because we could reduce σ by four by pre-sorting method, this number also gets larger by factor of two and more. Nonetheless, the number of differently sized beads that can be used in a size selection chip is probably limited to less than 100 when considering various practical constraints.

Separation	**Next size up mis-fill possibility**	**Next size down mis-fill possibility**
0σ	10.56%	11.51%
1 σ	4%	2.8%
2 σ	0.87%	0.13%
3 σ	0.01%	0.01%
4 σ	0%	0%

Table 4.1. Mis-fill possibilities Vs. separation factor.

However, there is a threshold to pass for higher error correction performance. For precise bead sorting system, precisely controlled bottom and top windows are an indispensable factor. In the current system, bottom opening size is dependant on a poorly controlled factor: wafer thickness. The tolerance on wafer thickness is mainly controlled by the wafer vender. As wafer tolerance gets smaller, the price gets higher and higher. Even if we get minimum variance thickness wafers available in market, its tolerance is only about 5%. From the formula (1) on the previous page shown, we can calculate how much error the bottom size can have.

$$\textbf{\% Bottom size error} = \frac{2t(0.01\rho)\cot 54.74^\circ}{l - 2t\cot 54.74^\circ} \times \mathbf{100} \qquad \textbf{(2)}$$

, where ρ is wafer thickness tolerance

As we can see from **(**2**),** 5% wafer thickness variance results in 18% window size error. Reducing this error is absolutely required.

4.3 Double side aligning process

The errors due to wafer thickness variance are inevitable. If we could create well-aligned square size selective membranes on the bottom, this factor can be eliminated. As we could see from Figure 4.3.1, bottom selection unit is designed parallel to the bulk etching cavity.

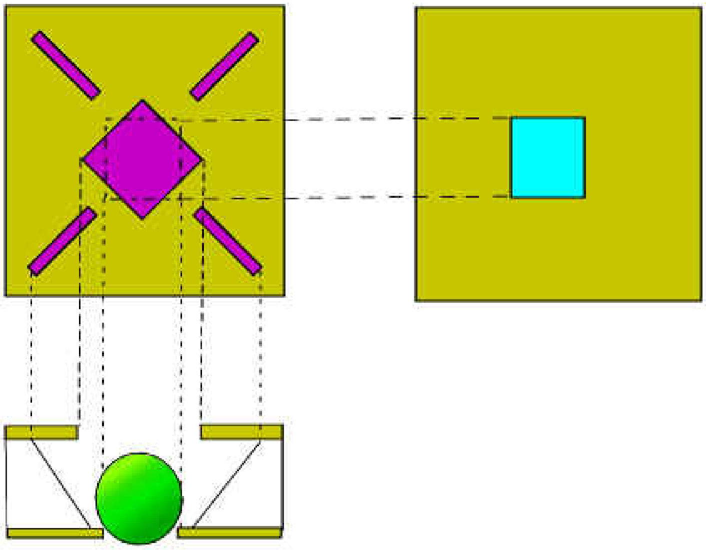

Figure 4.3.1 Illustrations of double side size selection unit.

In designing of the double side process, cavity-creating etch window should be designed bigger than one-side process to eliminate the possibility of blocking of bottom selection unit by bulk cavity underetch. Figure 4.3.1 is the illustrations of bulk micromachining etching process when it has an etching window on both the top and the bottom. As KOH etches through top and bottom side, a big pyramid from the top and a small pyramid from the bottom are produced. They create a cavity which is normally bigger than single side etch structure. However in a bad case, if the wafer thickness is too thick, then the bottom hole can be blocked by substrate as shown in Figure 4.3.2. On the contrary, over-etch affects more on single-side process. A over-etch of single side membrane size selection chip can increase the size of bottom window, which bring about failure of bead sorting ability.

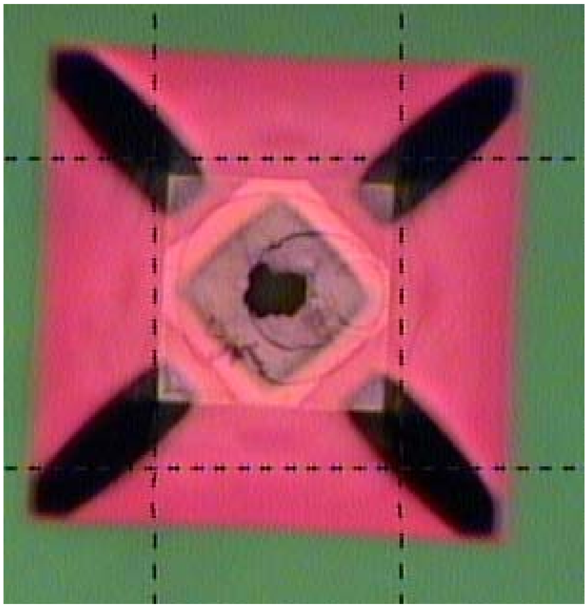

Figure 4.3.2 Example of under-etch cavity.

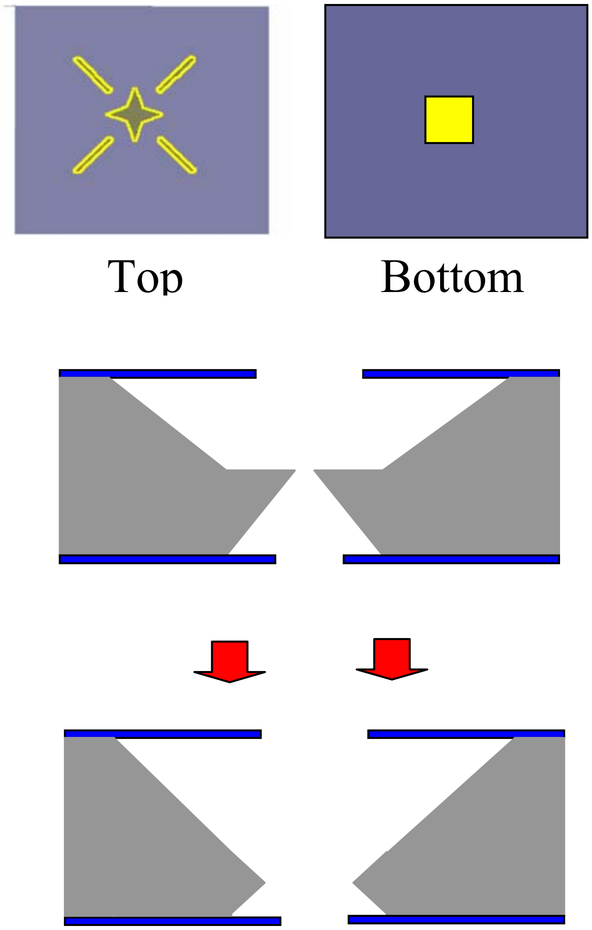

Figure 4.3.3 Diagram of double side etch result.

As mentioned above, the double side process gives better results than the single side process. However, the double side process does not require significantly more processing than the single side process. When we deposit film for the top layer, the bottom side also has the same film. The double side process does not require additional film deposition steps. It only requires one more photolithography step on the other side.

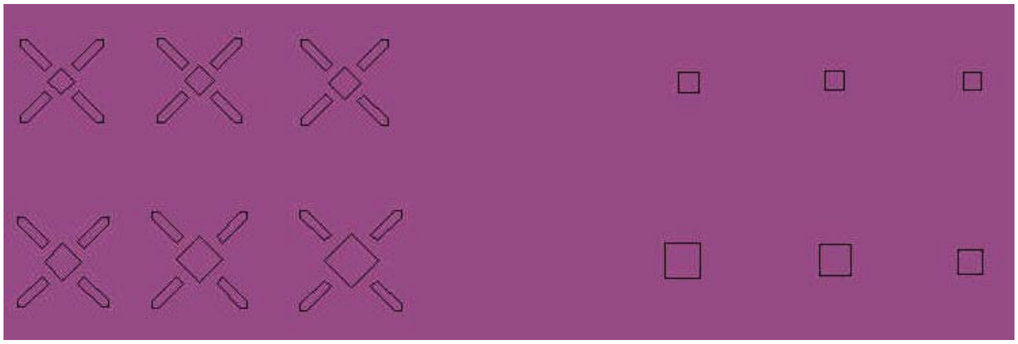

Figure 4.3.4 Double side process photomask.

Figure 4.3.4 is a part of an actual double side photomask. The bottom units are drawn like mirror images of top units. The double side aligner stores the optical image locations of front side registrations. After slight developing of front side after exposure, the backside is aligned by saved registration marks stored in the computer system that is part of the double side aligner.

Once the backside exposure is over, the rest of the process is the same as the single side process, with the addition of a backside RIE process for backside hole opening. In fact it is not an addition of a process step because in single side process, we have to RIE etch of the membrane in the backside after wet etching. While stripping off the bottom layer, top unit structures tend to be damaged by plasma passing through bottom holes. In the worst case of overetch, top structures get so fragile that they cannot perform appropriate function as bead size filter.

Figure 4.3.5 shows the actual pictures of size selection top and bottom units for one cell. Top unit shows a square coming from bottom. This reflects the cavity shape under the top sorting unit. Also we could see a slight shining square around bottom unit picture, which shows silicon substrate etch ends a few tens of microns from the bottom unit. This cell can select beads between 100μm to 110μm in diameter.

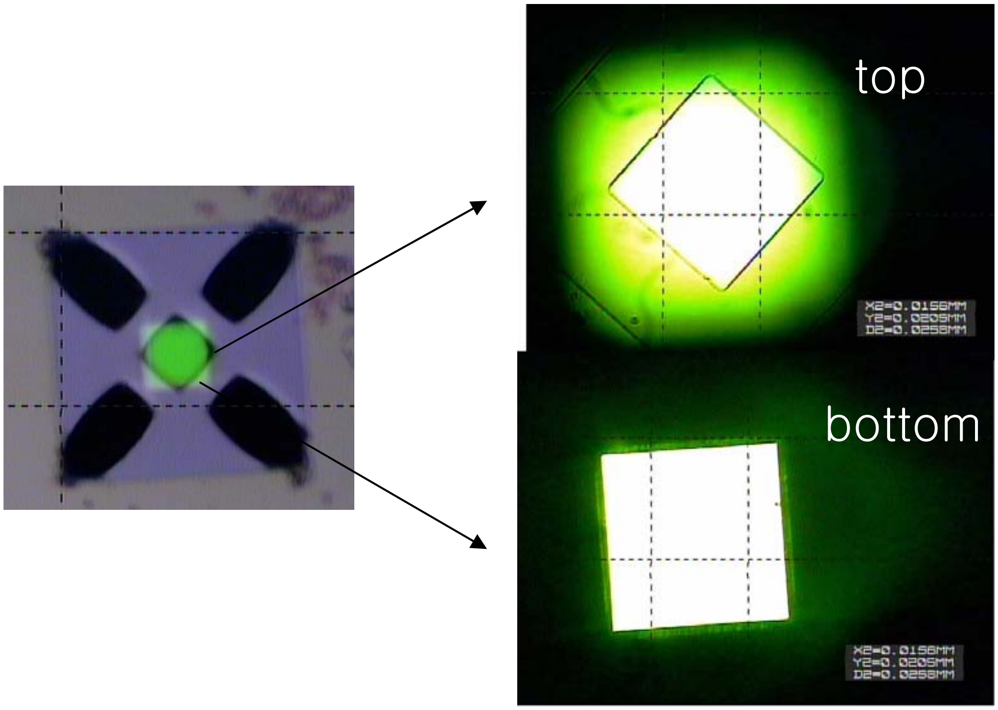

Figure 4.3.5 Picture of size selection unit, the top and the bottom units.

4.4 Demonstration of bead size selection method

As the author pointed out earlier in this chapters, the beads used are too small to handle like picking up a single ball and placing it simply. Traditional method of bead handling use automatic pipette to pick up beads in the water and move beads into the pits with a needle. Handling single beads also needs a process of separating beads attached to each other. Bead size sorting method can solve three problems in bead placing:

1. bead separation issue
2. mis-filling issue
3. bead confining issue

To verify the feasibility of size sorting method, the author simulates bead sorting with glass beads instead of polymer gel beads to see the feasibility of size sorting since glass beads are sold sorted by accurate size. Bead size selection experiment videos are captured and are shown in sequence for easier understanding of this method.
Secondly, the author will show the result of polymer gel bead size selection experiment. In that experiments, the author marks the agarose polymer beads with various fluorescent colors by each size and the result of bead size selection will be presented.

4.4.1 Glass bead size selection setup

The author could obtain about 4% CV(coefficient of variance) glass beads from Duke Scientific Corporations. Those beads are designed as spacers, insulators and reflectors. For bead size selection simulation, the author ordered seven different kinds of beads as shown in table 4.2. The beads are selected to have very small separation between neighboring size beads' minimum and maximum size to see the resolution of size selection chip. In our test, 100μm, 110μm, and 120μm beads have around one micron overlap on size range, which is statistically negligible number. Another four kinds of glass beads have pretty large gaps among each diameter range as many as ten to twenty microns.

For the dry bead sorting experiment, the author set a vacuum chuck with 8mm diameter size oil ring to cover all the sorting units at once. The vacuum system contained a needle value, filter, flow meter and pressure meter for control and measuring data. The needle valve actually controls the pressure and flow rate of the vacuum system. The filter is installed to absorb water and beads to prevent contamination of the in-house vacuum system. The flow meter and pressure meter are used to analyze the flow rate versus pressure of the plumbing network.

Beads are picked up using a tungsten needle with electrostatic force from the bead storing bottle. The author used a micro manipulator to control position of tungsten tip needle. The micro manipulator is capable of three-axis micro-scale positioning. This micro-manipulator makes it easier to deliver the glass beads attached to the needle between each size selection unit.

Diameter	CV*	σ
100µm	3.2%	3.2µm
110µm	3.8%	4.2µm
120µm	4.3%	5.2µm
140µm	2.5%	3.5µm
170µm	3.6%	6.1µm
200µm	3.5%	6.9µm
230µm	3.8%	8.7µm

Table 4.2 Glass bead size and distribution.

CV* = Coefficient of variance

4.4.2 Size selection experiment of dry glass beads

The installation of 100 micron glass bead on the size selection chip is demonstrated in this section. As shown in figure 4.4.2.1, the top sieve layer sorts out bigger beads while the bottom sieve layer passes away smaller beads than its sieve size. Figure 4.4.2.2 shows the size selection chip before dispensing of the 100 micron bead. The shining blur in figure 4.4.2.3 is the needle which is holding the glass beads. The needle carries hundreds of beads on its surface; by tapping the micromanipulator lightly the glass beads fall off the needle onto the chip surface. As the glass beads are released from the needle, they scatter and are pulled by air flow into the size selection units. Figure 4.4.2.4 shows this step, which looks as if glass beads explode onto the chip. While beads bombard the chip, some beads fall into the wrong size selection units and pass out the bottom sieve. Only the beads which fit designated size selection units stay there. As designated unit receives a bead, it does not receive any more beads because air flow is blocked by the first bead stored in that unit. Figure 4.4.2.5 shows successful bead settlement in top left unit. It can be barely observed in figure 4.4.2.5 that the bead is in the correct spot. It is clearly seen that the bead is settled in the middle of designated size selection unit in figure 4.4.2.6.

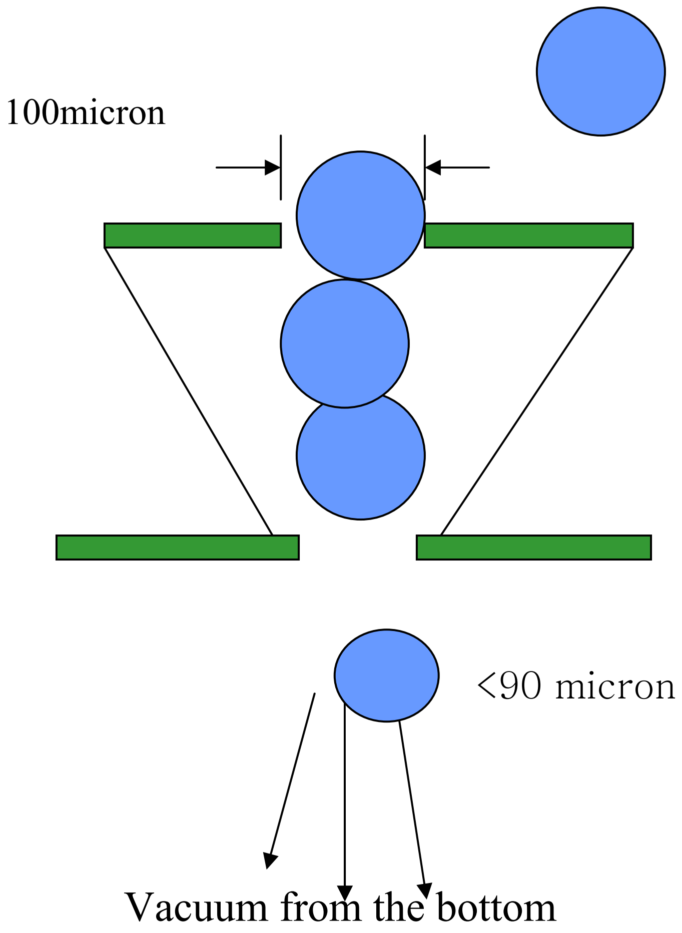

Figure 4.4.2.1 Illustration of vacuum bead installation.

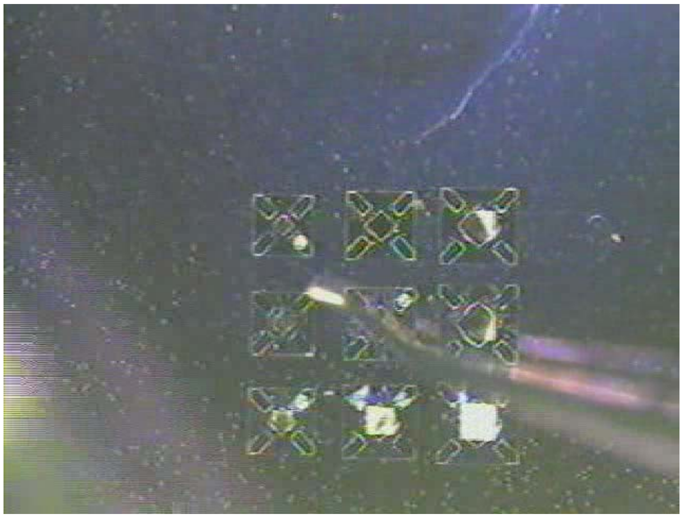

Figure 4.4.2.2 Before bead installation.

Figure 4.4.2.3 Needle with beads approaches on top of the size selection units.

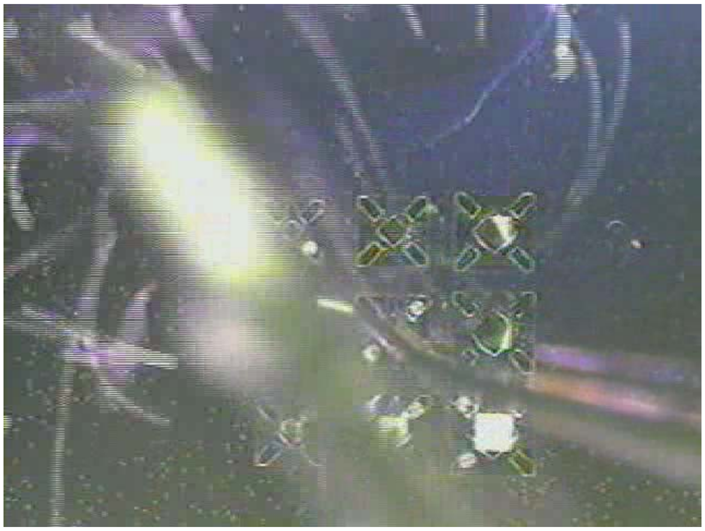

Figure 4.4.2.4 Beads bombard onto the chip(see left top unit).

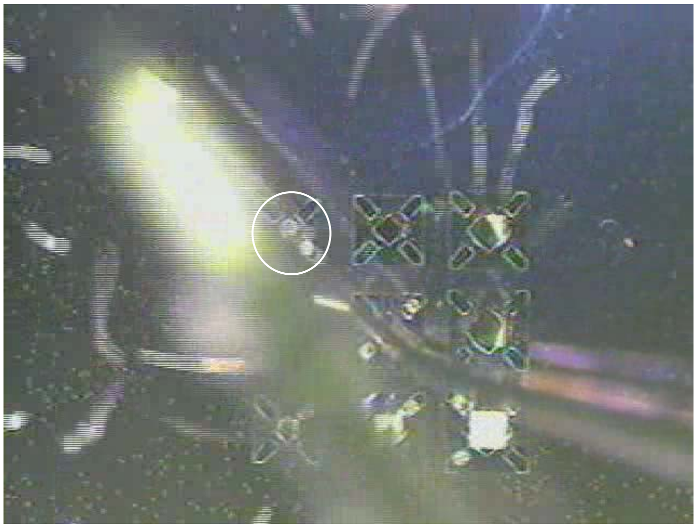

Figure 4.4.2.5 100 micron bead settled its designated place.

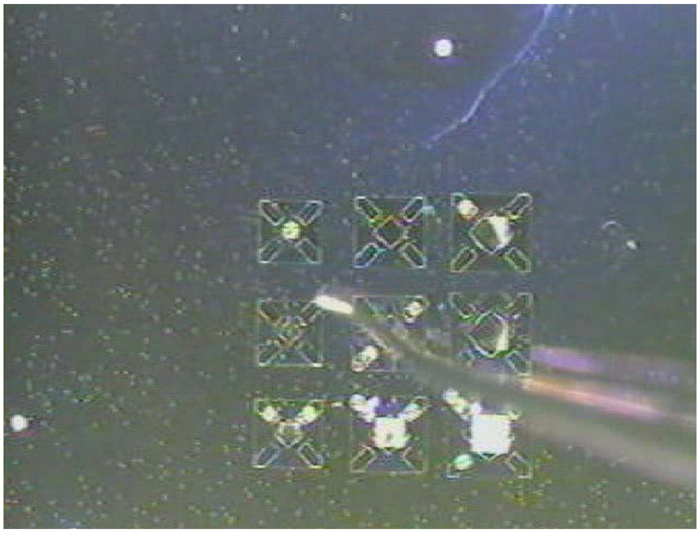

Figure 4.4.2.6 Bead installation successful.

The next demonstration is putting a 140 micron bead into its designated spot, on the bottom left. Before performing that, beads in the etch windows are swept away by sending strong air flow from side direction. In this step, it is observed that a 140 micron bead dropped from needle is drawn into the 140 micron size selection unit. The flying bead looks like a comet with a white trace line approaching into the right spot in figure 4.4.2.7 to figure 4.4.2.8. As is expected, size selection units which were already filled with a bead does not receive any more beads due to blocked air flow. Those beads that enter into the wrong places are passed away, too. Figure 4.4.2.9 shows bead installation performed well on 140 micron unit. From figure 4.4.2.10 to figure 4.4.2.12, excess bead removal is demonstrated. It is observed that beads in the bottom right are rattling in figure 4.4.2.11, and are blown away in figure 4.4.2.12.

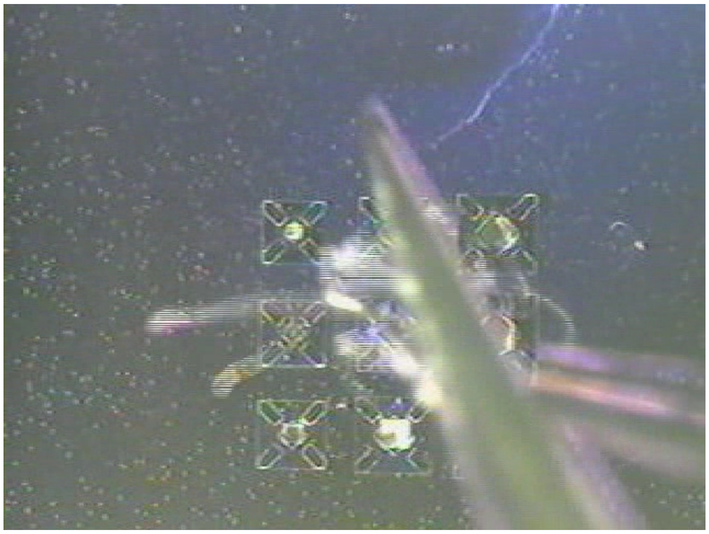

Fig 4.4.2.7 140 micron beads bombardment.

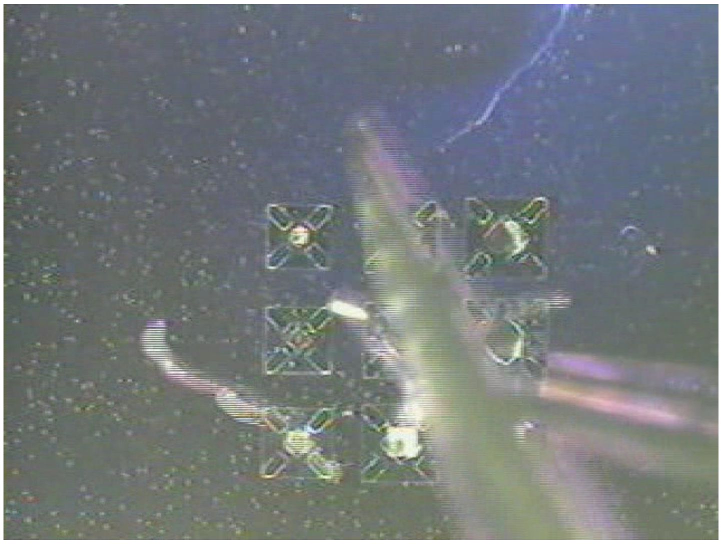

Figure 4.4.2.8 Bead trace approaches to 140micron spot.

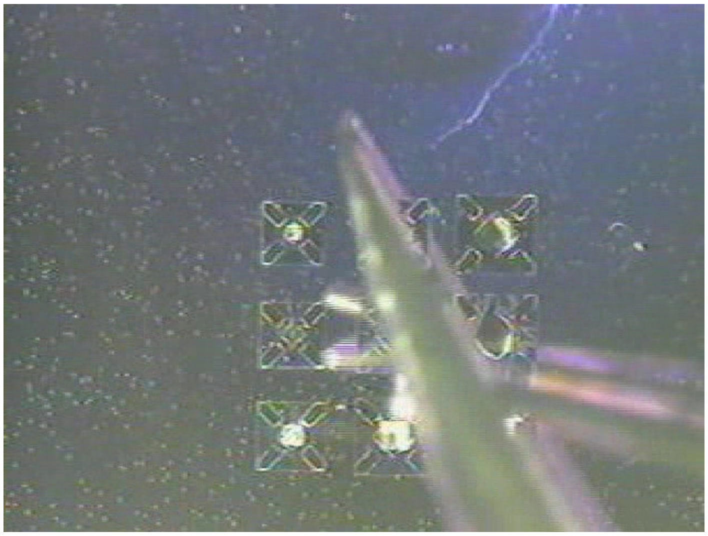

Figure 4.4.2.9 140 micron bead installed successfully.

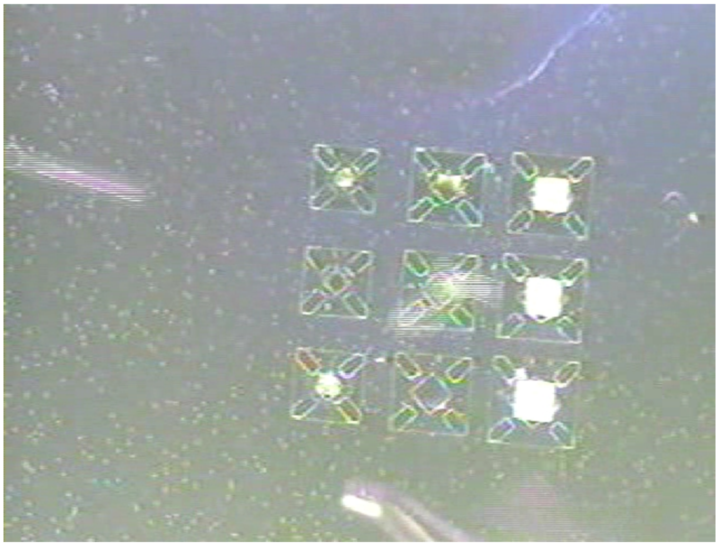

Fig 4.4.2.10 200 micron bead installing.

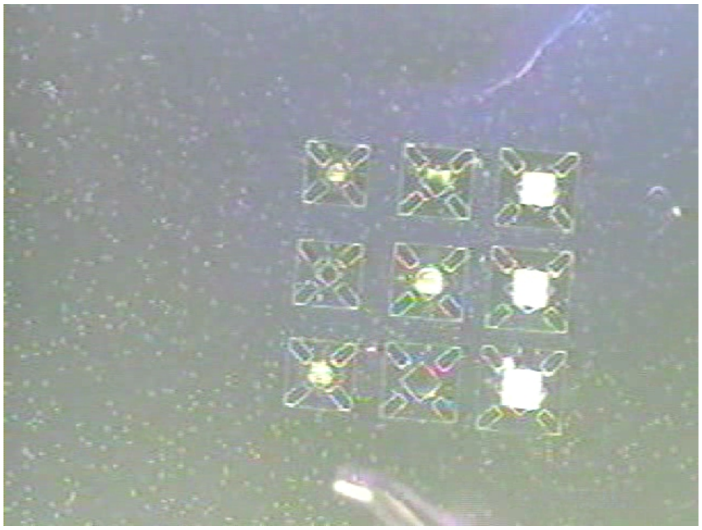

Fig 4.4.2.11 200 micron bead installed successfully.

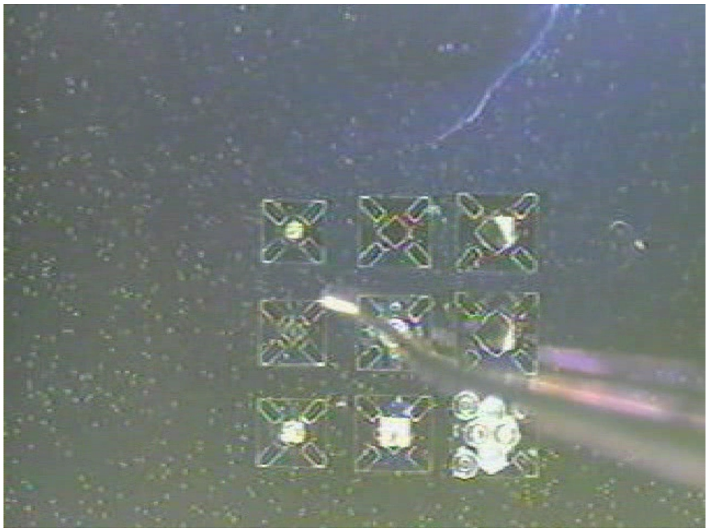

Fig 4.4.2.12 Getting rid of beads on top of the chip by side-air blowing.

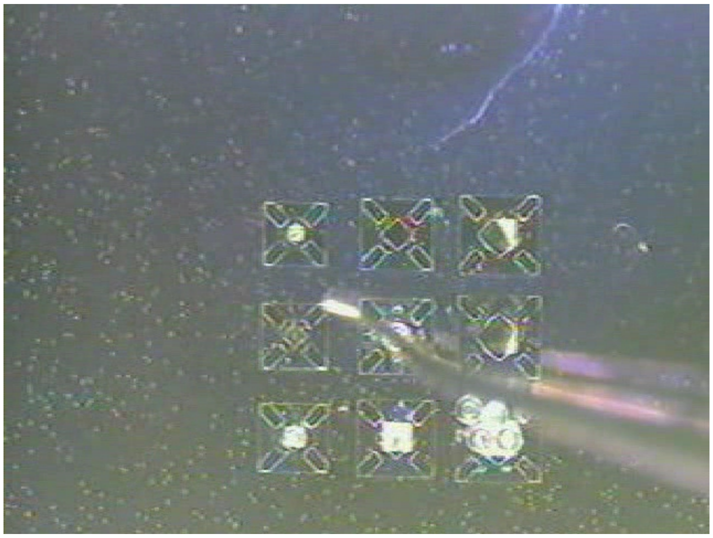

Fig 4.4.2.13 Bottom right beads are blown away.

The feasibility of bead size selection method is shown in these three different size glass bead installation demonstrations. Not only in these two experiments but also in every other experiment, the glass bead size selection method successful by caught designated beads into designated spots. Since the distribution of glass beads are well controlled by vendor, as long as the size selection units in the chip are not broken, beads of the proper size will be captured only in the desired location.

4.4.3 Size selection experiment in wet condition

Dry bead size selection demonstrations were performed successfully as described in previous section. Another approach to bead installation is demonstrated in this section in a wet condition. The author selected agarose beads in clean water as the size selection objects. Bead dispensing onto the chip is performed using a syringe as shown in figure 4.4.3.1. While dry beads scatter by tapping the needle, wet beads coming out of syringe tend to remain together. Sometimes it is difficult to observe bead installation due to sticky characteristics of wet agarose beads.

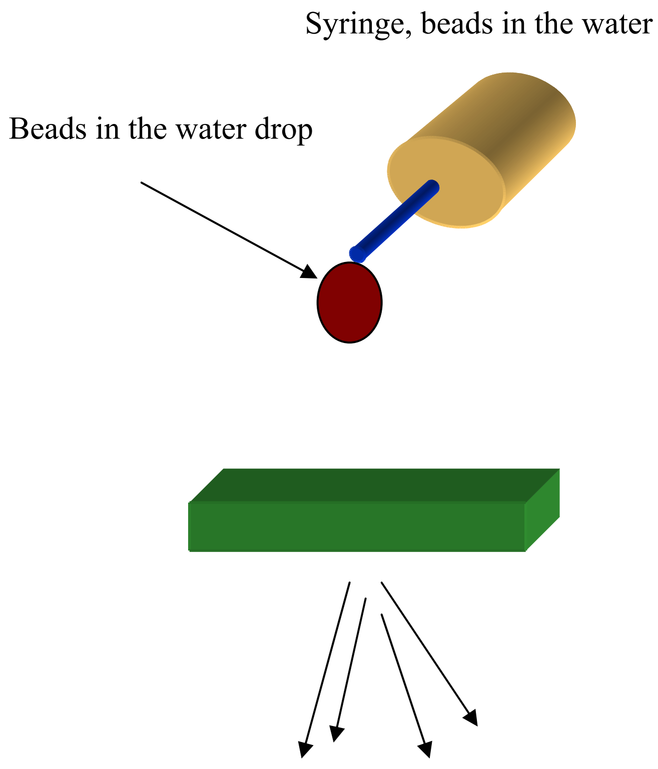

Figure 4.4.3.1 Illustration of wet bead installation.

In this experiment, the author used 160 micron size agarose beads provided by the McDevitt group, who are co-workers in the Department of Chemistry and Biochemistry. The designated size selection unit is mid-right unit in this 3 by 3 size selection chip. Figure 4.4.3.2 shows dropping of bead-water on the top of size selection chip. Figure 4.4.3.2 through figure 4.4.3.5, it is noticed that the designated size selection unit picked up the designated agarose bead. It is demonstrated that size selection units perform their role in both air and water.

Figure 4.4.3.2 Dropping of 160 micron agarose polymer beads.

Figure 4.4.3.3 Water is passing through sorting units.

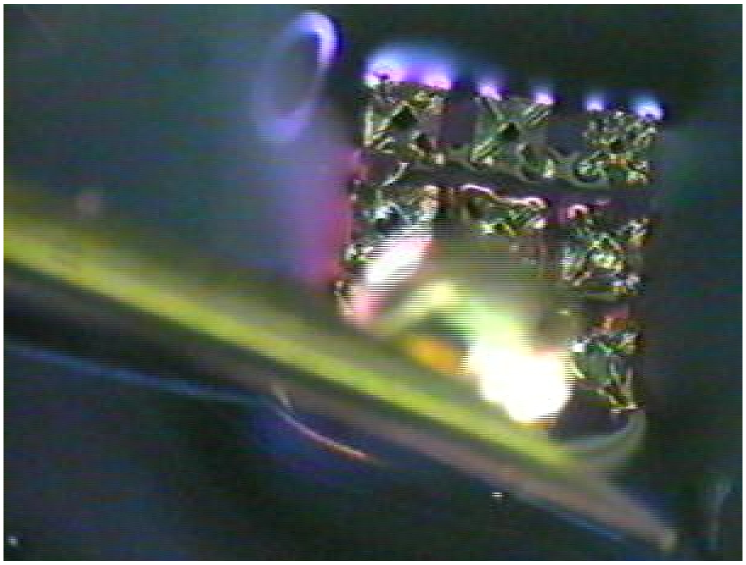

Figure 4.4.3.4 160 micron sorting unit captured bead.

Figure 4.4.3.5 Water in the surface is absorbed.

4.5. Size selection of the agarose beads with fluorescent marker

Throughout this chapter, the author described how bead size selection method is motivated, designed and performed. It is demonstrated in those dry and wet bead installation experiments that placing different size beads in the designated spot is possible.

In this section, the author presents the actual goal with each different chemical bead marked by bead size, and placing them into the designated place as shown in figure 4.5.1. These agarose beads are prepared by McDevitt group, sorted by biochemical sieve and dyed red, green and green with red speckles. Beads are dispensed using a pipette with water solution similar to the way the author used syringes on the vacuum chuck discussed in the last section.

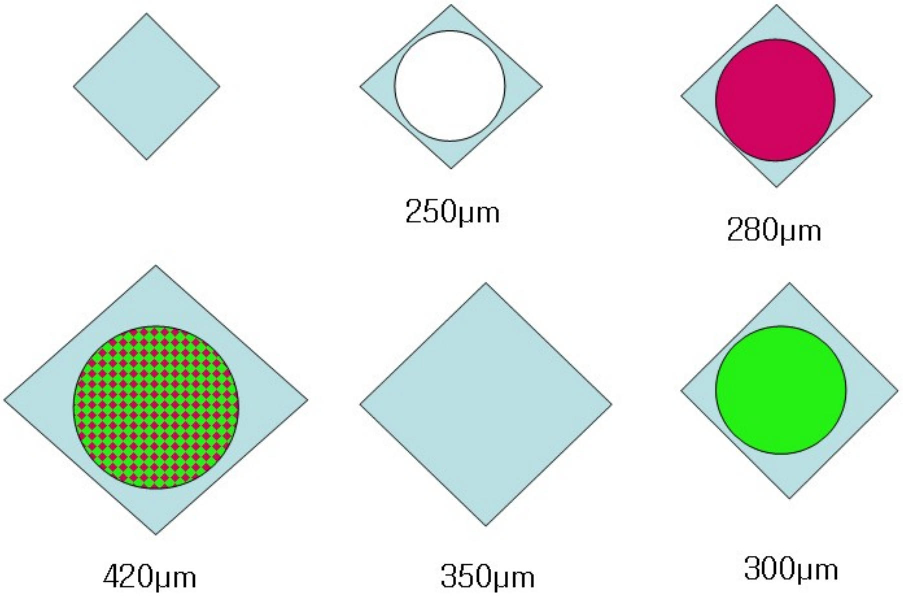

Figure 4.5.1 Bead size selection plan.

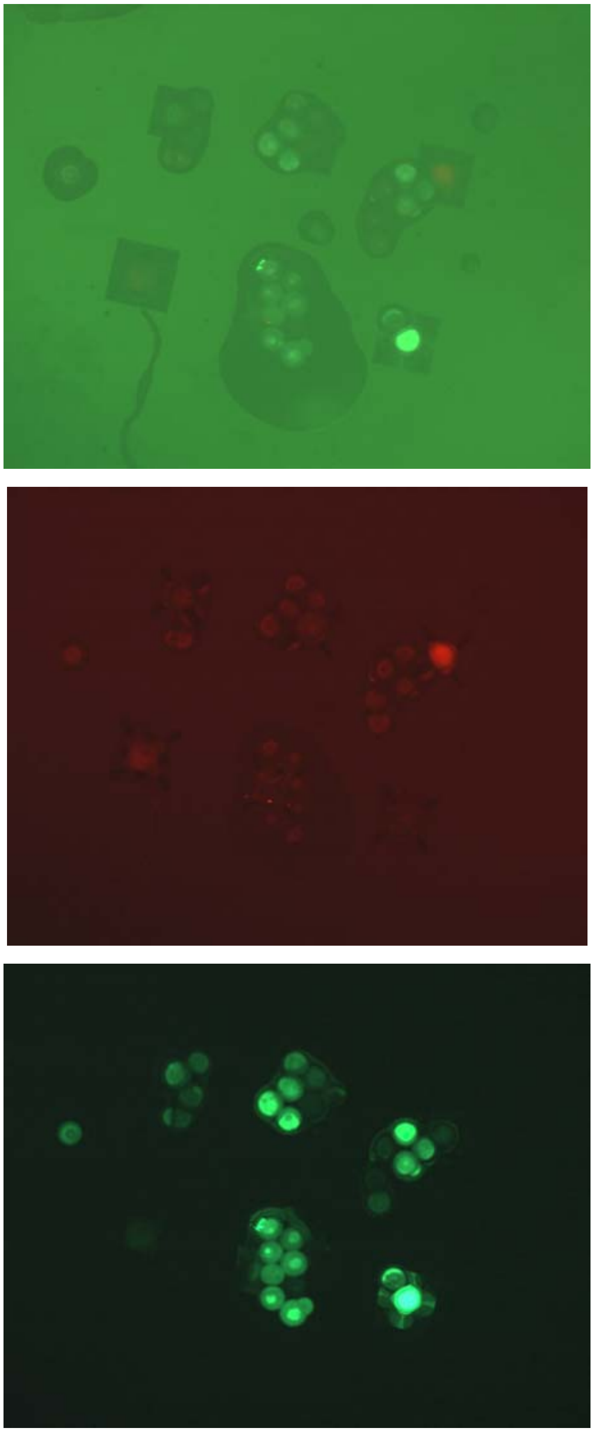

Figure 4.5.2 After putting 250µm, 280µm and 300µm beads under combo, red and green illumination.

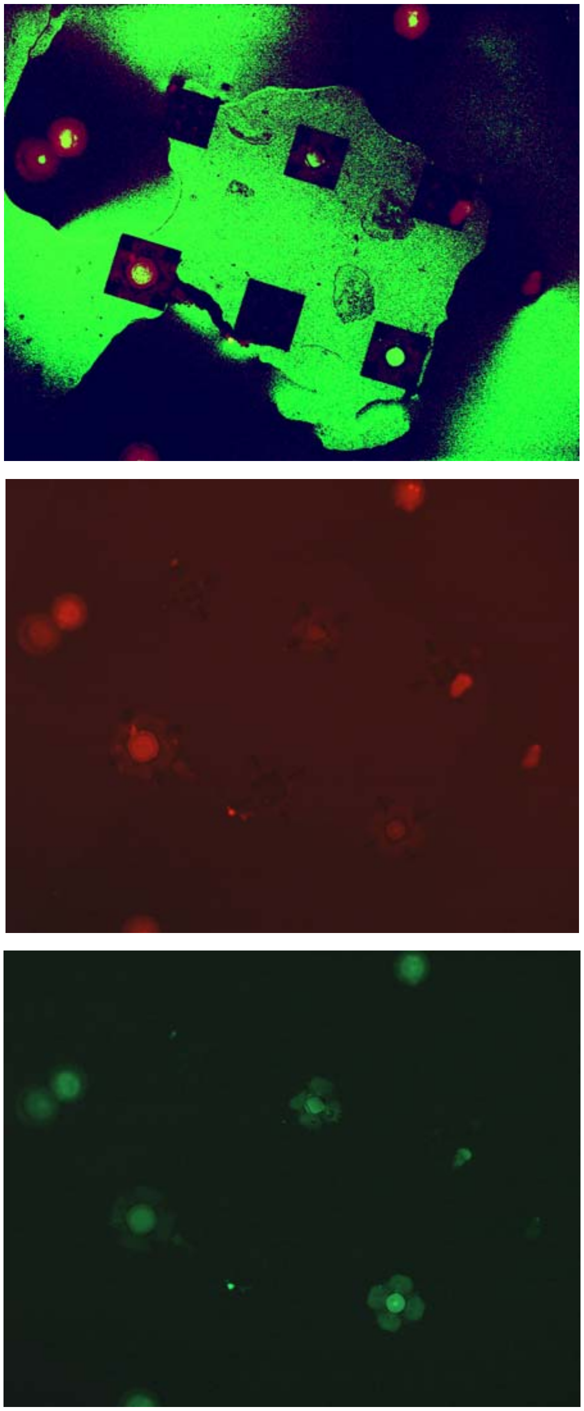

Figure 4.5.3 After putting 250μm, 280μm, 300μm and 355μm beads under combo, red and green illuminations.

Bead installation was performed in the same way as described before, from smaller size to bigger size. The author installed 250μm, 280μm and 300μm beads and took pictures under various fluorescent color illuminations. Figure 4.5.2 shows the result of size selection under various color illuminations. As planned in figure 4.5.1, natural bead, red bead and green bead installations were performed and figure 4.5.2 shows the result of those installation processes. Each bead becomes noticeable under its matching illuminations. After final bead installation, green with red speckle bead is discovered in its designated place as shown in figure 4.5.3. However, the red bead has disappeared in figure 4.5.3.

The loss of already-installed-bead happens repeatedly in every experiment of different bead size selection. As the same results repeat over and over, the author could reach the conclusion that this problem is not because of mistakes in experiments, but because the fundamental physics of size sorting method. In next chapter, the author will discuss this issue.

4.6 Summary

The size selection method is designed to overcome increasing complexity of placing micron size sensor beads into their designated place in tiny micromachined sensor chip. The micromachined structures are added on each side of bead storing cavities to capture each designated sized beads. This is statistically feasible if bead lots are well sorted and the each size selection unit is designed to have a certain amount of differences. Glass bead size selection experiments were performed in dry conditions successfully. Finally agarose beads in wet conditions were marked in different fluorescent colors and installed into the size selection chip. While performing this agarose bead installation experiment, the loss of bead in the cavity happened repeatedly. The reason will be discussed in next chapter.

Chapter 5. Results and Discussions

5.1 Agarose beads as the chemical and biological sensor container

Agarose beads have been the classic medium for molecular chromatography. There are several kinds of chromatography methods; agarose is a good medium of gel permeation chromatography-which is called molecular sieve chromatography. Crosslinked agarose have very large pores in them, which allows smaller molecules to enter but excludes molecules larger than the pore diameters. Crosslinked dextrans and polyacrylamides are other examples materials that can be used for gel permeation chromatography.

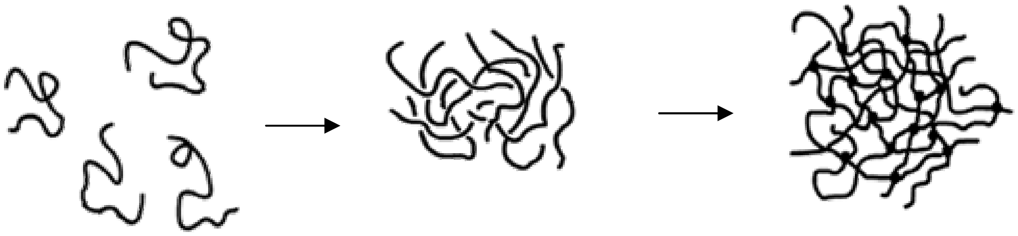

Figure 5.1.1 Cross linking polymer – GEL [22].

This permeation chromatography requires a bio specific ligand that is covalently bonded to a chromatographic bed material called a matrix. It is important that the bio specific ligands (antibody, enzyme, or receptor protein) retain their specific binding affinities for the substances of interest. The Sepharose is the commercial name of a bead-form of agarose gel which displays virtually all of the features required of a successful matrix for immobilizing biologically active molecules. The hydroxyl groups on the sugar residues can be easily derivatized for covalent attachment of a ligand. The 4% agarose bead is the most favored and widely-used matrix. The open-pore structure 4% agarose bead is very large and makes the interior of the matrix available for ligand attachment and ensures good binding capacities, even for large molecules.

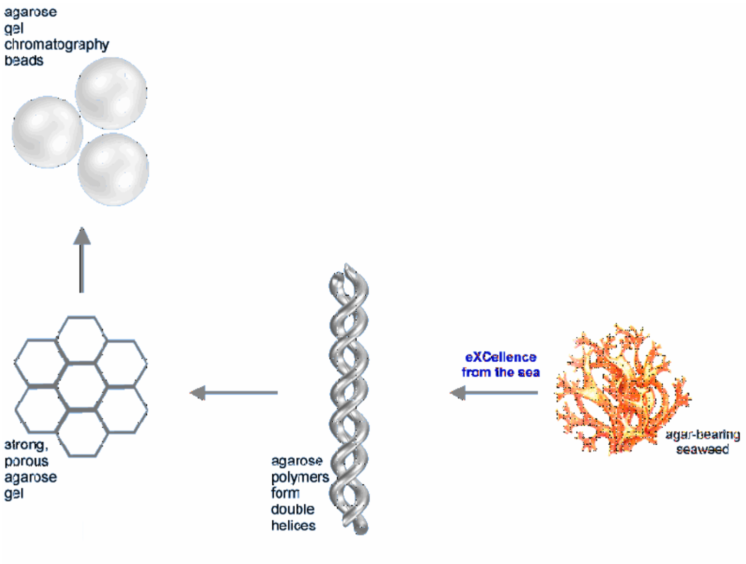

Figure 5.1.2 Agarose bead [22].

The 4% agarose bead shows very low non-specific adsorption, which is essential because the power of affinity chromatography relies on specific interactions. The bead-form of the gel provides excellent flow properties with minimal channeling in the bed which ensures that rapid separations are obtained. Adsorbents based on agarose are stable under a wide range of experimental conditions such as high and low pH, detergents and dissociating agents[22].

5.2 Nature of polymer bead swelling and dry shrinkage

Agarose beads start shrinking as soon as they leave a wet environment, and once dry, swell when placed back into a wet environment. The nature of gel bead swelling mechanism was well analyzed by Tanaka and Fillmore in 1979 [23]. A simple visualization of the swelling of polymer gel beads in shown figure 5.2.1. A crumpled polymer gel bead whose inner network is under uniform stress absorbs water when placed in the fluid and expands until the osmotic pressure of the gel becomes equal to zero and reaches equilibrium with the surrounding fluid.

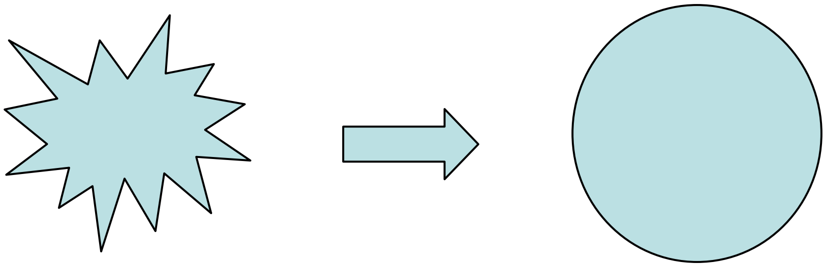

Figure 5.2 Illustration of agarose bead swelling.

It is indispensable to consider the size change of sensor containing beads while performing the bead placing step. Since force used in bead placing in the size sorting chip is air flow, beads may dry. As agarose beads are exposed to a dry environment instead of a wet environment where they should be kept, they start losing water stored inside. The average time of putting three kinds of different size bead into size selection chip is around 120 seconds in author’s experiments, so changes in bead diameter during this time should be considered.

Chemists have treated these agarose beads with sensor as much as possible so as not to be away from wet environments. Normally the only step agarose beads are away from wet environments are when beads are being placed into the chips. A general idea is that antibodies lose their activities as they dry, but as they are reconstructed with a buffer, they become active again. This comes from the three dimensional shape functional characteristics of the protein. As they dry, three dimensional structure of proteins change. This brings about less activity of the protein but this activity recovers as they are reconstituted with buffers. In the view of this result, dry agarose beads with sensors could be placed into the chip with size selection method and then be reconstituted.

5.3 Study of agarose bead size changes

As shown in figure 5.3.1, agarose beads shrink as they come out of water and are kept in a dry environment. The beads in a normal atmosphere show a random starting time for shrinkage; this uncertainty of the start time of shrinking probably comes from the uncertainty of water content in the micromachined storage well containing the agarose beads. Beads in an air flow condition show immediate shrinkage because a vacuum has been used to remove all the excess liquid water from the storage well containing the beads. If light illuminates the agarose beads (such as the case when a microscope is used to record the image of the beads), it also affects drying. From experimental data, however, illumination does not affect drying nearly as much as air flow.

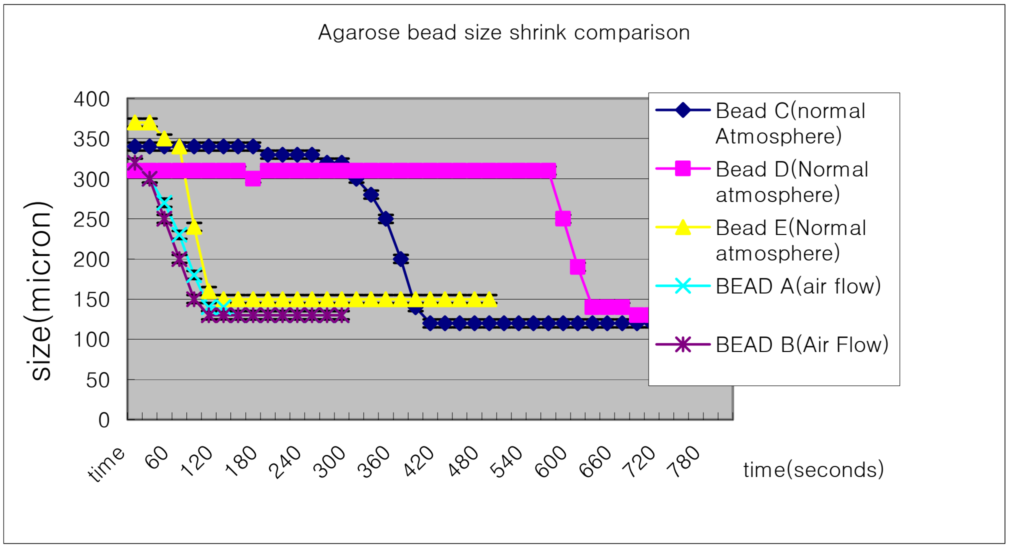

Figure 5.3.1 Agarose bead size shrink chart.

However, as the beads start shrinking, the time rate of change in diameter is fairly similar for the different cases. While the author monitored the pictures of shrinking agarose beads in every case, a number of common characteristics of agarose bead shrinkage were observed. When beads are fully wet, even if the beads are exposed to dry atmosphere, they have “halos” around them as shown in figure 5.3.2 and figure 5.3.3. As they dry, these wet halos disappeared as can be seen clearly in figure 5.3.4. Then beads start shrinking as shown in figure 5.3.5. Figure 5.3.6 shows the ratio of each bead size over its maximum size. All the beads under same condition shows similar slope of bead size shrinkage. The rate of drying is so fast that even in 60 seconds agarose beads shrink to 70% of their wet size, which makes size selection method very difficult. In 100 seconds under dry air flow environment, agarose bead shrink to less than 50% of their original wet diameter. In the most recent size selection chip design, each bead size selection unit has around 30 micron differences to discriminate. In the case of 330 micron beads, it takes only 40 seconds to shrink 30 microns. If this were to occur the beads captured in the storage wells during size sorting could actually escape out of the bottom of the chip.

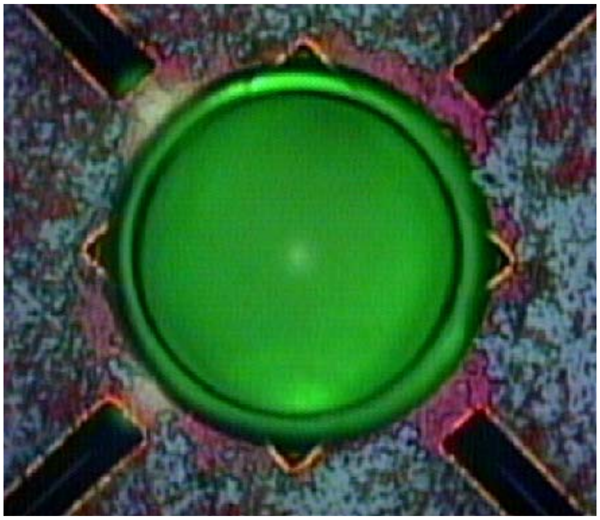

Figure 5.3.2 Initial stage of beads in normal atmosphere.

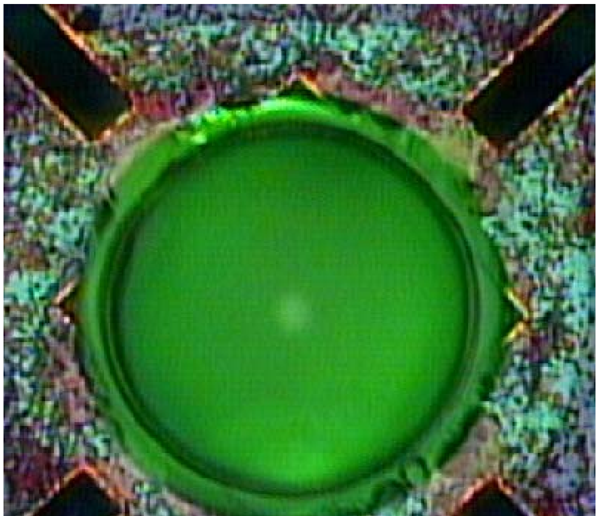

Figure 5.3.3 Right before starting shrink, after 220 seconds in normal atmosphere.

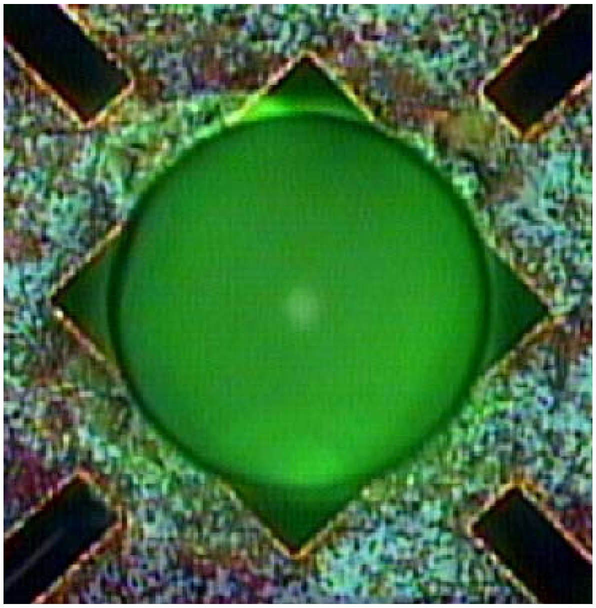

Figure 5.3.4 Bead start shrinking, after 240 seconds in normal atmosphere.

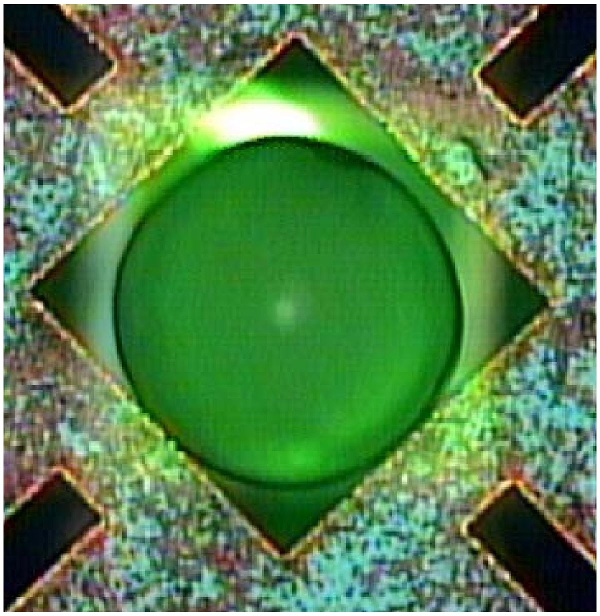

Figure 5.3.5 Bead is shrinking, after 300 seconds in normal atmosphere.

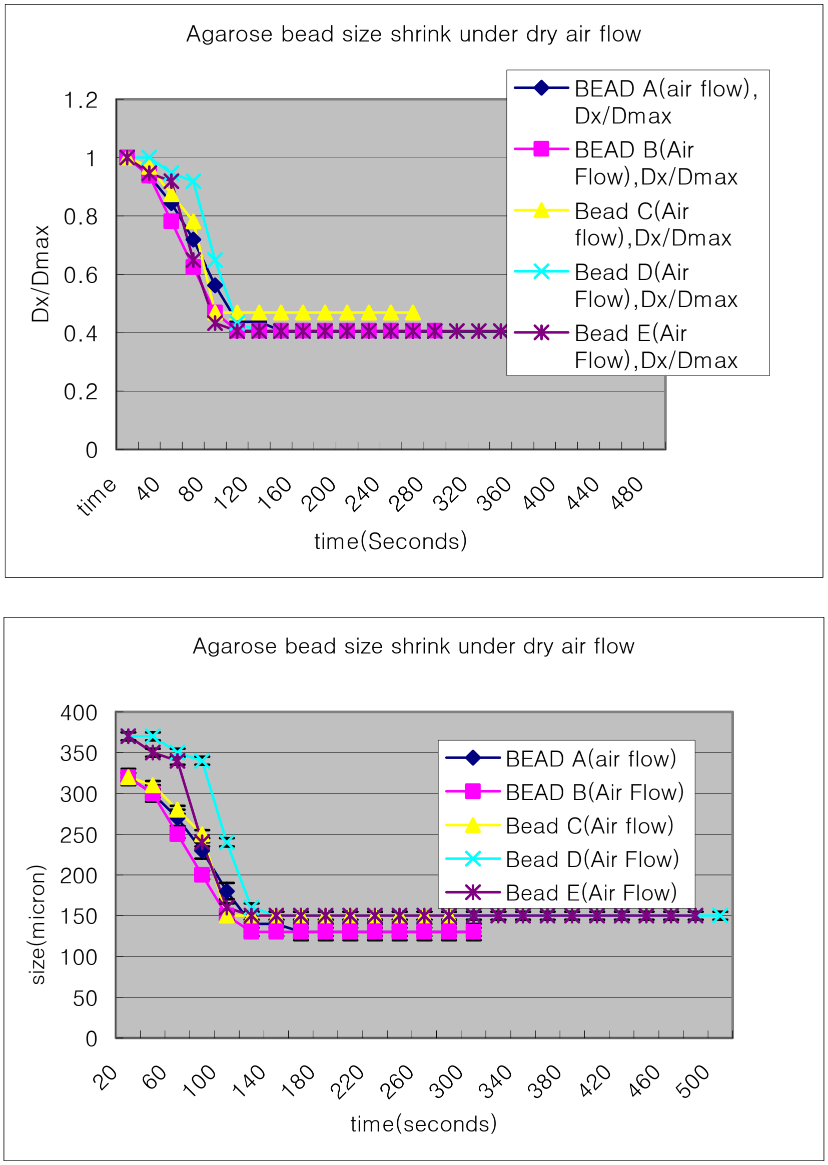

Figure 5.3.6 Agarose beads size shrinkage chart under dry air flowing environment.

Since the agarose beads are the main container of chemical and biological sensors, this problem must be overcome. One possibility is to pre-dry the beads before size sorting into the chips; this option would only be possible if the agarose beads recover their original characteristics after re-wetting. To understand the re-wetting behavior of an agarose bead, the author used dried agarose beads in a size selection chip to test the expansion as water is introduced. The chip was stored in a normal dry environment and water was applied by a syringe.

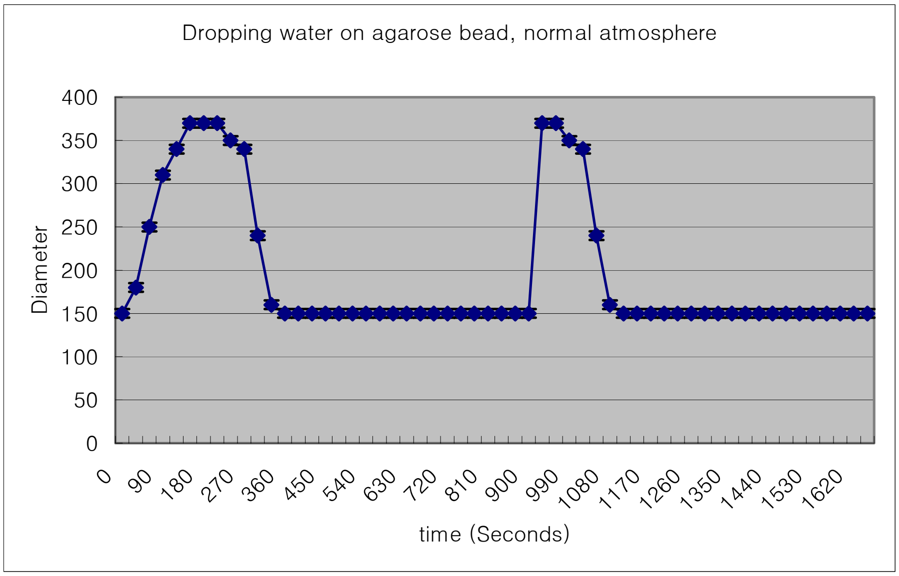

Figure 5.3.7 Agarose bead size change as getting wet and dry.

The author planned a simple experiment of observing the size changes after dropping a drop of water into the dehydrated agarose bead in the size selection unit. As shown in figure 5.3.7, as soon as water drops onto the well, the bead starts expanding. The slope of size expansion is not very different from that of size shrinking. Figure 5.3.8 and 5.3.9 are pictures taken after dropping the water. In less than 120 seconds, a dry bead expands again back to its original wet size. Even after drying out again, it will expand back to its original size as shown in figure 5.3.1. This size recovery suggests it might be possible to pre-dry beads before using the size-selective chip, and perform the assembly in dry air (as was originally demonstrated using glass beads), although the storage wells will then have to accommodate the large increase in bead diameter when they are re-exposed to a wet environment. There is also concern that the reconstituted beads might lose at least some of their chemical sensitivity for an agarose bead that has been dried and then re-wet.

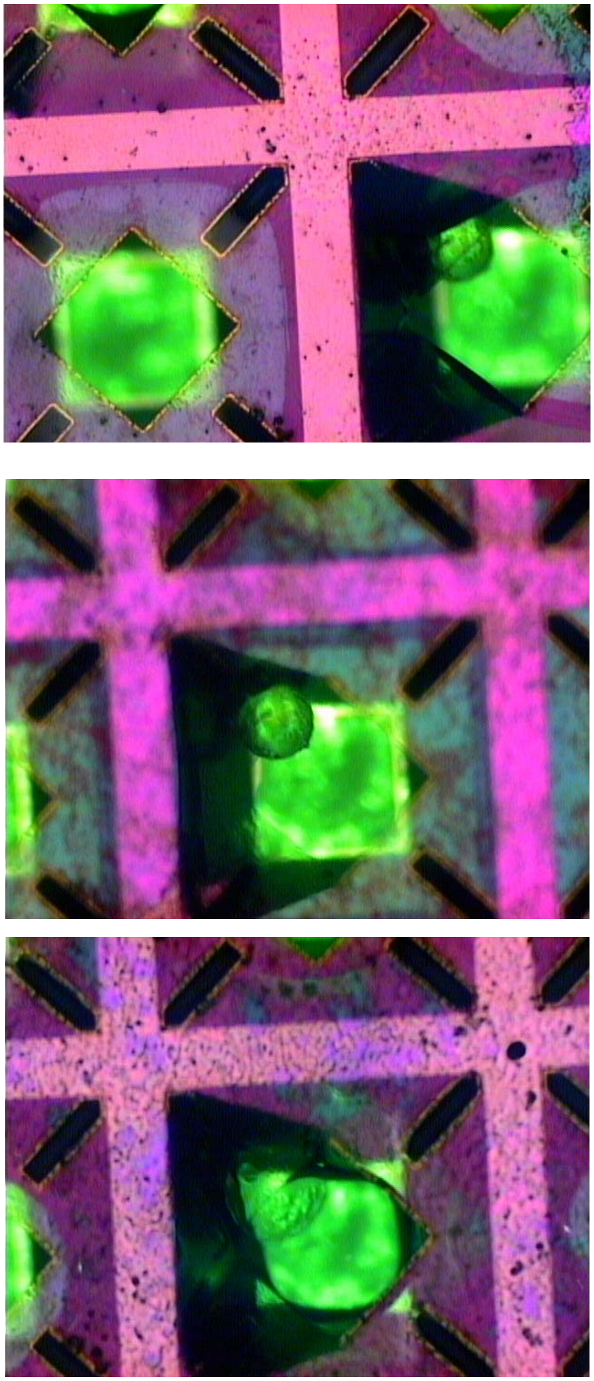

Figure 5.3.8 Agarose bead expands as water drops onto, 30 seconds intervals.

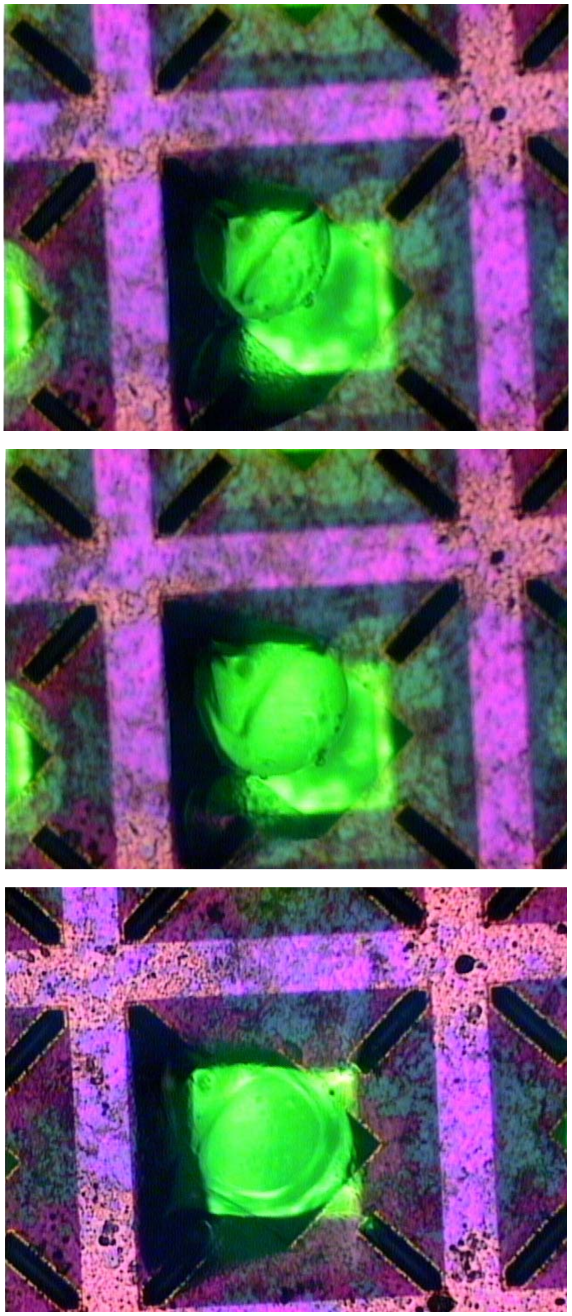

Figure 5.3.9 Agarose bead expands as water drops onto, 30 seconds intervals.

Another approach, rather than allowing the beads to dry at all, would be to keep the agarose bead container with the sensor in a wet environment all the time. That solution should keep beads from drying as well as shrinking to prevent losing beads from the chip. If very humid air could work the same as a drop of water, shrinkage by dehydration would not occur. Figure 5.3.10 is a comparison chart of bead size change with water and for beads with humidified air blown around them, indicating that this approach might work.

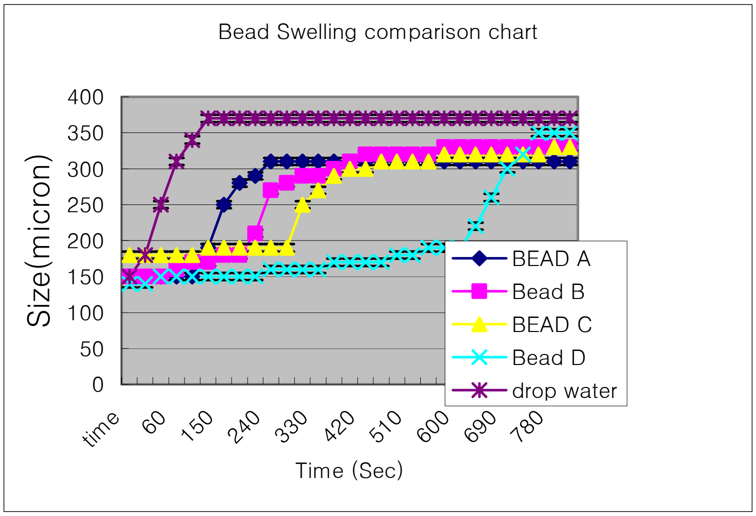

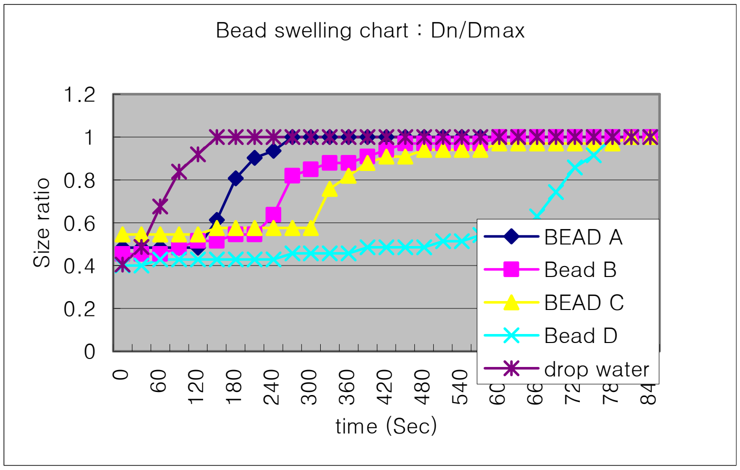

Figure 5.3.10 Bead swelling by water and 100% humidified air.

Humidity can be expressed in several ways; including absolute, specific and mixing ratio humidity. In general, the humidity measures the mass of water vapor for a given mass of dry air. It may be measured in grams of water vapor per kilogram of dry air. Mixing ratio humidity is a commonly used measure by meteorologists. At a temperature of 20 degrees C, at average sea level pressure, the saturation mixing ratio is 14 grams of water per kilogram of dry air. In the case of humidifier used in the author's bead experiments, the air flowed over the beads is saturated humid air, which can be described as 100% humidified air.

As seen from the chart in figure 5.3.10, 100% humidified air environment can also swell dry beads back to their full wet size, although the time to reach full size is different for "wet air" and liquid water. Data in figure 5.3.10 was taken with beads simply placed on a surface. Data in figure 5.3.11 was taken with the size selection chip on top of vacuum chuck, the same condition when agarose bead size selection is performed. This chart shows even under strong air flow through the bead and bead storage well, humidified air could perform the same role as liquid water. Figure 5.3.12 shows the size change of agarose beads as they were allowed to dry from a humidified air environment, and then reconstituted again using humidified air. As the humidifier was turned off, bead size decreases abruptly to its minimum size. As humidified air is supplied again, the beads again swell back to their original size.

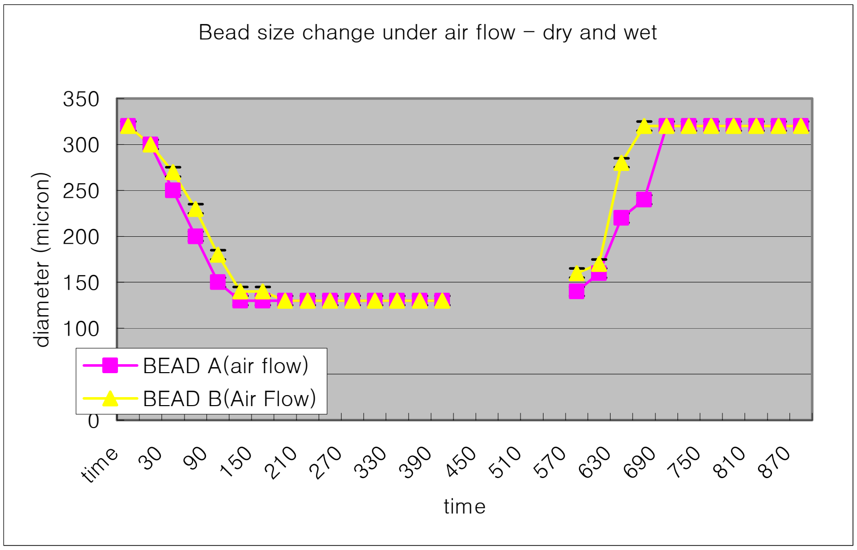

Figure 5.3.11 Agarose beads size change chart, under air flow by humidifier.

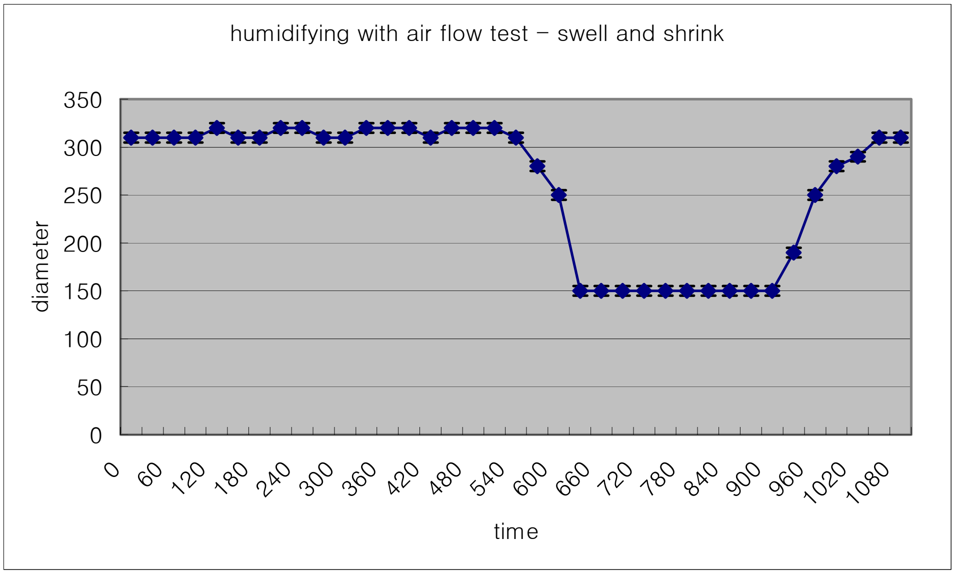

Figure 5.3.12 Agarose bead swelling and drying experiment, on vacuum chuck with humidifier.

Figures 5.3.13 through 5.3.16 are the pictures taken from the same experiment charted in figure 5.3.12. Humidified air created wet halos around beads as well as "dew" on top of the chip. These pictures are the same agarose bead taken after 120 seconds, 240 seconds and 360 seconds. As the humidifier is turned off, rapid shrinkage occurs, which is the evidence of strong air flow. Agarose bead shrank in two minutes to its smallest size in this experiment.

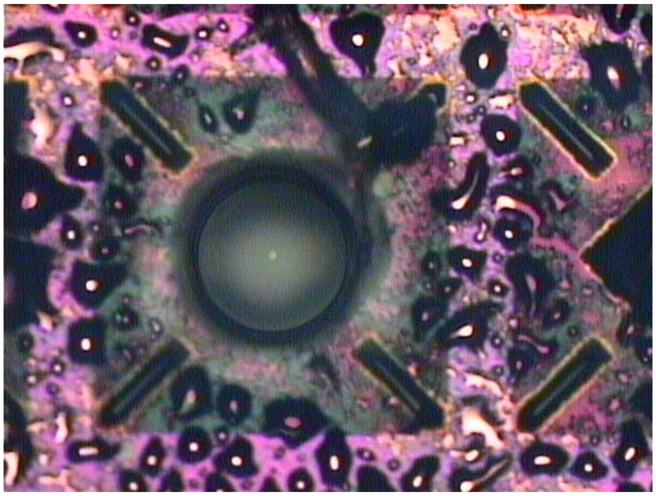

Figure 5.3.13 Agarose bead on the chip with vacuum chuck turned, in humidified air, t=0 seconds.

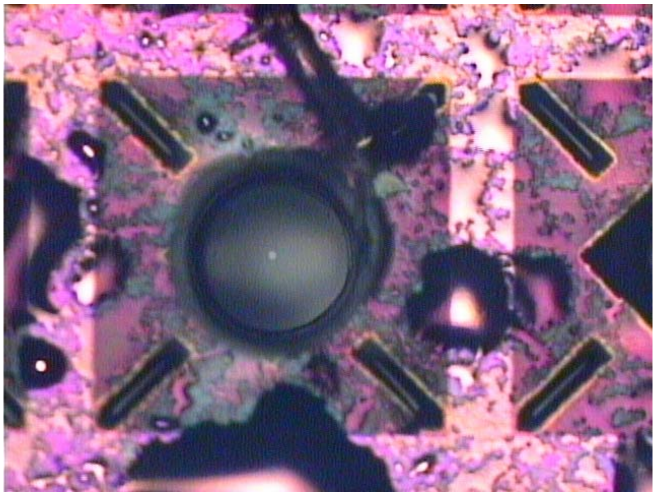

Figure 5.3.14 Agarose bead on the chip with vacuum chuck turned, in humidified air, t=120 seconds.

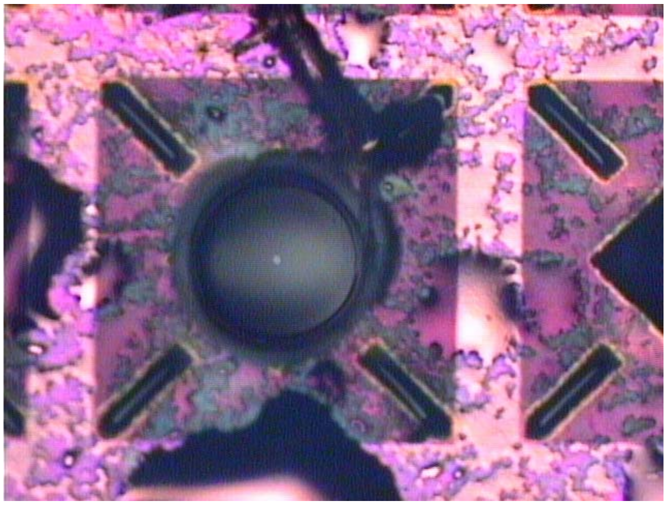

Figure 5.3.15 Agarose bead on the chip with vacuum chuck turned, in humidified air, t=240 seconds.

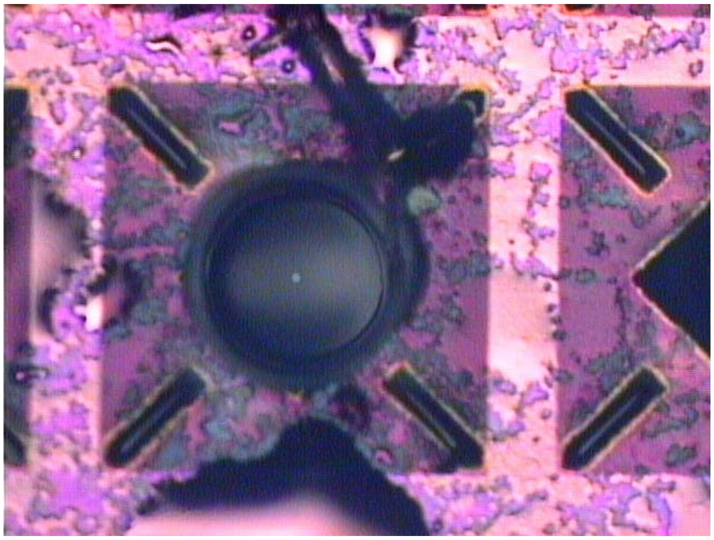

Figure 5.3.16 Agarose bead on the chip with vacuum chuck turned, in humidified air, t=480 seconds.

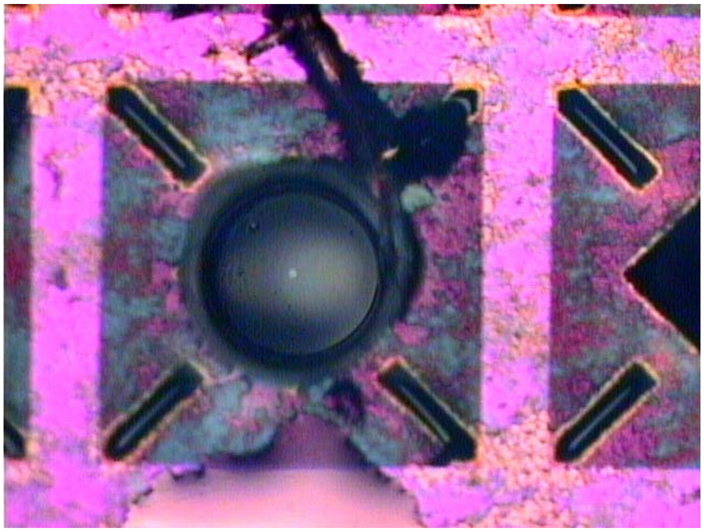

Figure 5.3.17 Agarose bead on the chip with vacuum chuck turned, t=510 seconds.

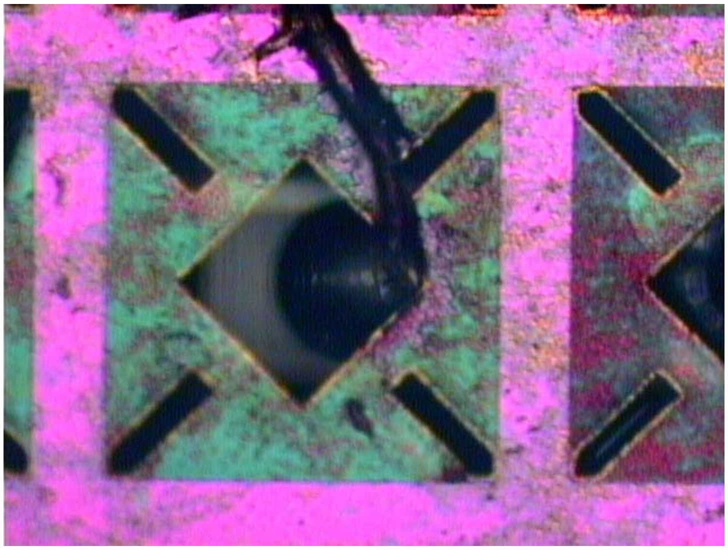

Figure 5.3.18 Agarose bead on the chip with vacuum chuck turned, t=630 seconds.

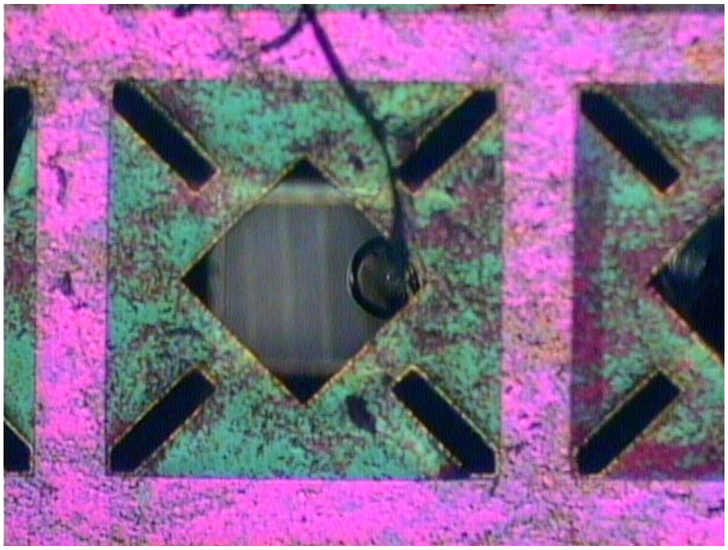

Figure 5.3.19 Agarose bead on the chip with vacuum chuck turned, t=690 seconds.

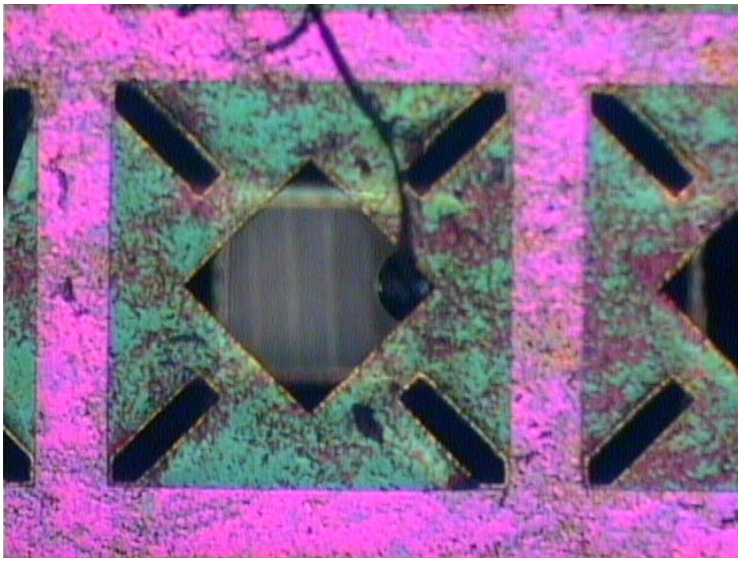

Figure 5.3.20 Agarose bead on the chip with vacuum chuck turned, t=750 seconds.

Since agarose beads can be easily reconstructed with humidified air to their wet condition, keeping their original size, it should be found how long they can stay in that status. Normally, it takes around 30 seconds to perform each bead installation onto the chip, so a maximum time of 480 seconds would be enough for filling current 8 different size sorting units in a chip. It would be reasonable to consider that if agarose beads do not shrink under the humidified environment for 10 minutes, they can be regarded as good size sorting objects like glass beads, which don't shrink. Pictures in figure 5.3.23 through 5.3.26 show long term observations under humidified environment. It can be noticed that even after 400 seconds in humidified environment, the bead does not lose its wet halos around itself. With this result, the author can conclude that agarose beads can keep water saturated sizes while size selection procedure is undertaken.

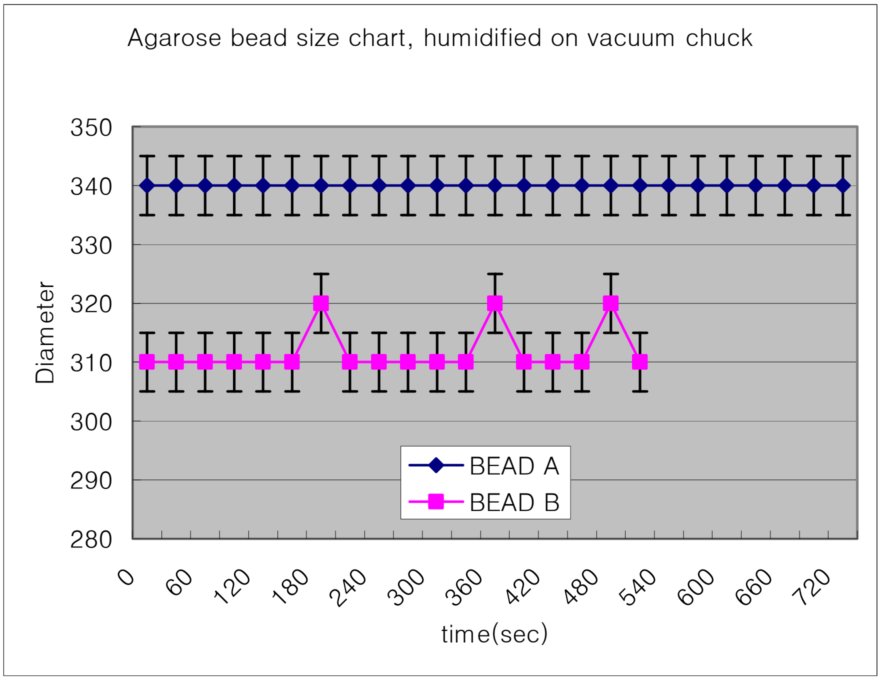

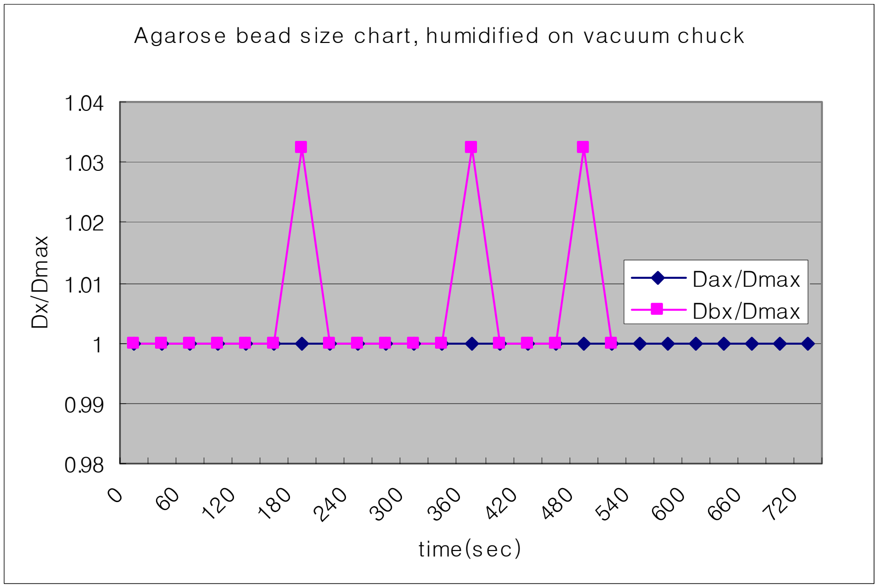

Figure 5.3.21 Size of the agarose bead on vacuum chuck under humidified environment.

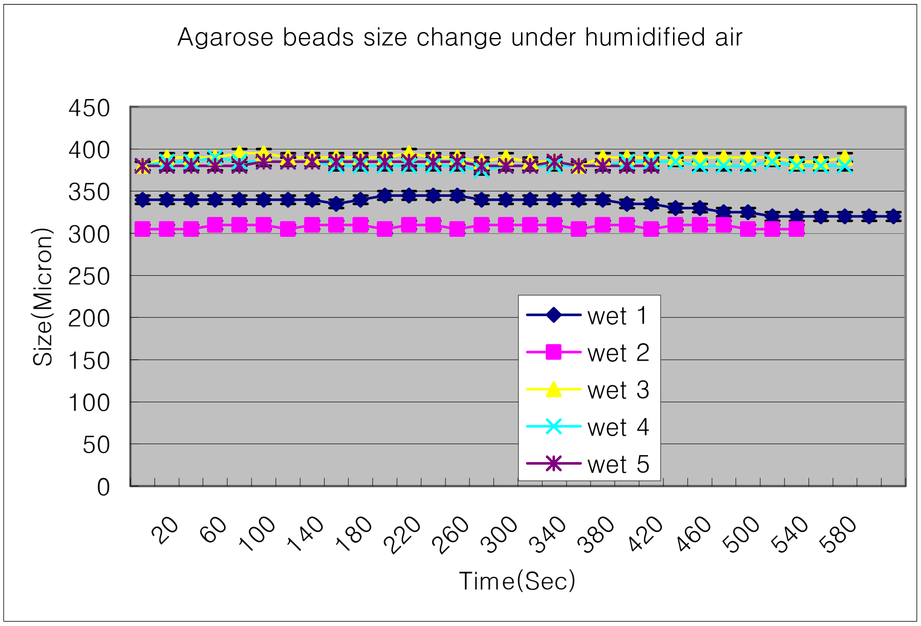

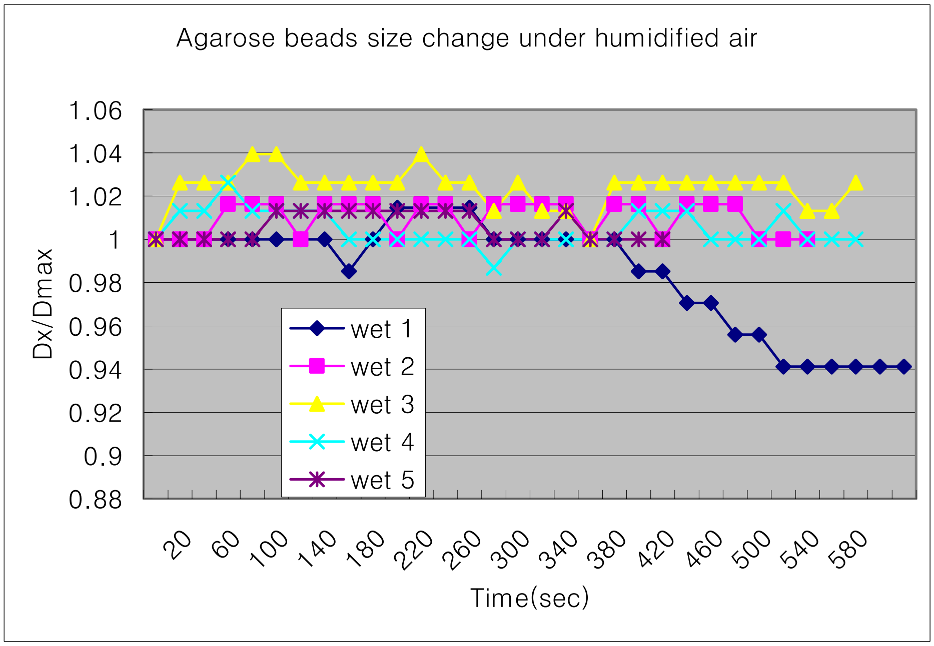

Figure 5.3.22 Size of the agarose bead under humidified environment.

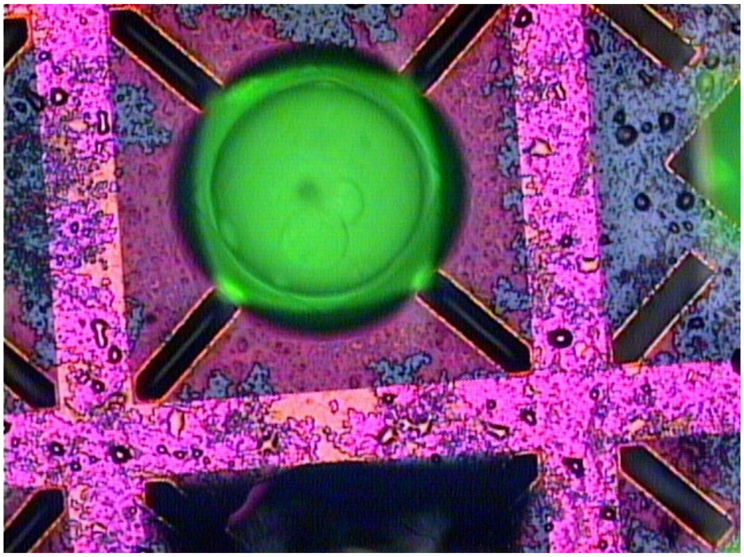

Figure 5.3.23 Agarose bead in humidified environment, t=0 second.

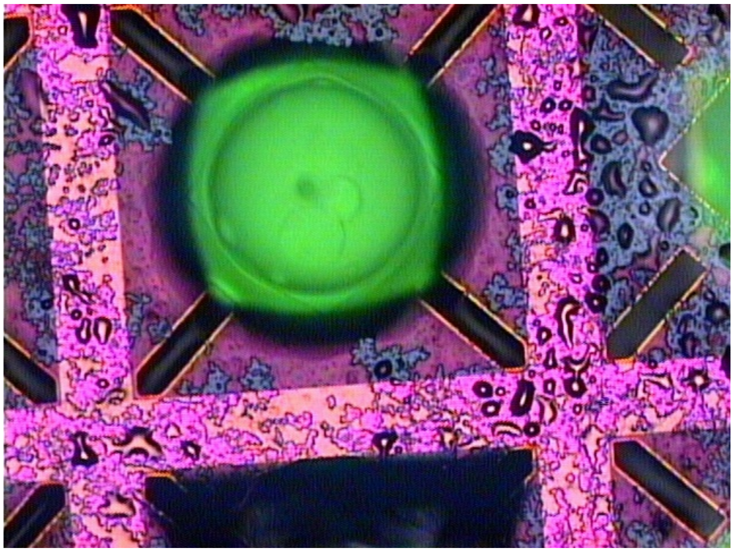

Figure 5.3.24 Agarose bead in humidified environment, t=200 seconds.

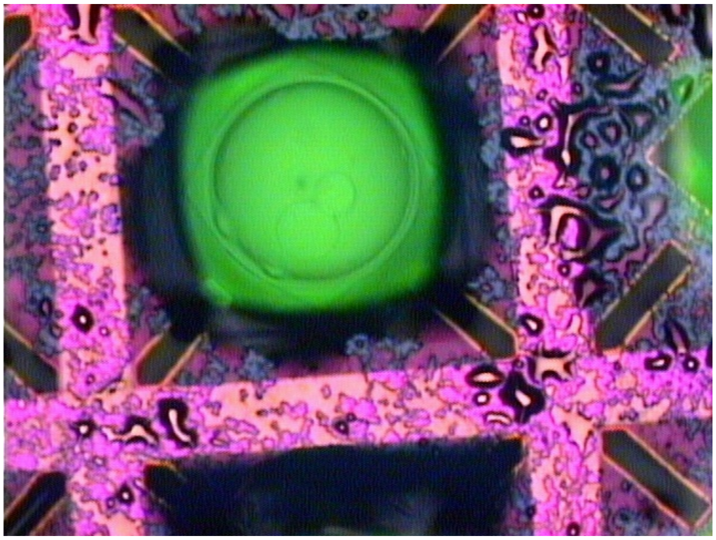

Figure 5.3.25 Agarose bead in humidified environment, t=400 seconds.

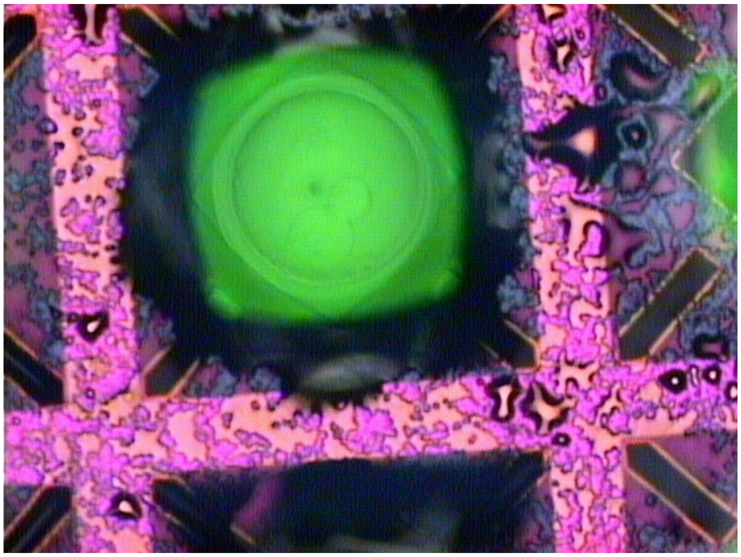

Figure 5.3.26 Agarose bead in humidified environment, t=600 seconds.

5.4 The effect of environmental humidity changes to sensor activities

The size of agarose beads can be maintained under a saturated humid environment as evidenced in a consistent fashion by multiple experiments. The structural feasibility of size selection method has been described in a previous section. The applicability of size selection method can be verified under the bio/chemical stability of sensors under standard conditions. If the sensors maintain activity under saturated humid air environment, not only bead loading process but also assaying preparation and preservation of fully loaded sensor chip can be much more flexible. Here, we utilized a bead-based assay previously developed by the McDevitt group for the detection and measurement of CRP to evaluate the effects of humidity on this bead type of sensor.

C-reactive protein (CRP) is a protein made by the liver and secreted into the bloodstream. The concentration of CRP increases within a few hours after the start of an infection, which makes it especially valuable for monitoring infections. The concentration of CRP rise in the blood often precedes pain, fever, or other clinical indicators. The level of CRP can jump a thousand-fold in response to inflammation. It drops relatively quickly as soon as the inflammation passes, making it a valuable test to monitor effectiveness of treatment. The CRP test is used in patients with inflammatory bowel disease and some forms of arthritis and autoimmune diseases to assess how active the inflammation is and to monitor the treatment. The CRP test is also used to monitor patients after surgery or other invasive procedures to detect the presence of an infection during the recovery period. CRP test is not specific enough to diagnose a particular disease but a general marker of infection and inflammation that alerts medical professionals that further testing and treatment may be necessary. More recently, chronic low-level inflammation has been defined as the underlying contributor for the development of arteriosclerosis, the underlying cause of cardiovascular disease. Likewise, CRP has been described as a strong independent risk factor for heart disease. More specifically, apparently healthy individuals with chronic low-level elevations of CRP are at higher risk for CVD than those with low CRP in their serum. [24, 25]

Figure 5.4.1a illustrates the first step of the experiment, in which CRP-specific capturing antibody is conjugated on the porous agarose beads (300μm diameter). The agarose beads are then positioned into micromachined wells on a silicon chip and exposed to a phosphate buffered saline (PBS) wash before flowing sample containing CRP antigen and CRP-detecting fluorescently-labeled antibody.

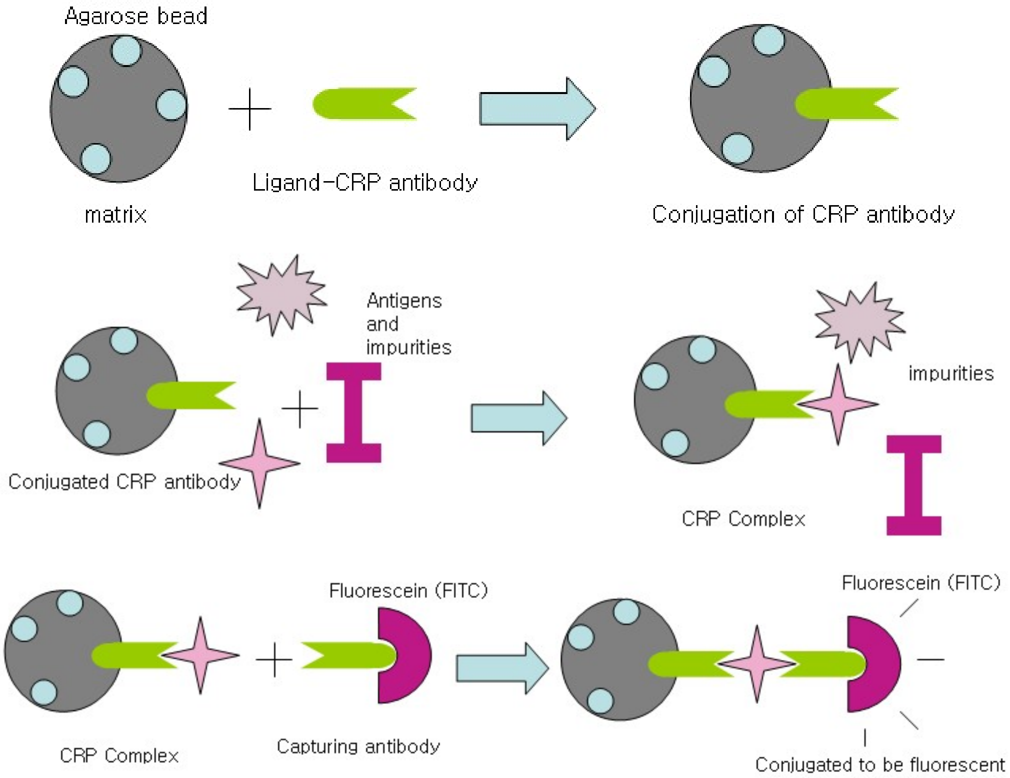

Figure 5.4.1 Illustrations of chemical sensing reaction measurement step.

a. Conjugation of CRP antibody on agarose beads.

b. Capturing of CRP antigen on beads.

c. Fluorescent detection of captured CRP on bead with a FITC-conjugated CRP-specific antibody.

CRP antigen is combined with CRP antibody on the bead as shown in figure 5.4.1b after a five minute incubation. After a brief PBS wash, fluorescently (FITC)-labeled antibody specific for CRP dye is introduced into the chip to detect the captured CRP analyte on the bead (figure 5.4.1c). The concentration of CRP assayed is proportional to the brightness of the fluorescent signal on each bead.

In this CRP assay, two negative control conditions are also used. The first involves beads coated to an antibody irrelevant to CRP. These beads should not recognize CRP and are thus not expected to bind to it. Consequently, these beads should produce no signal after incubation with CRP and CRP-specific detecting antibody. The second control condition involves an assay run in which no CRP antigen is presented to the bead. Once again, no signal is expected on these beads, as no antigen is available to bind to the CRP-sensitized beads. In contrast, when beads coated with a CRP-specific capturing antibody are exposed to CRP, a positive signal is produced that is proportional to the CRP concentration; this condition serves as a positive control [24].

The types of beads tested were:

- **Internal "large pore" beads produced in the McDevitt Lab**
    - ❖ Conjugated to a CRP-capturing Antibody
    - ❖ Conjugated to a CRP-irrelevant Antibody
- **Commercially-available beads from ABL**
    - ❖ Conjugated to a CRP-capturing Antibody
    - ❖ Conjugated to a CRP-irrelevant Antibody

Sensor activity was tested after exposure of the beads to four different environmental conditions that can happen while bead size sorting is undertaken: normal control, always wet, (1); normal conjugation and loading into a standard chip, followed by drying, exposure to the rest of the assay (2); normal conjugation and loading into a standard chip, followed by drying, then reconstitution of the beads using humidified air, then exposure to the rest of the assay (3); and normal conjugation and loading into a standard chip, followed by continuous exposure to humidified air, then exposure to the rest of the assay (4). Figure 5.4.2 illustrates these various exposure conditions. Sample (2) and (3) were exposed to nitrogen air for two minutes for drying after finishing bead installation into the sensor chip. Sample (4) is exposed to saturated humid air for twenty minutes and sent to assay.

In each experiment, positive antigen assay was comprised of 6 positive CPR conjugated sensors with home-made agarose beads and 6 positive CPR sensors with commercially acquired 6% agarose beads. The author will refer to the home-made agarose bead as type A, and the commercially acquired beads as type B. Negative controls and non specific assay samples were prepared the same as positive assay test.

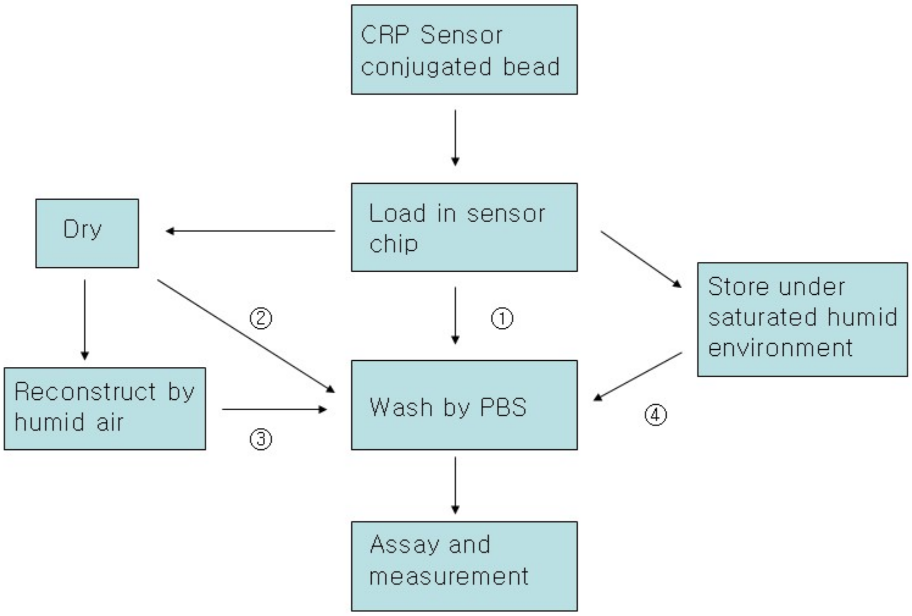

Figure 5.4.2 Immunoassay steps and variations for experiments.

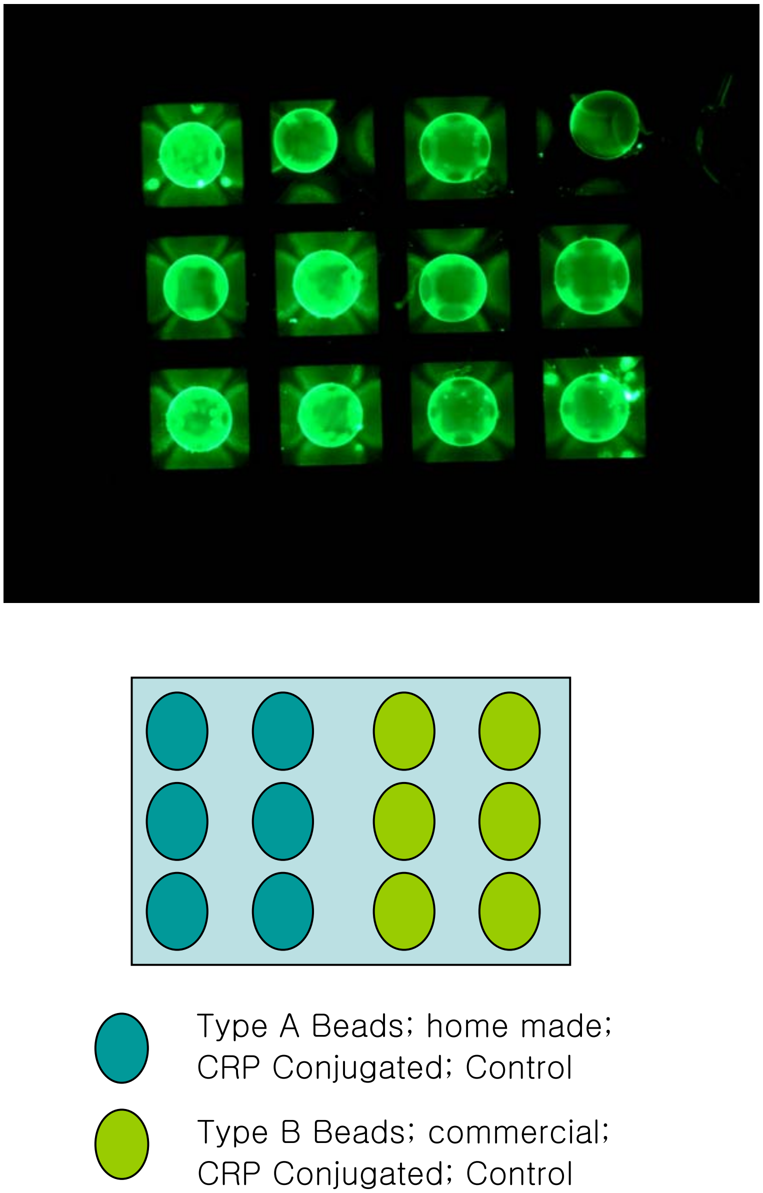

Figure 5.4.3 Normal condition assay result – the control(1).

All twelve beads show bright fluorescent results in figure 5.4.3 for the normal control sample (1). Two columns in left sides are type A agarose beads and the other two columns in the right sides are type B agarose beads as described before. These arrangements are kept the same in all the experiments. The intensity of signal is the brightness of fluorescent green light. This control will act as a ruler to measure the activity of the sensor after a environmental change. As beads were exposed to air flow for two minutes, they shrank as described in previous sections. Figure 5.4.4 is the assay result of dried bead sample. It is noticeable that the brightness of each bead is within measurement error equivalent to that of the control. This suggests that there was successful three dimensional reconstruction of enzyme during the PBS (phosphate buffered saline) wash step. While the type B agarose beads are fully reconstructed to their original size, type A agarose beads are not reconstructed to their original size. The reason of this unexpected behavior of type A agarose bead is suspected to be collapse of the large pores in this home-made bead. Nonetheless, the type A beads were still an effective sensor fro HRP.

The assay result of experiment (3) is shown in figure 5.4.5. Sensor beads are dried by air flow for two minutes and reconstructed under saturated humid air for four minutes. The assay result shows that the enzyme sensors reconstructed successfully again but type A agarose beads behave same as experiment (1). This result drives the assumption that the reconstruction of type A agarose bead is difficult once they totally shrunk.

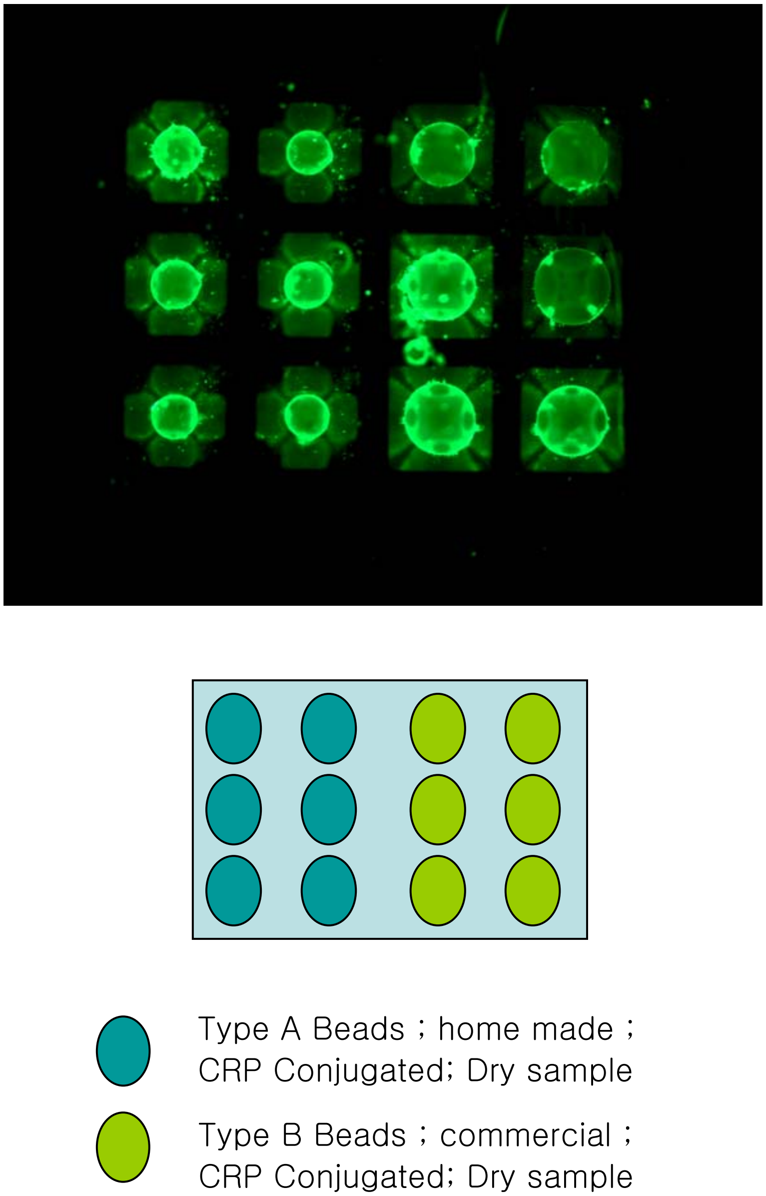

Figure 5.4.4 Assay result of dried sample (2).

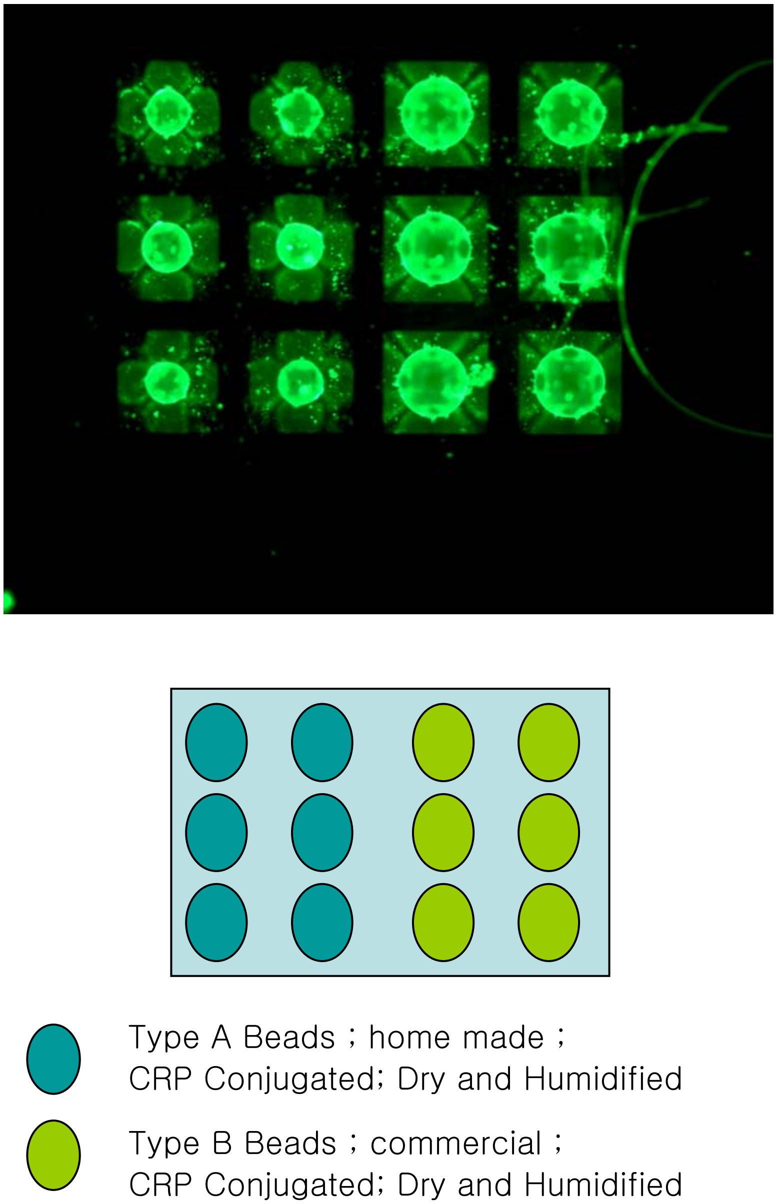

Figure 5.4.5 Assay result of dried – reconstructed by saturated humid air sample (3).

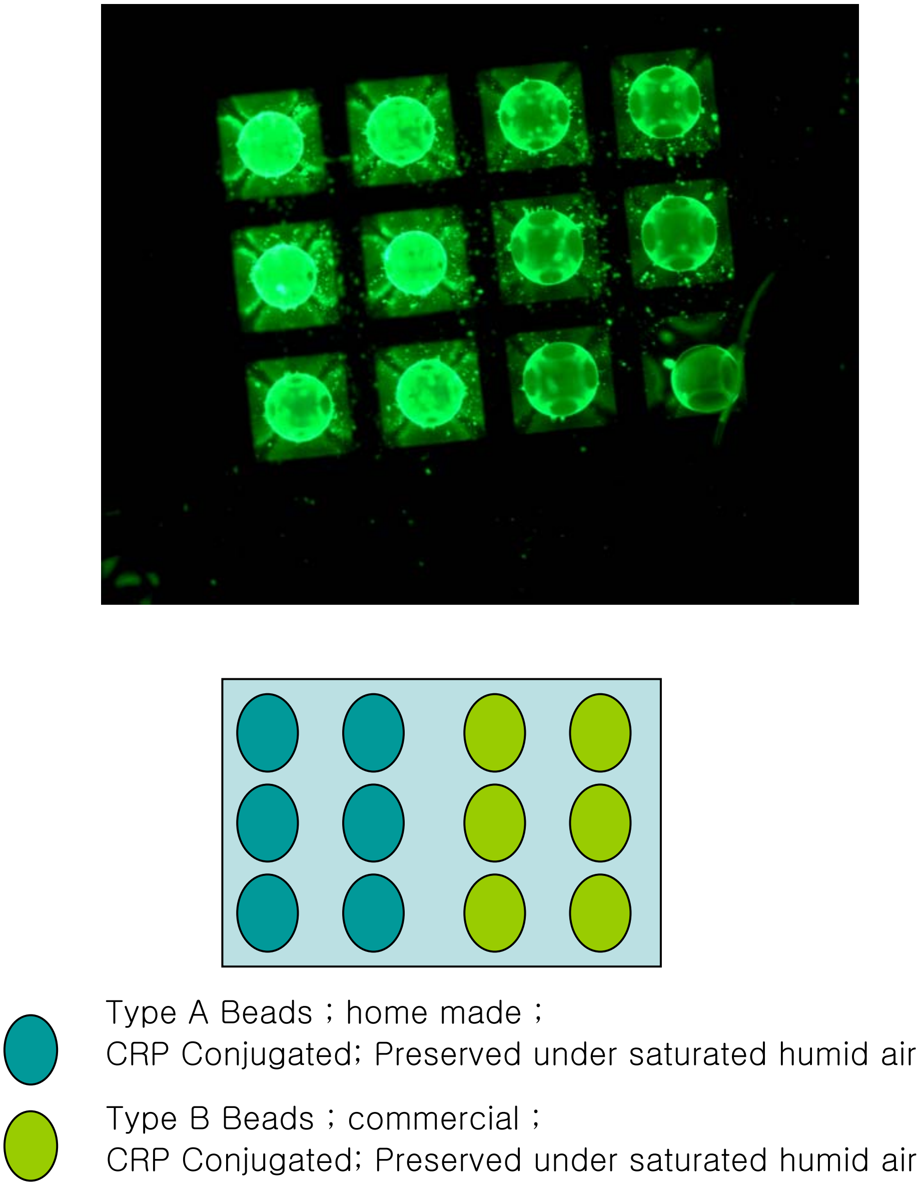

Figure 5.4.6 Assay result of chip stored under saturated humid air environment (4).

In the experiment (4), the sensor chip was exposed to saturated humid air for twenty minutes to keep sensor beads from drying. The sensor chip was separated from the humidifier outlet by about 6 inches, far enough not to condense liquid water on the chip. Under a saturated humid air environment, all the sensor beads in the chip did not shrink. In that wet environment, even larger pore sensor bead type A maintained their sizes. The result of assay sequence (4) is shown in figure 5.4.6. The strength of signals as well as the sizes of beads is almost same as assay sequence (1). In contrast, for sequences (2) and (3), the type A agarose beads did not fully recover their original size. The saturated humid environment does successfully preserve the activity and signal strength of enzyme sensors as well as the structure of agarose beads.

The negative control, beads conjugated with non-specific antibody of CRP and non-specific antigen reaction, results also support this conclusion. As illustrated in figure 5.4.7 and 5.4.8, the negligible signals in those non-specific antigen-antibody reactions show that the saturated humid air does not affect the negative reactions as well.

According to the experimental data acquired by CRP experiments, the author concludes that the addition of saturated humid air in the processes of assembly conjugated enzyme sensors into chips does not harm either the bio/chemical or structural characteristics of agarose sensor beads

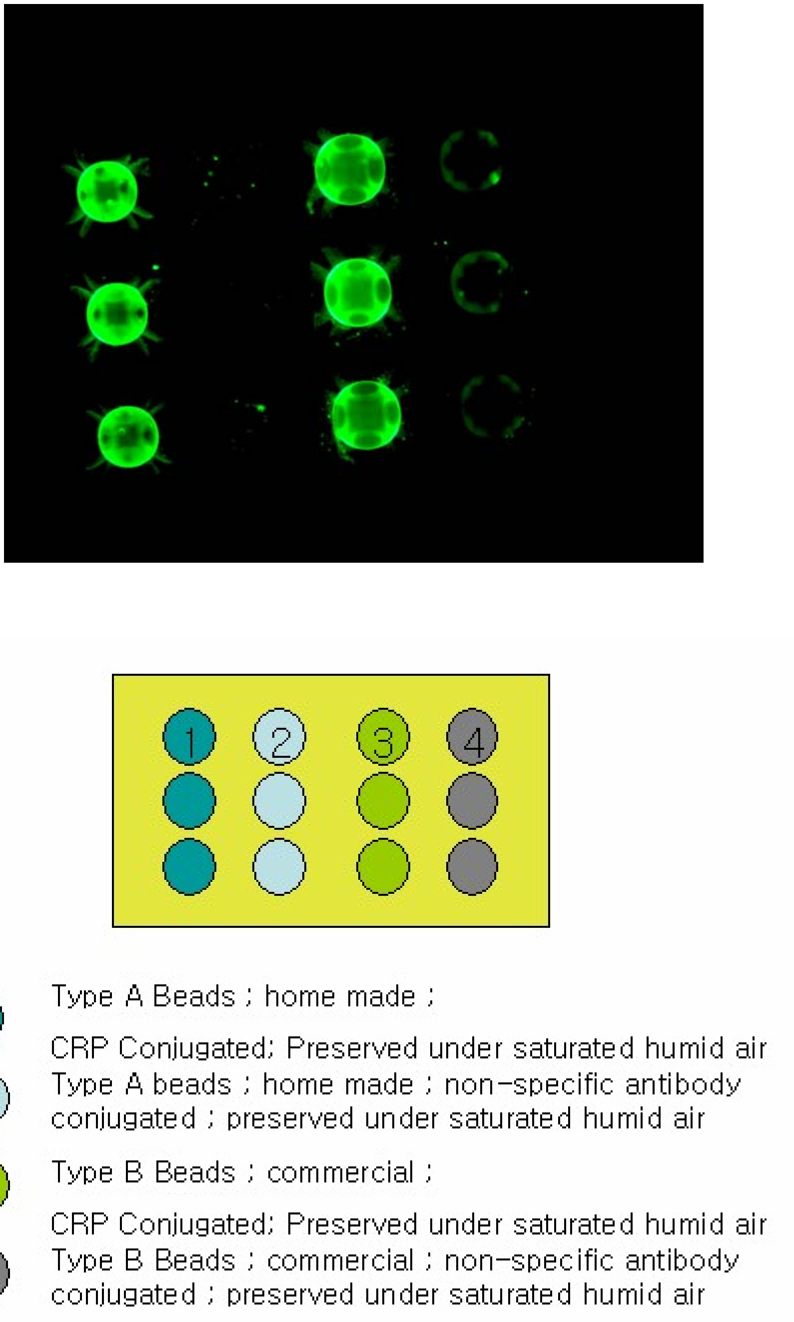

① Type A Beads ; home made ;
CRP Conjugated; Preserved under saturated humid air

② Type A beads ; home made ; non-specific antibody
conjugated ; preserved under saturated humid air

③ Type B Beads ; commercial ;
CRP Conjugated; Preserved under saturated humid air

④ Type B Beads ; commercial ; non-specific antibody
conjugated ; preserved under saturated humid air

Figure 5.4.7 Non specific antibody assay result
under saturated humid air environment (4).

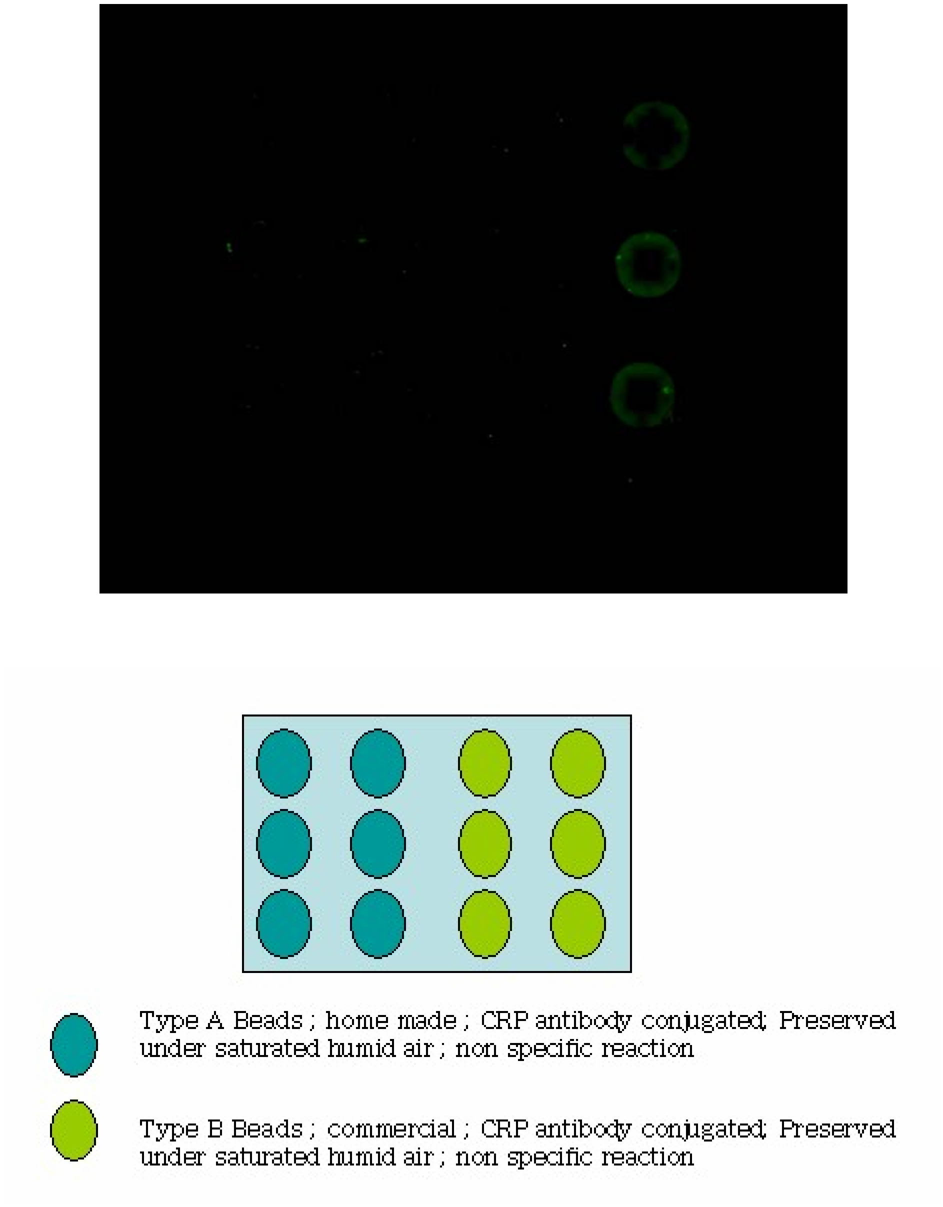

Figure 5.4.8 non-specific antigen assay under saturated humid air environment (4).

5.5 Summary

Crosslinked agarose beads can have very large pores in them, which allow smaller molecules to enter but exclude molecules larger than the pore diameters. The bio specific ligands (antibody, enzyme, or receptor protein) bind to the hydroxyl groups in the crosslinked agarose covalently. Collapsed agarose gel beads absorb water in the fluid and expand until the osmotic pressure of the gel becomes equal to zero and reaches equilibrium with the surrounding fluid. As it loses water from inside by dehydration, it shrinks to a certain minimum size, while it expands again as it absorbs water from outer environment. A saturated humid environment produced by a humidifier can prevent this drying. Under saturated humid environment, an agarose sensor bead maintains its physical shape as well as chemical sensor activity. Hence size selection chips can be used to assemble such chemical sensor arrays by making use of a saturated humid environment.

Chapter 6 Conclusion

A size selection method for chemical sensor array chip bead placement has been invented. A novel electronic taste chip has been designed and fabricated to test the feasibility of the size selection method.

The chip was made in a silicon substrate using a silicon rich nitride and silicon oxide composite film. Silicon substrate is double side polished so as to allow the fabrication of structures on both sides of the wafer. The composite film works as a bulk etch mask as well as the structure that size-sorts various kinds of beads. The anisotropic wet etching of silicon creates a pyramidal cavity in silicon substrate, in which sensor beads are stored. The size selection chip uses two different size sorters covering the top and the bottom of the pyramidal cavity to capture only an appropriately sized bead in a designated storage well.

Each size selection unit is designed to select certain size $\mu_{x,}$ which is separated from the next size by $4\sigma_x+\sigma_{x+1}$, hence statistically there should be less than 0.01% errors for selecting wrong size beads, where the mean size of bead x is μ_x and variance is σ_x. In our actual experiments, the mean size and variances are not as clearly defined in our samples, so various size separations were tested. Before using a double sided lithographically patterned design the author fabricated a single side size selection chip, but this design has errors that trace to variance in wafer thickness, a variable that is traditionally expensive to tightly control in silicon wafer production. Using a double side aligner for photolithography a new size selection design was fabricated. To have a robust sifting structure on top and bottom, a silicon rich nitride film was substituted for the normal Si_3N_4 film. Silicon rich nitride composite films with the half thickness achieve better yield than Si_3N_4 composite films. This thinner and robust composite film enabled a simpler fabrication step with better yield. A stiffer film recipe was discovered recently by another group member and is expected to produce micromachined chips with even better yields.

Size selection method is suggested to overcome increasing complexity of placing micron size sensor beads into their designated place in tiny micromachined sensor chips. The micromachined structures are added on each side of bead storing cavities to capture each designated sized beads. This is statistically feasible if bead lots are well sorted and each size selection unit is designed to have a certain amount of differences. Glass bead size selection experiments were performed successfully, with beads delivered by both air flow and by water flow. Finally, agarose beads delivered in water, each marked with a different fluorescent color, were installed into the size selection chip. While performing this agarose bead installation experiment, changes in bead size were observed. This happens because agarose beads lose water in their network when they are exposed to dry air. Losing water in their network brings about size shrinkage that reduces their diameter by about a factor of two. Shrunken beads can then escape through the bottom window of the size selective chip. The agarose beads can repeatedly swell and shrink as their internal water content varies. As dry air flows around the agarose beads, it accelerates dehydration of the inner polymer network. Since the dispensed agarose beads are moved into the size selection unit using air flow, beads suffer from drying and shrinking. A novel idea is suggested to prevent beads from drying by making the environment humid. It is observed that under saturated humid air environment, agarose beads do not change their size more than 5%. It is observed that the saturated humid air preserves wet halos around the agarose beads.

An immunoassay experiment was performed to test the effects of drying and of saturated humid air to verify practical application of the size sorting chip. CRP antibody derrivatized agarose beads were stored under saturated humid air for twenty minutes and observed. The result shows that beads sizes as well as immune reaction strengths are either the same or nearly the same as when the beads are kept under water.

It is concluded that using a saturated humid air environment the size selection method of chemical sensor beads assembly into the micromachined sensor platform is possible.

In the future, the size selection chips need to be produced using stiffer single layer silicon rich nitride film that should lead to an even higher chip yield. Other chemical sensing strategies also need to be evaluated for their sensitivity to wetting and drying to determine if the use of saturated humid air environment is sufficient to prevent damage.

Bibliography

[1] J. J. Lavigne, S. Savoy, M. B. Clevenger, J. E. Richie, B. McDoniel, S. Yoo, E. V. Anslyn, J. T. McDevitt, J. B. Shear, and D. P. Neikirk, "Solution-Based Analysis of Multiple Analytes by a Sensor Array: Toward the Development of an 'Electronic Tongue'," *Journal of the American Chemical Society*, **Vol. 120**, July, 1998, pp. 6429-6430.

[2] G. T.A. Kovacs, Micromachined transducers sourcebook. (2000)

[3] Gelst Inc., Metal-organics for material & polymer technology. (2001)

[4] L. Ristic, Sensor technology and devices, Chapter 3 and 4. (1993)

[5] R.M.Goodman, the introduction of "Artificial Olfaction Systems" at http://www.micro.caltech.edu/micro/people/Grads/dickson/nose/ppframe.htm, (2000)

[6] http://www.microchem.com/products/su_eight.htm

[7] D. J. Campbell, http://mrsec.wisc.edu/edetc/PDMS/

[8] D. J. Campbell, K. J. Beckman, C. E. Calderon, P. W. Doolan, R. H. Moore, A. B. Ellis, G. C. Lisensky, "Replication and Compression of Bulk Surface Structures with Polydimethylsiloxane Elastomer.", *J. Chem. Educ.* **Vol. 76** , 537(1999).

[9] Y. Berdichevsky, J. Khandurina, A. Guttman, and Y.-H. Lo, UV/ozone modification of poly(dimethylsiloxane) microfluidic channels, *Sensors and Actuators B* **Vol. 97**, 402-408 (2004).

[10] http://www.analog.com

[11] http://www.ti.com

[12] Sandia National laboratory, Teaching Material for MEMS course, (1999).

[13] Y.S. Sohn, Dissertation, University of Texas at Austin, (2001).

[14] http://www.genometrix.com, (2000).

[15] A. Goodey, J. J. Lavigne, S. M. Savoy, M. D. Rodriguez, T. Curey, A. Tsao, G. Simmons, J. Wright, S. Yoo, Y. Sohn, E. V. Anslyn, J. B. Shear, D. P. Neikirk, J.

T. McDevitt,“Development of multianalyte sensor arrays composed of chemically derivatized polymeric microspheres localized in micromachined cavities,” *Journal of the American chemical society* 123 (11): pp. 2559-2570 MAR 21 2001.

[16] B. H. Park, Y. S. Sohn, Y. S. Park and D. P. Neikirk, “Fabrication of size sorting chip for chemical array sensor”, *SPIE Smart Sensors, Actuators, and MEMS*, **Vol. 5116**, P303 (2003).

[17] B. H. Park, Y. S. Sohn, D. P. Neikirk, “Development of micro beads size selection chip for chemical array sensor”, *The 7th International Conference on Miniaturized Chemical and BioChemical Analysis Systems, Squaw Valley, California USA* , p631, October 5-9, (2003).

[18] http://galaxy.micro.uiuc.edu/software/index.html, J. Chen, J. Zou and C. Liu , 2001, based upon their paper, Zhenjun Zhu and Chang Liu, “Micromachining process simulation using a continuous cellular automata method”, *Journal of Microelectromechanical systems*, **Vol. 9**, No.2, June (2000).

[19] O.Tabata, K.Kawahata,S.Sugiyama, and I.Igarashi, “Mechanical property measurements of thin films using load-deflection of composite rectangular membranes”, *Sensors and Actuators A*, **Vol. 20**, pp.135-141,(1989).

[20] S.T. Cho et all, “Internal Stress Compensation and Scaling in Ultra sensitive Silicon Pressure Sensors”, *IEEE Trans. Electron Devices*, **Vol. 39**, No. 4, pp 836-842, (1992).

[21] The Britannica encyclopedia, ”Young’s Modulus”, http://www.britannica.com

[22] Agarose Bead Technologies website, www.abtbeads.com

[23] T. Tanaka and D. J. Fillmore, “Kinetics of swelling of gels”, *Journal of Chemical Physics,* **Vol. 70**, no. 3, pp. 1214-1218, (1979).

[24] N. Christodoulides, M. Tran, P. N. Floriano, M. Rodriguez, A. Goodey, M. Ali, D. P. Neikirk, and J. T. Mcdevitt, “A microchip-based multianalyte assay system for the assessment of cardiac risk”, *Analytical Chemistry*, **Vol. 74**, No. 13, 3030-3036, (2002).

[25] http://www.haps.nsw.gov.au/edrsrch/edinfo/crp.html

Vita

Byunghwa Park was born in Busan, South Korea, on March 12, 1972, as the first son of Sangbong Park and Kihyang Chung. After completing his work at Myungji High School, Seoul, South Korea, in 1991, He entered the Department of Electronics Engineering at Korea University in Seoul, South Korea where he received his B.S. in 1996. In August 1998, he entered the Department of Electrical and Computer Engineering at the University of Texas at Austin.

Permanent Address : 501, Sungmo Villa, 350-18 Bookaja Dong,
Sodaemoon koo, Seoul, Korea 120-131.

This dissertation was typed by the author.